# Huygens' measurements of the speed of sound on Titan

## Thesis

# Huygens' Measurements of the Speed of Sound on Titan

Philip David Rosenberg

The Open University
Milton Keynes
UK

Submitted for the degree of Doctor of Philosophy in Planetary and Space Sciences

September 2007

DATE OF SUBMISSION: 28 SEPTEMBER 2007
DATE OF AWARD: 6 MARCH 2008

# Huygens' Measurements of the Speed of Sound on Titan

Philip David Rosenberg

The Open University
Milton Keynes
UK

Submitted for the degree of Doctor of Philosophy in Planetary and Space Sciences

September 2007

# Acknowledgements

As with any PhD thesis written, this one has not been created in isolation and a number of people have made its production possible or at least a little easier. I would firstly like to acknowledge the support of my two supervisors, John Zarnecki and Martin Towner. Without John I would never have been able to work on such a project and he has been able to direct me through the past four years. Martin has been invaluable as a supervisor and in addition to his support overall, his guidance in the lab has been key to me reaching this stage. I would also like to acknowledge Axel Hagermann for the assistance he has provided whilst analysing the Huygens results, Mark Leese for managing the Huygens project at The Open University and being the font of all knowledge with respect to the Surface Science Package, Hakan Svedhem for providing the sound speed instrument and the rest of the Surface Science Package team.

I would like to thank Zöe Flack for not only putting up with me over the past four years but also for insisting on our future marriage. I would also like to thank my parents, Colin and Linda Rosenberg, for all their support over the past four years and for helping Zöe and I set up our first home in the process.

I would also like to say a big cheers to those who have made my time at the Open University such an enjoyable one. Without you I would have gone mad. Notable contributors include Jon Watson, Maria Tynan, Adam Morris, Sarah Web, Tracey Parker, Manish Patel, Tim Ringrose, Vic Pearson, Lee Baker, Cat Maguire, the PSSRI students et al.

Finally, I acknowledge those who have made completing this thesis financially viable; PPARC (now STFC) for funding the PhD for three years and also those people who have employed me during the dark period of my fourth year. Again here, my thanks go out to John Zarnecki. Also, to Jane Fletcher and the rest of the Sky at Night team, who all helped to make my time at the BBC a fantastic experience.

# Foreword

This thesis is essentially based around the results returned from the speed of sound sensor which operated on the Huygens Probe on Saturn's largest moon, Titan. The thesis begins by introducing some of the background knowledge on Titan, including the major results of the Voyager flybys. The latest results from the Cassini-Huygens mission complete chapter 1.

The speed of sound sensor – the Acoustic Properties Instrument-Velocimeter, is introduced in chapter 2. The principles of its function are presented and the process used for the calibration of the sensor is described.

Chapter 3 discusses how the speed of sound in a fluid is related to composition and state (temperature and pressure). This is then placed in the context of Titan's thick atmosphere, consisting of a mixture of nitrogen and methane. A number of predictions from different equations of state are compared to laboratory data so their applicability to Titan can be deduced.

In Chapter 4 the results from the Huygens probe on Titan are presented and the calibration work from chapter 3 is applied to determine the speed of sound in Titan's lower atmosphere. Chapter 5 takes the speed of sound data and uses it to provide estimates of the abundance of methane in Titan's atmosphere at the Huygens landing site. Chapter 6 rounds up the conclusions of the thesis and chapter 7 provides some possible avenues for future research.

Overall this work leads the reader through the process of determining atmospheric composition on Titan from speed of sound measurements. It presents some lessons learnt from the first time such an investigation has been performed in space exploration.

# Contents

Acknowledgements ..... 2

Foreword ..... 3

Contents ..... 4

List of Figures ..... 7

List of Tables ..... 9

Publications ..... 10

Abstract ..... 11

§1 Titan and its Atmosphere ..... 12

§1.1 Voyager ..... 13

§1.2 Earth Based Observations ..... 14

§1.3 Cassini-Huygens ..... 15

§1.4 Cassini Huygens Results ..... 19

§2 Acoustic Properties Instrument - Velocimeter ..... 29

§2.1 Instrument description ..... 33

§2.2 Measurement technique ..... 35

§2.2.1 Instrument Characterisation ..... 38

§2.2.2 Initial characterisation ..... 40

§2.2.3 Temperature measurement ..... 43

§2.2.4 Detailed Characterisation ..... 46

§2.2.5 Top Hat Contraction ..... 55

§2.3 Signal Strength ..... 57

§3 Speed of Sound ..... 60

§3.1 Wave Propagation in a Medium ..... 60

§3.2 Ideal Gas Equations of State ..... 63

§3.3 Non-Ideal Equations of State ..... 64

§3.3.1 Modified Benedict-Webb-Rubin Equation of State ..... 64
§3.3.2 Virial Equation of State ..... 68
§3.3.3 Helmholtz Energy Equation of State ..... 69
§3.4 Comparison of Equations of State ..... 71
§4 Analysis of Huygens Data ..... 77
§4.1 Atmospheric Data ..... 79
§4.1.1 Measurement Scatter ..... 80
§4.1.2 Analysis techniques ..... 84
§4.1.2.1 Upper Limit ..... 84
§4.1.2.2 Numerical Optimisation ..... 86
§4.1.2.3 Bayesian Analysis ..... 89
§4.1.3 Resultant Speed of Sound ..... 94
§4.2 Surface Data ..... 96
§4.2.1 Data Analysis ..... 100
§5 Interpretation of API-V Results ..... 103
§5.1 Atmospheric Methane Concentration ..... 103
§5.1.1 Atmospheric Implications ..... 110
§5.2 Interpretation of Surface Data ..... 113
§6 Conclusions ..... 118
§7 Future Work ..... 122
Appendix ..... 127
A.1 Logging Program ..... 127
A.1.1 Main Program ..... 128
A.1.2 Scope ..... 135
A.1.3 Date ..... 141
A.1.4 Nagspline ..... 143
A.2 Numerical Optimisation Program ..... 148

A.2.1 Main Program ..... 148
A.2.2 Annealing ..... 150
A.3 Bayesian Analysis ..... 158
A.3.1 Main Program ..... 158
A.3.2 Bitmap ..... 167
§8 References ..... 170

# List of Figures

Fig 1.1 Map of Titan created by ISS images up to December 2006.....20

Fig 1.2 The surface of Titan as imaged by DISR.....25

Fig 1.3 Titan's surface as imaged after landing.....25

Fig 1.4 HASI temperature profile measured using the TEM sensor.....26

Fig 2.1 A cutaway of the SSP Top Hat.....30

Fig 2.2 A cutaway through a single API-V sensor.....34

Fig 2.3 Diagram showing how API-V is used to measure the speed of sound.....36

Fig 2.4 The atmospheric chamber used for characterisation of API-V.....40

Fig 2.5 Initial measurement of time of flight with a sensor separation of 55.1 mm.....41

Fig 2.6 Initial measurement of time of flight with a sensor separation of 83.0 mm.....42

Fig 2.7 Speeds of sound calculated from time of flight data at two different separations...42

Fig 2.8 Calibration curve for the rhodium-iron temperature sensor.....45

Fig 2.9 Plot showing a typical received API-V signal.....48

Fig 2.10 Layout of system for calibration of API-V.....50

Fig 2.11 Plot showing pressure in the atmospheric chamber.....52

Fig 2.12 The time of flight offset calculated at temperatures from 82 to 288 K.....54

Fig 2.13 Plot showing the expected peak received signal voltage.....58

Fig 3.1 Plot showing the discontinuity at the pure nitrogen limit for NIST database 14 ....67

Fig 3.2 The variation in predicted sound speeds for the discussed equations of state.....73

Fig 3.3 Comparison between predictions and experimental data for pure $N_2$.....74

Fig 3.4 1st Comparison between predictions and experimental data for $N_2$ and $CH_4$.....74

Fig 3.5 2nd Comparison between predictions and experimental data for N2 and CH4.....75

Fig 3.6 3rd Comparison between predictions and experimental data for N2 and CH4.....75

Fig 4.1 Entire raw, uncalibrated, API-V dataset collected during the Huygens mission ....78

Fig 4.2 Useful, calibrated API-V data collected during the Huygens mission. .....79

Fig 4.3 Histogram of the difference between API-V measured and expected values. .....82

Fig 4.4 Fourier transform of Fig 4.3.. .....82

Fig 4.5 Plot showing the API-V data against height.....85

Fig 4.6 Graphical representation of an optimisation algorithm.....87

Fig 4.7 Probability density function (pdf) used in the Bayesian analysis.....92

Fig 4.8 The result of Bayesian analysis on subsets of 200 data points.....94

Fig 4.9 Speed of sound in Titan's atmosphere as determined by API-V.....95

Fig 4.10 Effect of fluid on API-V sensors if not horizontally aligned .....98

Fig 4.11 Data collected by API-V after impact on Titan's surface. .....100

Fig 4.12 Speed of sound after Huygens' impact on Titan's surface.....101

Fig 5.1 Atmospheric composition based on API-V data .....104

Fig 5.2 plot comparing predicted and measured saturation mole fractions of methane ....105

Fig 5.3 Saturation mole fraction of methane for adiabatically rising air .....112

Fig 5.4 Methane abundance on the surface data assuming no temperature increase. .....114

Fig 5.5 Temperature change on the surface assuming constant methane abundance.....115

Fig 5.6 Cause of total speed of sound increase on the surface.....116

# List of Tables

Table 2.1 Surface Science Package sensors ..... 29

Table 2.2 Calibration points for rhodium-iron RTD ..... 44

Table 2.3 Contraction of Top Hat caused by cooling to liquid nitrogen temperatures ..... 56

# Publications

The following publications have been produced over the course of my PhD studies. Some elements of these publications have contributed to this thesis.

Hagermann, A., Rosenberg, P. D., Towner, M. C., Garry, J. R. C., Svedhem, H., Leese, M. R., Hathi, B., Lorenz, R. D., & Zarnecki, J. C. 2007, Speed of Sound Measurements and the Methane Abundance in Titan's Atmosphere. Icarus, 189, 538.

Hagermann, A., Zarnecki, J. C., Towner, M. C., Rosenberg, P. D., Lorenz, R. D., Leese, M. R., Hathi, B., & Ball, A. J. 2005, Physical Properties as Indicators of Liquid Compositions: Derivation of the Composition for Titan's Surface Liquids from the Huygens SSP Measurements. Monthly Notices of the Royal Astronomical Society, 359, 637.

Zarnecki, J. C., Leese, M. R., Hathi, B., Ball, A. J., Hagermann, A., Towner, M. C., Lorenz, R. D., McDonnell, J. A. M., Green, S. F., Patel, M. R., Ringrose, T. J., Rosenberg, P. D., Atkinson, K. R., Paton, M. D., Banaszkiewicz, M., Clark, B. C., Ferri, F., Fulchignoni, M., Ghafoor, N. A. L., Kargl, G., Svedhem, H., Delderfield, J., Grande, M., Parker, D. J., Challenor, P. G., & Geake, J. E. 2005, A Soft Solid Surface on Titan as Revealed by the Huygens Surface Science Package. Nature, 438, 792.

# Abstract

On 14th January 2005 the Huygens probe descended to Titan's surface, measuring, amongst other properties, the speed of sound in the moon's dense, haze filled atmosphere. These measurements were made by the Acoustic Properties Instrument – Velocimeter (API-V). For a binary mixture of gases, with known components, the sound speed, temperature and pressure can be used to determine the mixing ratio. As the Huygens Gas Chromatograph Mass Spectrometer (GCMS) indicated that the only bulk components of Titan's atmosphere were methane and nitrogen, sound speed has been used as an indicator of methane abundance.

To achieve this, flight spare replicas of API-V have been used for calibration purposes and a non-ideal equation of state supplied by the Groupe Européen de Recherches Gazières (GERG) has been employed to model the sound speed in the cold dense mixtures of nitrogen and methane found on Titan.

The sound speed on Titan was found to decrease from 183.2 m $s^{-1}$ at 11 km altitude to 194.0 m $s^{-1}$ at the surface. Use of the GERG equation of state with Huygens temperature and pressure data indicated that the mole fraction of methane at the surface is 0.026 remaining approximately constant up to 7 km altitude, then decreasing slightly to 0.012 at 11 km altitude. The estimated uncertainty in this value is ±0.018. This is lower than the estimate by GCMS of 0.049±0.0025. There is also a possibility of enhanced methane abundance at the surface and suppressed methane abundance at an altitude of approximately 3 km.

After impact the sound speed was found to increase by ~2 m $s^{-1}$. As API-V was in a separate thermal environment to the temperature sensor, this could be due to an increase in temperature of ~2 K or due to methane evaporating from the potentially wet ground increasing the methane mole fraction by 0.08.

# Chapter 1
# Titan and its Atmosphere

Titan is Saturn's largest moon, with a diameter of 5150±1 km (Lindal, et al. 1983). This is larger than the planet Mercury and places Titan behind only Ganymede in the list of largest moons of our Solar System. The moon itself was discovered by Christiaan Huygens in 1655 (Huygens 1655), and detection of its atmosphere was reported nearly 300 years later when absorption bands of gaseous methane were discovered (Kuiper 1944). In his paper Kuiper acknowledged earlier observations of Titan, generally attributed to the Spanish astronomer Jose Comas Sola, reporting the atmospheric phenomena of limb darkening. However, he also claimed that making such observations should not be possible.

It was quickly realised that the conditions on Titan were potentially cold enough to cause methane in the atmosphere to condense or freeze. This led to the possibility of a hydrological cycle on Titan based around methane, making Titan a unique and incredibly interesting body.

The following section provides a short overview of the state of knowledge of Titan at the time of writing. With the Huygens mission complete and Cassini in its $4^{th}$ year in orbit around Saturn, there is clearly a vast quantity of material, and the first of the books discussing recent findings about Titan have recently been published (Harland 2007). Hence, this introduction cannot hope to explain everything that is currently known about Titan. It will instead introduce some of the Voyager findings that, despite being superseded, represented the best information available when Huygens was being designed. The focus will then move on to Titan's lower atmosphere and surface as these are the important factors in the investigation of sound speed presented in this work.

## §1.1 Voyager

A large leap in the understanding of Titan's atmosphere occurred when the Voyager spacecraft performed flybys in 1980 and 1981. Both Voyager spacecraft found Titan's atmosphere to be opaque to their cameras. The opacity was caused by a haze in the atmosphere produced by photo-dissociation of methane and subsequent reactions of the created methyl free radicals. Voyager 1 performed a radio occultation experiment and observed Titan in the infrared and ultraviolet. The ultraviolet experiment allowed detection of nitrogen (Broadfoot, et al. 1981) as the major constituent in Titan's atmosphere. The radio occultation and infrared data allowed reconstruction of the temperature profile below 200 km (Lindal, et al. 1983) and determination of the mean molecular mass, which was found to be in the range 28.3-29.2 g $mol^{-1}$ (Samuelson, et al. 1981). As this mass is higher than is possible for a mixture of methane and nitrogen only, a third heavier component was inferred with argon being the most likely candidate. Further reanalyses of the available data over the following decades allowed refinements to be made to the model of Titan's atmosphere (Lellouch, et al. 1989; Courtin, et al. 1995; Samuelson, et al. 1997) and the possibility that Titan's atmosphere may be supersaturated with methane emerged. This could only occur if Titan's atmosphere was depleted in condensation nuclei, stopping the condensation of methane despite the concentration being above the saturation point.

The same photolytic processes that have been creating smog on Titan have also been destroying methane, hence some source for replenishment of the gas is required otherwise the methane in Titan's atmosphere would have been entirely removed in a time period of the order $10^7$-$10^8$ years (Yung, et al. 1984; Toublanc, et al. 1995). After the Voyager mission the prime candidate for such a reservoir was surface liquid in the form of oceans (Tyler, et al. 1981; Flasar 1983).

## §1.2 Earth Based Observations

Clearly, at close range, the Voyager spacecraft were able to provide some of the best data available in the early 80s. However, as technology improved, Earth-based observations began to add to our knowledge of Titan. After the Hubble Space Telescope was launched, the first surface images of Titan became available using wavelengths that could penetrate the smog (Smith, et al. 1996). The Hubble images revealed light and dark areas on the surface of Titan which were interpreted as water ice and organic material respectively. The bright material was interpreted as either fresh ice excavated by impact or as cleaned ice, washed by methane rain at high altitudes. Despite further reviews of the available data (Lorenz & Lunine 1997; Lunine, et al. 1998; Ori, et al. 1998; Taylor & Coustenis 1998) no consensus was reached about the nature of the surface, with organics, liquids, silicates, ices, frosts and altitude variations all being potentially responsible for differences in surface brightness. Further atmospheric modelling continued, although the sparse data meant that much of the work relied on inference (Flasar 1998).

As ground-based adaptive optics improved, observations of details on Titan's disc became possible from the surface of the Earth. The Keck telescope's adaptive optics were responsible for the discovery of the first tropospheric clouds on Titan in December 2001 and February 2002 (Brown, et al. 2002). These clouds were found at the south pole of Titan, just after Titan's southern hemisphere summer solstice, despite models at the time predicting clouds in the equatorial region. Comparison of methane absorption in spectra from cloudy and non cloudy parts of Titan's disk revealed the altitude of the cloud tops at approximately 16±5 km. In November 2002 the Very Large Telescope also found a bright feature in the atmosphere, circling Titan's South Pole and possibly associated with a south polar vortex (Gendron, et al. 2004).

In 2001 and 2002 a rare opportunity also occurred to use the extremely large, but restricted field of view, Arecibo radar dish to investigate the radar reflectivity of Titan's surface

(Campbell, et al. 2003). In this investigation, some points on Titan's surface were found to reflect specularly a radio signal in a manner consistent with a smooth liquid surface supporting the suggestion of liquid oceans on the satellite.

Hence, before the arrival of the Cassini-Huygens spacecraft in Saturn orbit, Titan was already being revealed as a wonderfully rich and varied world worthy of significant further study.

## §1.3 Cassini-Huygens

In June 2004, Cassini-Huygens arrived at the Saturnian system, entering Saturn orbit on 1st July. The spacecraft itself was composed of two parts. Cassini would remain in orbit around Saturn taking remote measurements of the planet and its moons, magnetosphere and rings, whereas Huygens would detach from Cassini on the 3rd orbit to descend through Titan's atmosphere on 14th January 2005.

Cassini was armed with a suite of 12 instruments and Huygens 6. The Cassini instruments most relevant to the investigations of Titan's surface and lower atmosphere follow, along with a brief description of their relevant capabilities.

- **Composite Infrared Spectrometer (CIRS)** CIRS uses two spectrometers, one for the far and one for the near infrared regions, coupled with a 50 cm telescope. It achieves spectral resolution of 0.5 to 15.5 $cm^{-1}$. It was designed to search for carbon, oxygen and nitrogen bearing molecules and aerosols in Titan's atmosphere. In combination with radio occultation data CIRS allows probing of temperatures in Titan's atmosphere in a similar manner to the Voyager 1 investigation (Flasar, et al. 2004).
- **Imaging Science Subsystem (ISS)** The ISS consists of a narrow angle and wide angle telescope with fields of view of 0.35° and 35° respectively. It is the highest spatial resolution imaging system on Cassini and each telescope uses a 1024×1024 pixel CCD. The telescopes are equipped with filters spanning the range 200 to

1100 nm, allowing penetration of the Titan haze in specific spectral windows (Porco, et al. 2004).

- **Ultraviolet Imaging Spectrograph (UVIS)** UVIS was designed to investigate the abundance of molecular species and aerosols in Titan's atmosphere and investigate global circulation of the atmosphere by tracking such compounds. The instrument would also investigate upper atmospheric processes relating to interactions with Saturn's magnetosphere. UVIS has two spectral channels with ranges of 56-118 and110-190 nm (Esposito, et al. 2004).
- **Visible and Infrared Mapping Spectrometer (VIMS)** VIMS is an imaging spectrograph, with moderate spectral and high spatial resolution; it therefore provides an intermediate instrument between the ISS and CIRS instruments providing synergies between the three datasets. The VIMS instrument can build up an image cube of the target having 2 spatial dimensions and a spectral dimension. This allows correlation between imaged features of Titan and their spectra. The spectral range, from 0.3 to 5.1 μm, allows VIMS to use the variation of methane absorption with wavelength to probe different levels in the atmosphere or the surface of Titan (Brown, et al. 2004).
- **Radar** The Radar is able to operate in synthetic aperture imaging, altimetry, scatterometry and radiometry modes and, due to the transparency of Titan's atmosphere to radar, allows investigation of Titan's surface (Elachi, et al. 2004).
- **Radio Science (RSS)** The Radio Science subsystem can investigate Titan's atmosphere using radio occultations in a similar manner to the Voyager radio occultation experiment and also provide detailed mapping of Titan's gravitational field (Kliore, et al. 2004).

Cassini also included the following instruments, although their relevance to Titan's lower atmosphere and surface is not as significant as those above.

- Cassini Plasma Spectrometer (CAPS)

- Cosmic Dust Analyzer (CDA)
- Ion and Neutral Mass Spectrometer (INMS)
- Magnetometer (MAG)
- Magnetospheric Imaging Instrument (MIMI)
- Radio and Plasma Wave Science (RPWS)

Huygens was specifically designed to perform an in-situ investigation of Titan's atmosphere. The probe itself was not provided with a soft (i.e. airbag or rocket assisted) landing mechanism and post-landing science could not be guaranteed. Despite this, the probe was expected to float for a short period of time should it land on a liquid surface and it was also expected to survive landing if the substrate was not too hard. Bearing this in mind, of the six instrument packages on Huygens, only one was designed to study primarily at the surface of Titan, with the rest being atmospheric instruments. A brief description of each instrument follows.

- **Huygens Atmospheric Structure Instrument (HASI)** HASI included accelerometers, electrical conductivity sensors and temperature and pressure sensors for measuring physical properties of the atmosphere during descent (Fulchignoni, et al. 2002).
- **Gas Chromatograph Mass Spectrometer (GCMS)** The GCMS was a gas chromatograph connected to a mass spectrometer that allows individual species to be separated by both volatility and mass number. The system takes direct atmospheric samples from an altitude of approximately 176 km to the surface as well as accepting samples from the ACP (see below) (Niemann, et al. 2002).
- **Aerosol Collector Pyrolyser (ACP)** The ACP sampled atmospheric gases, pumping them through a filter to extract any solid particles or aerosols. The collected aerosols were then baked at up to 600° C and any gases evolved from this pyrolysis were passed to the GCMS for analysis (Israel, et al. 2002).

- **Descent Imager/Spectral Radiometer (DISR)** DISR performed all the imaging and spectral functions of Huygens. It included three cameras, all on fixed mountings on the probe. Each camera was centred on the same azimuthal point with different angles of nadir, allowing a field of view covering the range from 6.5° (almost straight down) to 96° (slightly above horizontal). The cameras relied on the spin of the probe during descent to produce images at different angles of azimuth. DISR was also armed with a solar sensor, spectrometers, and photometers (Tomasko, et al. 2002).
- **Doppler Wind Experiment (DWE)** The DWE consisted of an ultra-stable oscillator on the Huygens probe as part of the radio link and a similar ultra-stable oscillator on Cassini. This would allow the Doppler shift in the signal to be determined and hence the line of sight velocity to be calculated. This would allow determination of the effect of Titan's winds on Huygens (Bird, et al. 2002).
- **Surface Science Package (SSP)** SSP was the only instrument on Huygens with the primary aim of measuring properties of Titan's surface (Zarnecki, et al. 2002). However, some sensors within the package also had the potential to work during descent. As there was a strong possibility of a liquid landing, many of the sensors were developed to measure properties of liquids such as refractive index, speed of sound, depth, thermal conductivity, density, permittivity and tilt caused by waves. In the case of a solid landing, SSP included a penetrometer that would measure the mechanical strength of the ground to a depth of 55 mm, and a sonar that had the potential to infer details of topography. SSP also included a high sensitivity accelerometer. The sound speed sensor and thermal conductivity sensor could also take atmospheric measurements during descent in addition to liquid measurements post landing. Analysis of these atmospheric sound speed measurements form the basis of this work.

## §1.4 Cassini Huygens Results

Even before Huygens made its descent onto Titan, Cassini was able to pierce the smog to view the moon's surface. When Cassini made its first flyby of Titan, ISS was able to provide the first high resolution images of Titan's surface showing a non-homogeneous surface with dark and bright regions that correlated well with the Hubble and other Earth-based observations. The latest albedo map at the time of writing, created using ISS results, is shown in Fig 1.1. Even with the increased resolution, no evidence was found to identify unambiguously the dark areas as liquids. In fact, the low contrast at the boundaries was more consistent with the dark regions being solid (Porco, et al. 2005).

Despite the still ambiguous status of liquids on Titan, within the first few flybys ISS was able to show that the moon's surface has preserved relatively few impact craters and has an age of only 130 – 300 Myr (Porco, et al. 2005). Other features identified on the surface include diffuse bright streaks, narrow dark lineaments and bright and dark patches and spots. Some possible explanations for these features include aeolian or fluvial activity, icy volcanism and tectonic activity, although no firm conclusions have been made (Porco, et al. 2005). One particularly likely candidate for a cryovolcanic feature on Titan has been observed by the VIMS instrument (Sotin, et al. 2005). The feature in question is bright and roughly circular with a dark spot in the centre. It also includes two large lobate extensions, which have been interpreted as possible cryolava flows.

ISS was also able to see a large methane cloud structure circling Titan's south pole similar to those seen from Earth. Based on their morphology they have been interpreted as convective tropospheric clouds (Porco, et al. 2005). Models of convective motion on Titan have predicted similar cloud clusters (Hueso & Sanchez-Lavega 2006), and the modelling indicates that the south polar formation is made up of approximately 100 convective cells capable of raining heavily for at least around 2 hours, dropping around 100 kg $m^{-2}$ (approximately 20 cm) of methane rain onto Titan's surface.

**Fig 1.1 Map of Titan created by ISS images up to December 2006. The map is a full globe cylindrical projection extending from pole to pole and from 360° longitude at the left hand edge to 0° longitude at the right hand edge. The Huygens Landing site is represented with a white dot. Image courtesy of NASA/JPL/Space Science Institute**

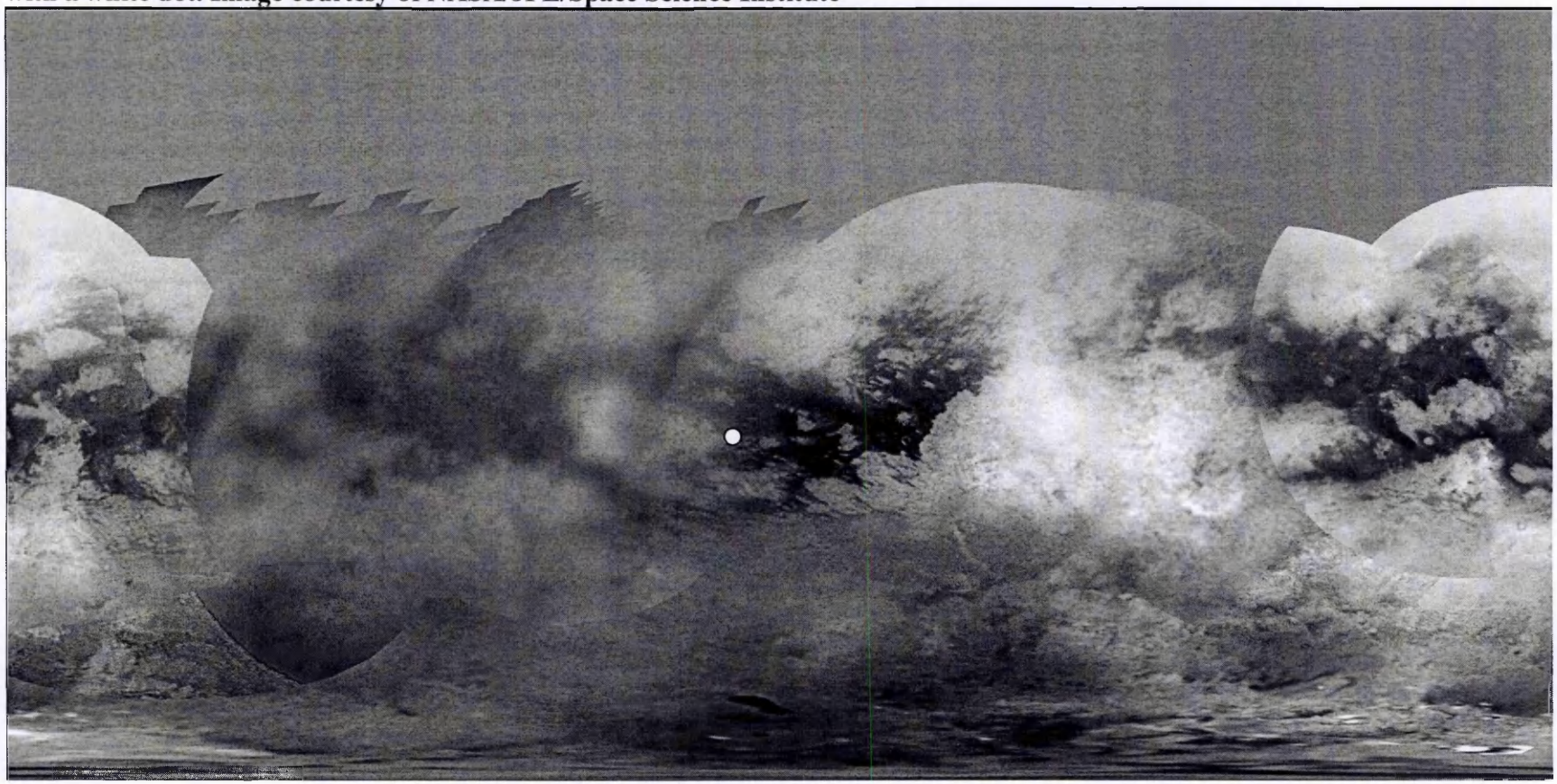

In addition to the polar cloud formation, long thin clouds, aligned almost along lines of constant latitude, and small mid-latitude tropospheric clouds have been seen (Porco, et al. 2005). The smaller clouds are found to have similar cloud top altitudes as the polar clouds of around 25 km; however, the long thin clouds are much lower. The preferred explanation for formation of clouds at such a low altitude is emission of methane from surface sources such as cryovolcanoes. However, so far, no surface features have been found to be associated with the clouds in the ~1 km resolution images available.

The Cassini Radar was also able to use its synthetic aperture radar (SAR) functionality to observe Titan's surface during the early part of the mission. At each flyby where the SAR is used, a long thin strip of Titan is imaged. The resulting strips are monochrome, with bright regions corresponding to areas either with a high radar reflectivity, a tilt angle towards the probe or a rough surface on scales similar to the wavelength used. Although there is not a 1:1 correlation between features seen in SAR and by the ISS or VIMS, many features seen by ISS are seen by SAR. The SAR images show channels, impact craters and possible volcanic flows (Elachi, et al. 2005; Elachi, et al. 2006; Stofan, et al. 2006).

One discovery made by the radar relates to the dark areas of Titan's surface. The dark equatorial regions (latitudes less than ~45°) have been shown to be covered by dune formations (Lorenz, et al. 2006b). These are visible using SAR because they are aligned in an approximately east-west direction and have been viewed by Cassini from the north and south. The change in tilt across the dunes is hence highlighted in the SAR images. The dunes do not show up, however, in other wavelengths because scattering of sunlight by Titan's atmospheric haze creates diffuse lighting conditions at the surface with little or no shadowing (Porco, et al. 2005). The observations of dune features indicate conclusively that the equatorial dark regions cannot be seas of liquid hydrocarbons. The dunes are longitudinal (i.e. parallel to the prevailing wind direction) and could be composed of sand sized grains of organic molecules formed in the atmosphere or of ice particles (possibly

incorporating impurities), although the dark colour when viewed with ISS suggests that solid organics are the preferred explanation.

Although higher latitude regions do not show dune features, it is likely that these areas are composed of similar granular, solid material to the equatorial regions. The lack of visible dunes could be caused by increased wetting or lower wind-speeds closer to the poles which would in turn lead to a reduction of the saltation processes required in dune formation (Lorenz, et al. 2006b).

Although the dark colour of the dunes may indicate a composition of organics, the VIMS instrument has found that the spectra of these regions is best approximated by pure water ice (McCord, et al. 2006). As methane clathrate hydrate has an almost identical infrared spectrum to water ice (Smythe 1975) this could also be a potential component. Surprisingly, the bright areas were found to be a poor match to water ice and no good matches for the spectra of bright regions have been determined (McCord, et al. 2006).

The lack of a global covering of open liquids raises two particularly pertinent questions. What is the source of replenishment for atmospheric methane destroyed by photolysis? Where is the large volume of ethane produced by the same photolysis process over Titan's lifetime (Lunine, et al. 1983)? Earlier in this section, reference has been made to potential cryovolcanic activity on Titan, and a cryovolcanic origin for Titan's methane is very plausible. One model (Tobie, et al. 2006) predicts that Titan consists of a solid methane clathrate hydrate shell above an ice layer which floats upon a subterranean ocean of water and ammonia. At Titan's centre lies a silicate core. Methane clathrate hydrate is a solid consisting of methane and water molecules which may form on Titan (Lunine & Stevenson 1987). Tobie et al. (2006) predicted that over the past ~1 billion years the ice layer should have become unstable to convection, leading to the onset of hot plumes which can cause dissociation of the clathrate and release of methane gas in cryovolcanic outbursts. The expected methane production rate is 1-3 times the current destruction rate which may explain the survival of methane on Titan without large surface reservoirs.

If methane has existed upon Titan for long periods of time, as expected in the model by Tobie et al. (2006), then large quantities of ethane should have been produced. At Titan's surface temperatures and pressures, ethane should condense into a liquid. However, instead of a global covering of liquid ethane being discovered, Cassini has found large expanses of dark dunes. If the dunes are composed of hydrocarbon material then the dunes themselves may have locked away the expected liquid ethane. The ethane atmospheric depth profile on the gas giant planet Jupiter requires that ethane is adsorbed/absorbed on/in organic dust particles. The ethane cannot be released again at temperatures below ~300 K except by photon-stimulated desorption. The same process may occur on Titan, hence the grains that make up Titan's dunes may have locked away the expected ethane oceans (Hunten 2006).

On 14$^{th}$ January 2005, Huygens entered Titan's atmosphere and impacted the surface, giving an incredibly high resolution snapshot of a small area of Titan. Generally, all instruments worked well onboard Huygens; however, an unfortunate problem on Cassini caused one of the two radio channel links to be lost with the result that many experiments lost some data. Despite this, a vast amount of information was able to be collected (Lebreton, et al. 2005).

The probe itself drifted eastwards during its descent through Titan's superrotating atmosphere (Bird, et al. 2005) before reversing direction at approximately 7 km altitude (Tomasko, et al. 2005) and eventually landing on an area of dark terrain just a few km from a boundary with bright terrain. During descent DISR found that haze in Titan's atmosphere extended all the way to the surface and the cameras were only able to resolve surface features once they descended to below ~50 km altitude. Despite this, DISR was able to image both the landing site in the dark terrain and the nearby bright terrain. The images show what appear to be dark drainage channels cut into the bright terrain, ending in what appears to be a coastline which defines the boundary with the dark terrain. Some of the channels appear to be dendritic, with many branches similar to terrestrial channels formed by precipitation, while others show less branching and are more similar to

terrestrial sapping channels (Tomasko, et al. 2005). Some images are shown in Fig 1.2 and Fig 1.3. Huygens landed in the dark terrain, finding it to be solid but relatively soft and similar in texture to uncompacted sand or gravel (Zarnecki, et al. 2005). The surface near Huygens is strewn with cobbles each with a diameter of around 10-15 cm sat upon a bed of finer granular material. On top of this relatively soft material, the SSP penetrometer measured a much softer layer with a depth of approximately 5 mm and then experienced large instantaneous force before penetrating into the granular material below. One possible explanation is that the penetrometer impacted with one of the cobbles before pushing it aside; the initial soft layer could be organic deposits atop the cobble (Zarnecki, et al. 2005). The physical nature of Titan's atmosphere was measured during the descent by HASI. The minimum temperature of 70.43±0.25 K was measured at an altitude of approximately 44 km and pressure of 0.115±0.001 MPa. The temperature and pressure at the surface were found to be 93.65±0.25 K and 0.1467±0.0001 MPa (Fulchignoni, et al. 2005; Harri, et al. 2006) The temperature profile is shown in Fig 1.4. The agreement with the Voyager temperature profiles (Lellouch, et al. 1989) is excellent. The lapse rate at the surface is close to the adiabatic lapse rate[1] of around -1.1 K $km^{-1}$ and generally increases with altitude within the troposphere (Fulchignoni, et al. 2005). This would indicate that in general, the troposphere is stable to convection; however, no direct measurement was taken of the ground surface temperature. Where sunlight falls upon a planetary surface beneath an atmosphere, a temperature discontinuity can be expected to occur, which, if large enough, may provide a heat source for the onset of convection. The accelerometry results from HASI do indicate a slight upward motion of air in the troposphere with a speed varying with altitude from 0 to 0.1 m $s^{-1}$ (Teemu, et al. 2006).

[1] The lapse rate is the rate of change of temperature with altitude. The adiabatic lapse rate is the expected lapse rate for a pocket of gas rising and expanding adiabatically.

**Fig 1.2 The surface of Titan as imaged by DISR showing dendritic river channels which appear to drain from light terrain onto dark terrain. This image is ~11 km across and Huygens landed below the lower edge. Image courtesy of ESA/NASA/JPL/University of Arizona.**

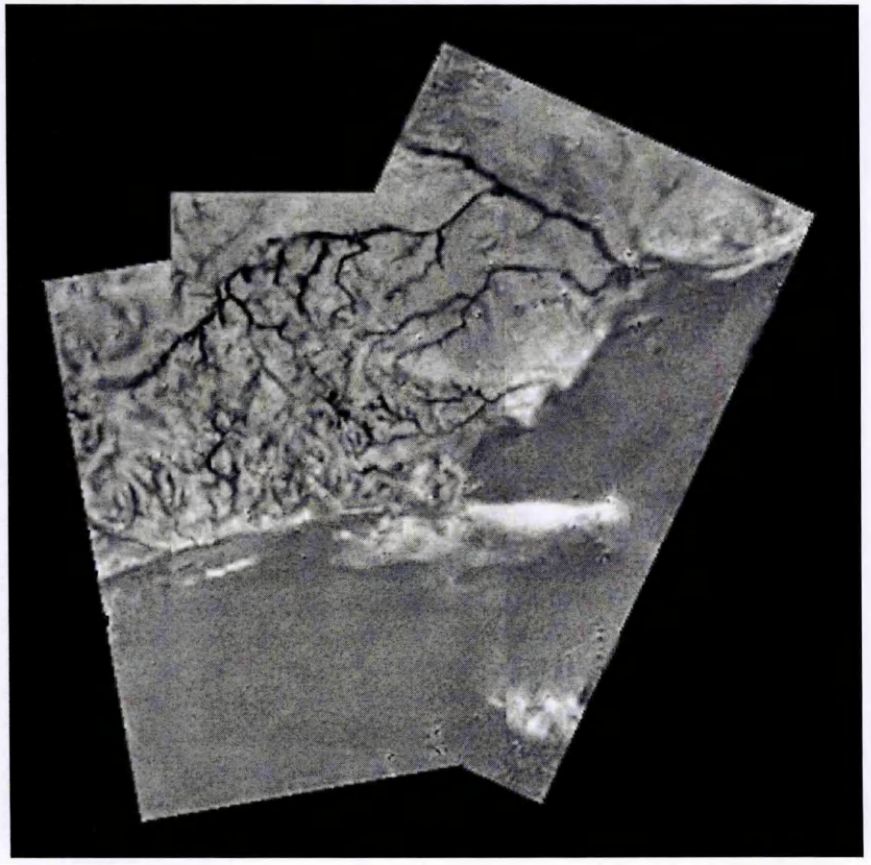

**Fig 1.3 Titan's surface as imaged after landing. The cobbles seen on the surface are ~10 cm diameter. Image courtesy of ESA/NASA/JPL/University of Arizona.**

**Fig 1.4 HASI temperature profile measured using the TEM sensor (Fulchignoni, et al. 2005)**

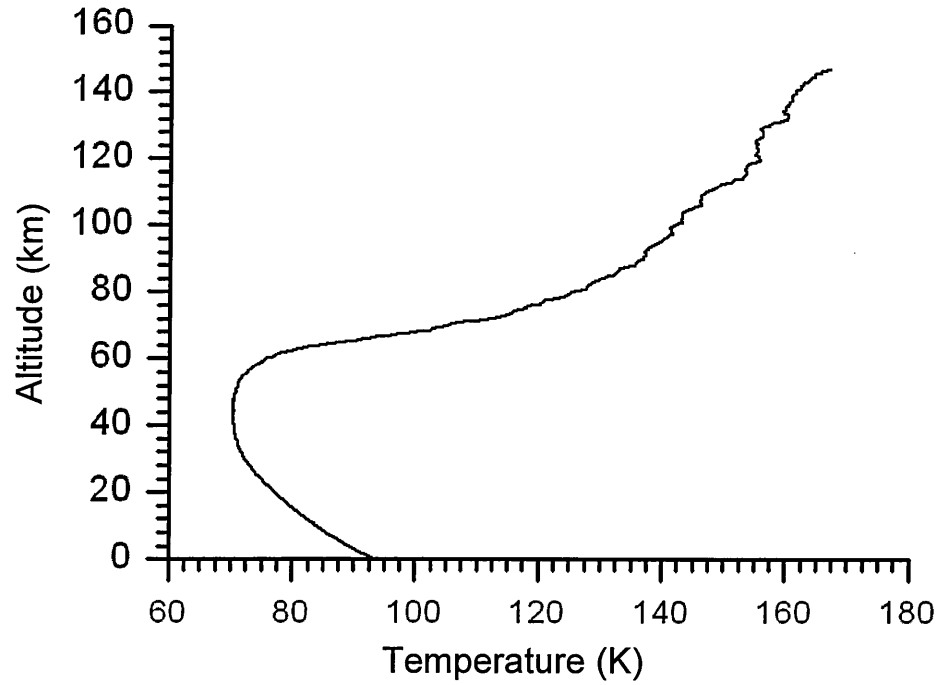


During descent the composition of the gas component of the atmosphere was measured by the GCMS. Noble gases were found only in trace amounts, with radiogenic argon-40 and primordial argon-36 existing with mole fractions of $(4.3\pm0.1)\times10^{-5}$ and $(2.8\pm0.3)\times10^{-7}$ respectively. These were the only heavy noble gases found with abundances above the detection limit of $10^{-8}$. With the fraction of argon measured at only trace levels the only two bulk components of the atmosphere were nitrogen and methane. The methane mole fraction was measured at a number of points during the descent and was found to be $(1.41\pm0.07)\times10^{-2}$ in the stratosphere increasing to $(4.9\pm0.25)\times10^{-2}$ below 8 km in the troposphere (Niemann, et al. 2005). The low abundance of primordial argon has implications for the formation of Titan's atmosphere. Two competing theories for the formation of the atmosphere exist. The first is that the nitrogen atmosphere evolved from ammonia that was incorporated into Titan as an ice during its accretion (Atreya, et al. 1978). The second is that molecular nitrogen was delivered to Titan in the form of a clathrate hydrate. In the second scenario argon should also have been bound in the

clathrate and should exist on Titan in significant quantities (Owen 1982). As this is not the case the ammonia scenario is favoured.

Immediately after landing, GCMS measured an increase in its methane signal indicating that methane may have been evaporated from the surface by the heat of the probe. Other larger molecules, such as ethane and possibly cyanogen, benzene and carbon dioxide, were also detected after impact (Niemann, et al. 2005).

The GCMS was also used to analyse the pyrolysis products of the aerosols collected by ACP. The pyrolysis fragments detected by the mass spectrometer of GCMS indicate that the aerosols collected consisted of large molecules of carbon and nitrogen which, upon heating, evolved into $NH_3$ and HCN. No difference was observed between aerosols collected in the stratosphere compared with those collected in the troposphere (Israel, et al. 2005).

During the final part of the descent, the SSP sonar instrument measured the distance to the surface and the acoustic reflectivity of the area around the landing site (Zarnecki, et al. 2005). The reflected signal was found to be specular and showed that variations in topography had amplitudes <1 m. The specular reflection indicates a smooth surface on scales similar to the sonar wavelength (of the order centimetres) (Towner, et al. 2006).

The SSP speed of sound sensor was also active during the descent of Huygens and the results will be presented in detail in this work; in particular the speed of sound has been used as an indicator of the bulk composition (i.e. methane mole fraction) of the atmosphere.

Since the Huygens landing, significant further development has been made by Cassini. Imaging of the north polar region of Titan, in particular using SAR, has identified a large number of dark features interpreted as lakes and seas (Stofan, et al. 2007). This is the first discovery of large expanses of liquid exposed on the surface of Titan. Full maps of the regions in question await publication although the dark features fall into two broad categories. Some tend to have irregular coastlines, resembling flooded river basins,

whereas others tend to be more rounded in shape. Clearly such expanses of liquid will have an effect on the methane cycle on Titan and it remains to be seen how extensive liquid features are on Titan's surface.

# Chapter 2
# Acoustic Properties Instrument - Velocimeter

The Acoustic Properties Instrument – Velocimeter (API-V) was installed on Huygens as part of the Surface Science Package (SSP). Its primary purpose was to measure the speed of sound in any surface liquid should Huygens make a splashdown on Titan. Information from API-V, combined with measurements of other liquid properties by other SSP sensors (Table 2.1), would have allowed limits to be placed on the bulk composition of the liquid depending upon the number of components in the liquid mixture (Hagermann, et al. 2005). Each of these instruments was mounted around or inside a cavity that became affectionately known as the Top Hat, due to the shape of its polymer structure. The sensors and the Top hat can be seen in Fig 2.1

**Table 2.1**
**Surface Science Package sensors (Zarnecki, et al. 2002)**

| Sensor | Properties measured |
|---|---|
| Accelerometer Internal (ACC-I) | Probe acceleration during descent and after landing |
| Accelerometer External (ACC-E) | High time resolution force as penetrator is pushed into surface |
| Acoustic Properties Instrument – Sonar (API-S) | Altitude and surface topography during descent and depth of liquid after landing |
| Acoustic Properties Instrument – Velocimeter (API-V) | Speed of sound in atmosphere and liquid |
| Density Sensor (DEN) | Density of liquid |
| Permittivity Sensor (PER) | Permittivity of liquid |
| Refractive Index Sensor (REF) | Refractive index of liquid |
| Thermal Properties Sensor (THP) | Thermal conductivity of atmosphere and liquid |
| Tiltmeter (TIL) | Spacecraft tilt and wave motion |

Before launch in 1997, there was an expectation that significant parts, if not all, of Titan's globe would be covered in oceans or lakes (Sagan & Dermott 1982; Lunine, et al. 1983; Lellouch, et al. 1989; Sohl, et al. 1995; Smith, et al. 1996; Lorenz & Lunine 1997). Just

prior to the Huygens landing, specular radar reflections were discovered in 12 out of 16 measurements made using the Arecibo and Green Bank radio telescopes (Campbell, et al. 2003). These specular reflections were consistent with the existence of hydrocarbon lakes although this was not the only possible explanation. It was therefore perfectly sensible that a large proportion of the SSP instruments were optimised for a possible liquid landing. However, upon landing, Titan's surface at the impact site was found to be essentially dry.

**Fig 2.1 A cutaway of the SSP Top Hat showing the instruments mounted inside the cavity(Zarnecki, et al. 2005). Instrument details can be found in Table 2.1**

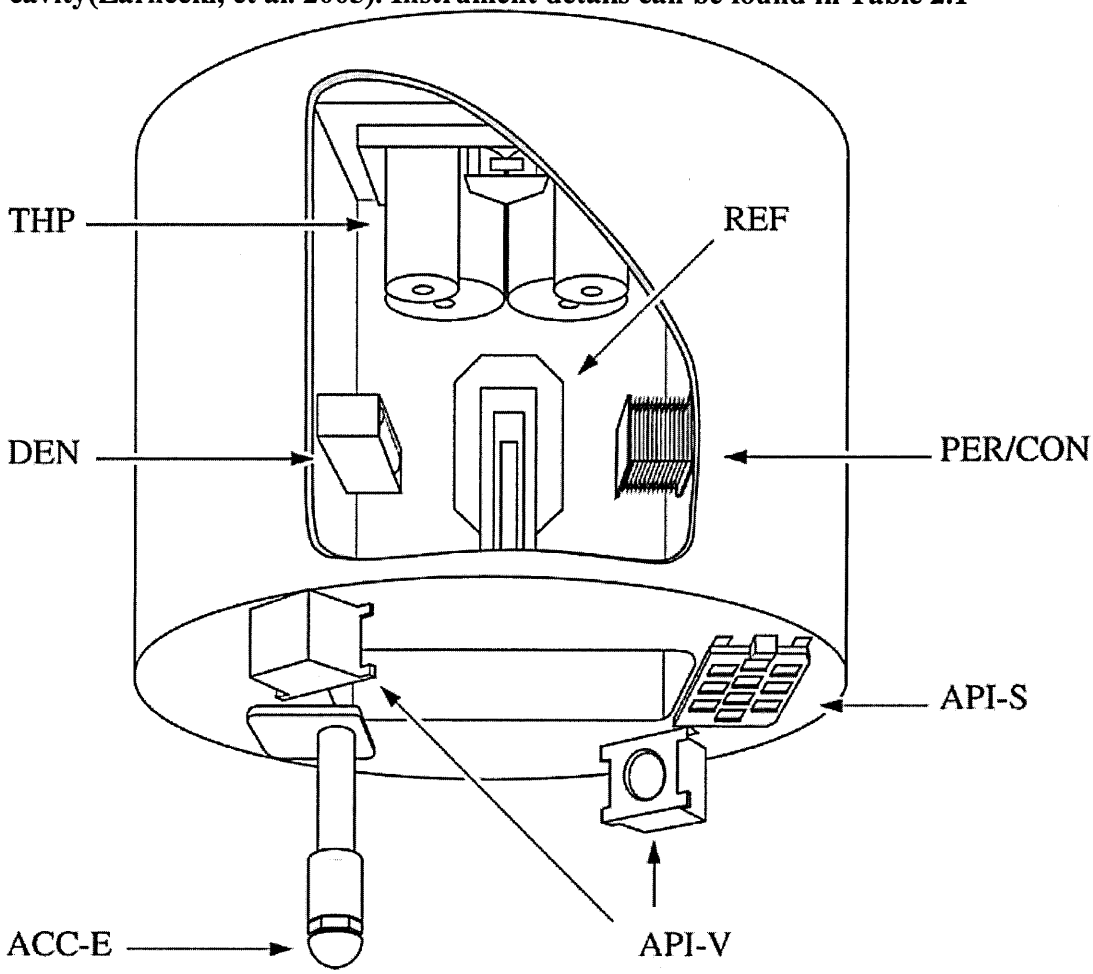


API-V's secondary objective was to measure the speed of sound in Titan's atmosphere and, as Huygens did not land in a liquid, this was the only objective performed. Despite the solid surface, API-V continued to function after landing and, had Huygens made a liquid landing, the primary objective would also have been successfully completed.

The purpose of measuring the speed of sound in Titan's atmosphere was to relate this property to composition. In an ideal gas, the speed of sound, c, is related to composition by

$$c = \sqrt{\frac{\gamma RT}{m}}, \qquad \textbf{Eq 2.1}$$

with $\gamma$ equal to the ratio of specific heats, R the ideal gas constant, T the absolute temperature and m the mean mass per mole of the gas mixture. Hence, measuring sound speed and temperature of an ideal gas reveals the ratio $\gamma/m$. The situation on Titan is, however, more complex as the atmosphere is too cold and dense for the ideal gas approximation to be used. Instead, a non ideal equation of state must be used to describe the effect of composition and state on the speed of sound. This will be discussed in detail in Chapter 3.

Both temperature and pressure measurements for Titan's atmosphere are also required and these properties were measured by the Huygens Atmospheric Structure Instrument (HASI) (Fulchignoni, et al. 2002; Harri, et al. 2006). As ambient conditions were reported from HASI, if Huygens affected the temperature or pressure around it then the conditions reported may not correspond to those experienced by API-V. Clearly, the air ahead of the probe was compressed as Huygens descended with this adiabatic compression causing some degree of heating. Solving the Bernoulli equation for inviscid flow around a blunt object gives an increase in pressure at the head of the object of

$$\Delta P = \tfrac{1}{2} v^2 \rho, \qquad \textbf{Eq 2.2}$$

where v is the flow speed and $\rho$ is the density of the fluid. For Huygens during descent at the altitudes where API-V was making measurements, this equates to around 50-100 Pa. The magnitude of the heating caused by this adiabatic compression has been calculated to be approximately 0.01 K. The pressure change is non-negligible, though the dependence of the speed of sound on pressure is small. This increase in pressure would increase the sound speed by only a few mm $s^{-1}$, which is orders of magnitude lower than other uncertainties. The temperature change is much smaller than the 0.25 K accuracy of the temperature sensor and can be regarded as negligible.

Although there is likely to be heat loss from the Top Hat, estimated to be around 13 W (Merryweather-Clarke 1995), the API-V sensors are mounted at the opening of the structure and hence should be sampling fluid unaffected by heat conducted from this leak. In order to determine the affect of heat radiated out of the Top Hat entrance a basic model has been set up. For an element of atmosphere a distance, s, ahead of the probe presenting an area, dA and a thickness, dz, the energy absorbed in time dt is

$$dE = \frac{PdA}{2\pi s^2} e^{-\alpha s} \alpha dz dt, \qquad \textbf{Eq 2.3}$$

where P is the power being emitted and $\alpha$ is the absorption coefficient of the atmosphere. Eq 2.3 assumes energy is radiated out of the Top Hat in a hemisphere. The increase in temperature caused by this absorption of energy is

$$dT = \frac{dE}{dAdz\rho c_p}, \qquad \textbf{Eq 2.4}$$

where $\rho$ is the density and $c_p$ is the heat capacity at constant pressure. If gas is flowing towards the Top Hat with velocity v=-s/t then dt=-ds/v, allowing Eq 2.3 and Eq 2.4 to be combined and integrated to give the change in temperature

$$\Delta T = \frac{P}{2\pi} \frac{\alpha}{v\rho c_p} \int_{\infty}^{0} \frac{e^{-\alpha s}}{s^2} ds. \qquad \textbf{Eq 2.5}$$

The integration from 0 introduces a factor of 1/0. This is because the emission has been assumed to come from a point source, so at zero distance the flux is infinite. To avoid this, the integration is instead taken to a distance of 0.06 m. This gives a diameter of the hemisphere approximately equal to the separation of the sensors.

Wien's Law indicates that the emission from the Top Hat will be in the far infrared with a wavelength of approximately 30 μm. Laboratory data for the absorption coefficient of methane and nitrogen mixtures at these wavelengths exist down to temperatures of 126 K (Buser, et al. 2004). At these temperatures we can expect a gas mixture representative of Titan's atmosphere to have an absorption coefficient of $\sim 1 \times 10^{-3}$ $m^{-1}$. Inserting this value

into Eq 2.5 and performing the integration, assuming all heat escaping the Top Hat is radiated through the opening, gives a temperature increase of only $1\times10^{-6}$ K. This is entirely negligible. The data of Busler (2004) indicates that the absorption coefficient increases with decreasing temperature, however, to cause an increase in temperature of the order 1 mK would require an absorption coefficient ~10 $m^{-1}$. For an absorption coefficient larger than this the absorption would be so strong that radiation would not be able to escape from the Top Hat. Hence, it can be stated with confidence that the heat leak from the Top Hat does not affect the temperature of the gas sampled by API-V

## §2.1 Instrument description

The design of API-V was based on the principle of measuring the time of flight required for a sound pulse to cross a known distance. In theory the speed of sound could then be trivially calculated by dividing the distance by the time of flight.

The instrument itself consisted of two identical sensor heads (named API-V1 and API-V2) each of which contained a piezoelectric transducer able both to generate and detect a sound pulse. In this way each sensor could be used as both a transmitter and receiver of sound waves.

The two sensor heads were located one at either side of the opening of the Top Hat, and were mounted directly onto its glass fibre reinforced polymer (GFRP) structure as seen in Fig 2.1. The nominal separation from sensor face to sensor face at room temperature was 128.9 mm. This location was chosen for a number of reasons:

1) The location at the bottom of Huygens would have ensured API-V was immersed in liquid if Huygens had landed in a sea or lake.
2) Flow of the atmosphere through the Top Hat and out of the vent pipe ensured constant resampling of Titan's atmosphere during descent.
3) The position at the entrance to the Top Hat gave the most pristine sample possible, minimising heating from the probe.

**Fig 2.2 A cutaway through a single API-V sensor**

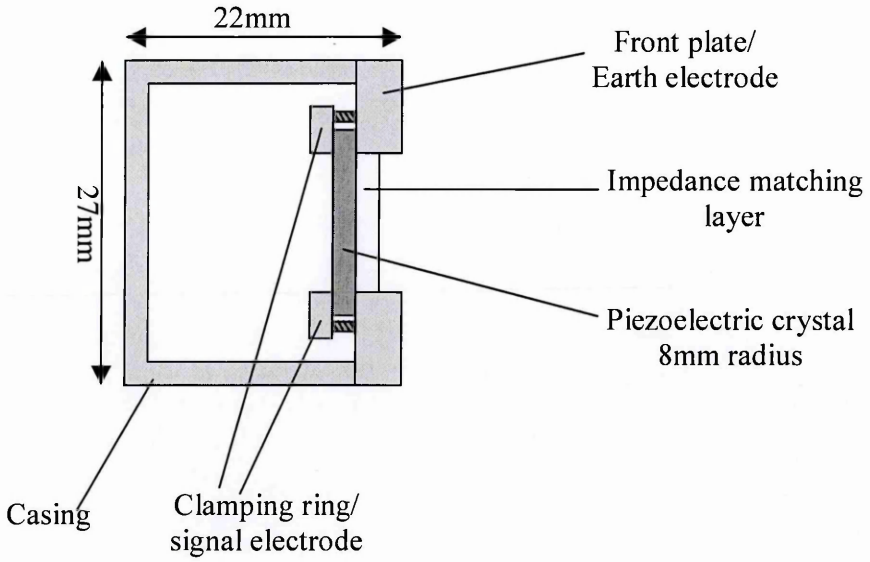


To take a measurement of the speed of sound, API-V1 transmitted a sound wave, and the time taken for this to reach API-V2 was measured. Specifically, the time from beginning transmission to the time at which the voltage on the receiving sensor crossed a threshold was measured. This process was then repeated with the roles of the sensors reversed. One pair of these measurements was made every second during the mission, starting just 600 seconds after the first parachute was deployed at an altitude of approximately 122 km. However it was expected that the tenuous atmosphere at such a great height above the surface would not allow transmission of sound to and from the sensors efficiently enough to allow measurements to be taken successfully. Switching on so early in the mission ensured that measurements would be taken as soon as the signal was strong enough i.e. at the greatest altitude possible.

A schematic diagram showing one of the sensor heads is given in Fig 2.2. The crystals are positioned at the front of the sensors, clamped in place at four points around their circumference, which, in addition to holding the crystals in position, form the electrical contacts. The front clamps act as an earth contact and the rear clamps act as an applied or measured voltage contact when used in transmitter or receiver mode respectively.

The crystals themselves were made of discs of 8mm radius and 2mm thickness PXE 5, a modified lead zirconate titanate (generally referred to as pzt). PXE 5 has a very low quality factor Q (Stretton 1965). The Q-factor is a measure of how quickly the vibrational energy of the material is dissipated as heat. It is defined as the number of cycles required for the system's vibrational energy to fall by a factor of $e^{2\pi}$, hence a system with a low Q-factor will be more heavily damped than an equivalent system with a high Q-factor. The low Q-factor of PXE 5 (approximately 80 compared with up to 500 for other PXE grades) renders it ideal for non-resonant sensing applications (Ejakov, et al. 2003). To maximise the transmission of sound between the piezoelectric crystals and Titan's atmosphere an impedance matching layer was added to their front surface. The impedance matching layer consists of a ~0.7 mm thick disc of Scotchply® brand XP-241-36 Type I syntactic foam. Using available room temperature data for the acoustic impedance of PXE 5 and the syntactic foam with expected values for Titan's atmospheric acoustic impedance, the effect of the foam has been calculated. It was found to increase the transmission coefficient, for the amplitude of the wave, from sensor head to sensor head, from approximately $1.5\times10^{-3}$ to approximately $5.3\times10^{-3}$. This is more than a three-fold increase.

## §2.2 Measurement technique

In order to appreciate fully the data returned from API-V, it is essential to understand the process by which each measurement was taken. An electronic circuit, without any software or programmable component, drives the sensors. The electronics simply react to an input pulse (start signal) which initiates a measurement. The electronic systems used can be conveniently divided into three parts, shown diagrammatically in Fig 2.3. The system functions as follows:

1) The sound generation electronics produces a 1 MHz square wave pulse of duration 10 μs and peak-to-peak amplitude 20 V for use as the transmission signal. This signal is passed to the transmitting sensor by a solid state switch.

2) The receiver detects this signal and the solid state switch directs it to the detection electronics. Here it is first passed through a 1 MHz filter and then through a low noise amplifier. Finally, the signal is passed to a voltage comparator which continuously compares the signal to a voltage threshold of 69.9 mV and triggers as soon as the signal voltage is larger than this threshold.

3) To derive the speed of sound the timing electronics uses a counter to record the time between transmission of the sound wave and triggering of the voltage comparator. The timing electronics count pulses from a 4 MHz clock, giving 0.25 μs resolution.

**Fig 2.3 Diagram showing how API-V is used to measure the speed of sound**

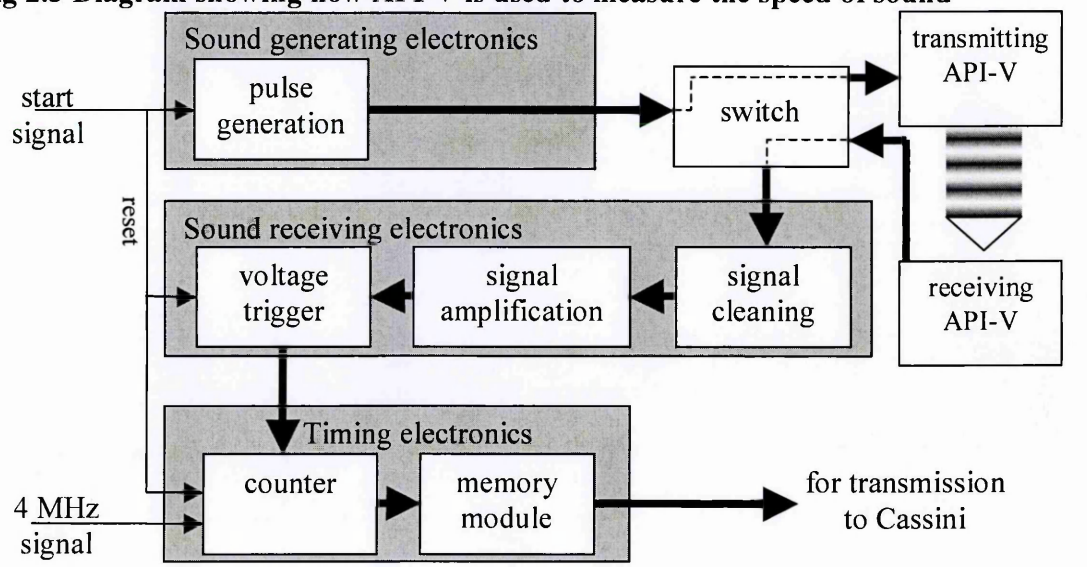


This measurement process is initiated by the start signal which resets the voltage comparator, restarts the counter and causes the sound generation electronics to begin producing the wave train as shown in Fig 2.3. After 2 ms the value on the counter is read into the memory module and stored for transmission to Cassini. The solid state switch then swaps the function of transmitting and receiving sensor heads and the process is repeated.

It is worth noting that if the voltage on the receiving electronics never crosses the threshold of the voltage comparator a timeout value of approximately 2 ms will be recorded. Also, as

a precaution to avoid crosstalk between the transmitting and receiving electronics falsely stopping the counter, a blanking window of 50 μs is used, during which time, the voltage comparator cannot trigger.

The pulse frequency was chosen to be 1 MHz in order to minimise absorption while maximising resolution. Depending upon the amplitude of the wave the trigger can occur anywhere along the quarter of a wavelength where the signal is greater than zero and rising. Increasing the frequency reduces this time period, therefore increasing resolution. Classical absorption, however, can be shown to be approximately proportional to the frequency squared (Herzfeld & Litovitz 1959). Classical absorption occurs due to shear viscosity, molecular diffusion, and thermal conduction and radiation processes, where heat is transferred from warm compressed regions of the waveform to colder rarefied regions. It is easy to see that both these effects will increase with increasing frequency and in particular the classical absorption coefficient increases greatly for frequencies over ~2 MHz. Absorption also occurs due to excitation and relaxation of internal energy levels such as molecular vibrational and rotational excitation levels. This process is caused because energy is transferred between the translational and internal degrees of freedom exponentially with a time constant $\tau$. If the frequency of a sound wave is close to $1/\tau$ then significant absorption will occur (Dain & Lueptow 2001b). Methane has a vibrational energy level with a relaxation time of 2 μs at room temperature (Stretton 1965) which creates an absorption peak around 0.1 MHz (Dain & Lueptow 2001a; Ejakov, et al. 2003). Avoiding this absorption peak may also have been a factor in deciding the frequency used, however, post launch investigations have found that the vibrational absorption drops significantly with temperature (Dain & Lueptow 2001a) to the point of being negligible at Titan conditions.

### §2.2.1 Instrument Characterisation

Although the principles behind the sensor are relatively straightforward - simply measure the time and use the separation measured before launch to determine the speed - it was important to verify that the sensors performed as expected in the laboratory. Some instrument characterisation work had been performed on the flight models pre-launch (Garry 1996). In this work the API-V sensor heads were driven either by a signal generator or by the flight electronics and the signals were monitored on an oscilloscope. Nitrogen, methane and argon gases were used with the time of flight being measured by comparing points of constant phase on the transmitted and received wave trains. These time of flight measurements were used to calculate speeds of sound and uncertainties were estimated to be around 1 m $s^{-1}$.

In order to characterise further the system used in this work, the flight spare model was used under a variety of conditions and the results compared with expected values. In order to carry out this characterisation a small atmospheric chamber was used. This was the same chamber as used by Garry (1996) for pre-launch characterisation with modifications made as appropriate.

A schematic drawing of the chamber is given in Fig 2.4. The chamber was constructed of stainless steel and consisted of two cylindrical tubes, one shorter and with a smaller radius than the other. Each cylinder had a closed end and a flanged end, meaning that when the smaller was placed into the larger and the flanges bolted together a small enclosed experimental volume was formed. A large O-ring was used to ensure a good seal and an inlet and outlet were provided for experimental gases.

Seven electrical feeds were provided for in the form of an off-the-shelf fitting attached to the gas outlet and for some experiments a pressure regulator was fitted. Another pressure release valve was added for safety and all gases were vented outdoors. The API-V sensors were mounted inside the chamber on small blocks attached to the lid. This lifted the

sensors away from the lid in order to reduce the effect of acoustic reflections off that surface.

The chamber was cooled by submerging it in liquid nitrogen and allowing it to reach equilibrium at typically around 85 K. The nitrogen was then allowed to evaporate away causing the chamber to warm slowly through the temperature range of interest. The rate of change of temperature while measurements were taken was typically less than 1 K $min^{-1}$ and through the Titan temperature regime it was typically 0.3 K $min^{-1}$.

**Fig 2.4 Schematic drawing of the atmospheric chamber used for characterisation of API-V. The inner chamber has a diameter of 148 mm and a height of 81 mm. This produces a working volume of approximately 1.4 litres.**

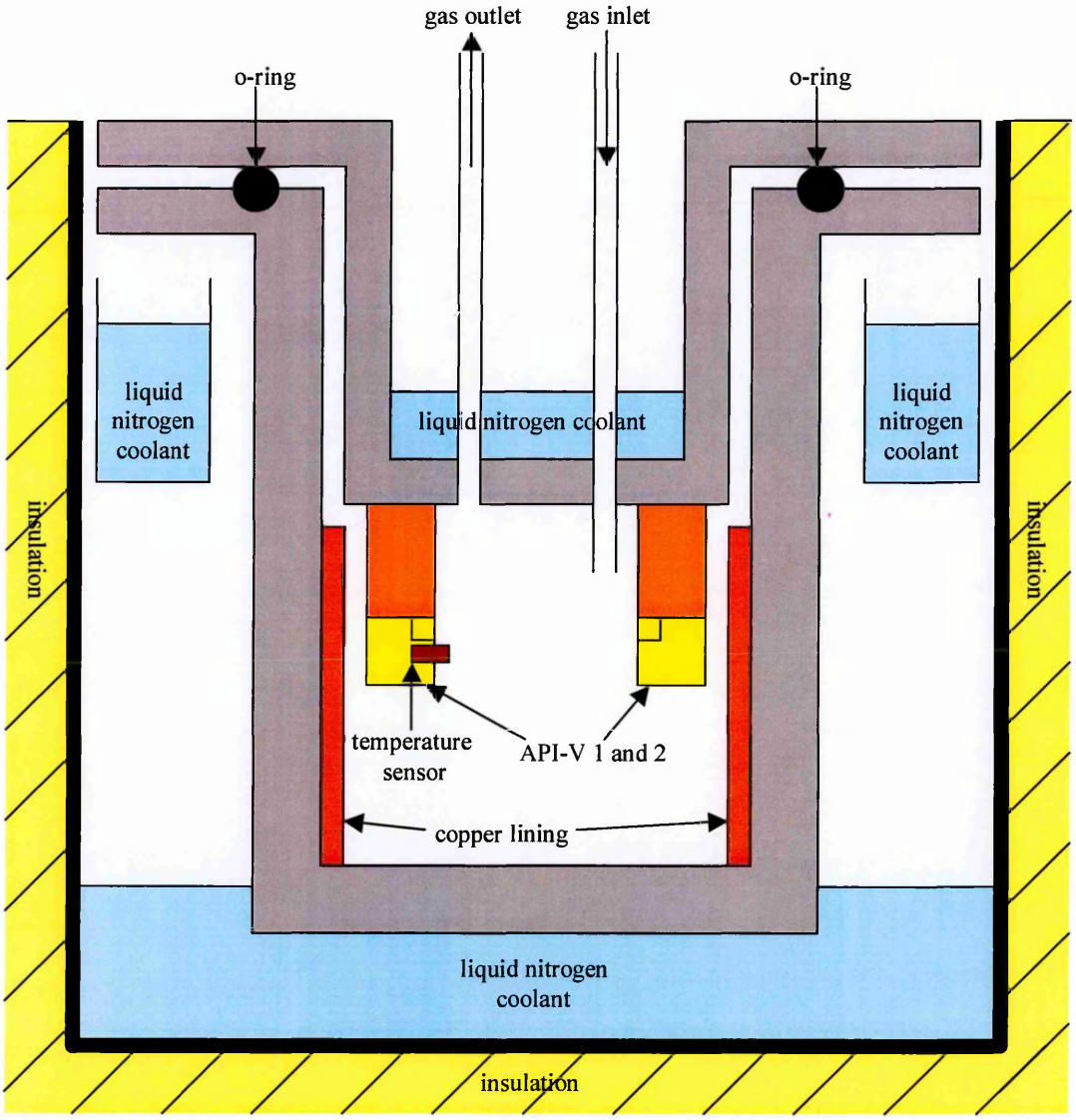


## §2.2.2 Initial characterisation

Initially, the chamber was run with a flow through of gas ensuring measurements were made at approximately atmospheric pressure. The chamber was first purged by allowing gas to flow through the chamber at a high rate. The flow rate was then reduced to the lowest value that would register on an inline flow meter. The inflowing gas was pre-cooled as it entered the chamber by passing it through a copper coil suspended above liquid nitrogen. The temperature was measured using a rhodium-iron resistance temperature

detector (RTD) powered by a previously constructed electronics box and logged on a PC via a PICO™ 12 bit analogue to digital converter.

The API-V sensors were driven by the SSP engineering model electronics package and the measurements were downloaded from the electronics onto a PC. The results of these initial runs using nitrogen gas with the sensors at two different separations are shown in Fig 2.5, Fig 2.6 and Fig 2.7 along with the expected ideal gas values.

It is clear that the API-V measurements do not agree with the ideal gas approximation. Although at low temperatures this may be expected to be the case, nitrogen does behave as an ideal gas at room temperatures and consequently the data should be expected to match here. This difference may have been caused by incorrect temperature measurements; or perhaps problems caused by gas flow into the chamber.

**Fig 2.5 Plot showing initial measurement of time of flight for a sound wave measured with a sensor separation of 55.1 mm. The solid line is the expected time of flight assuming ideal gas conditions.**

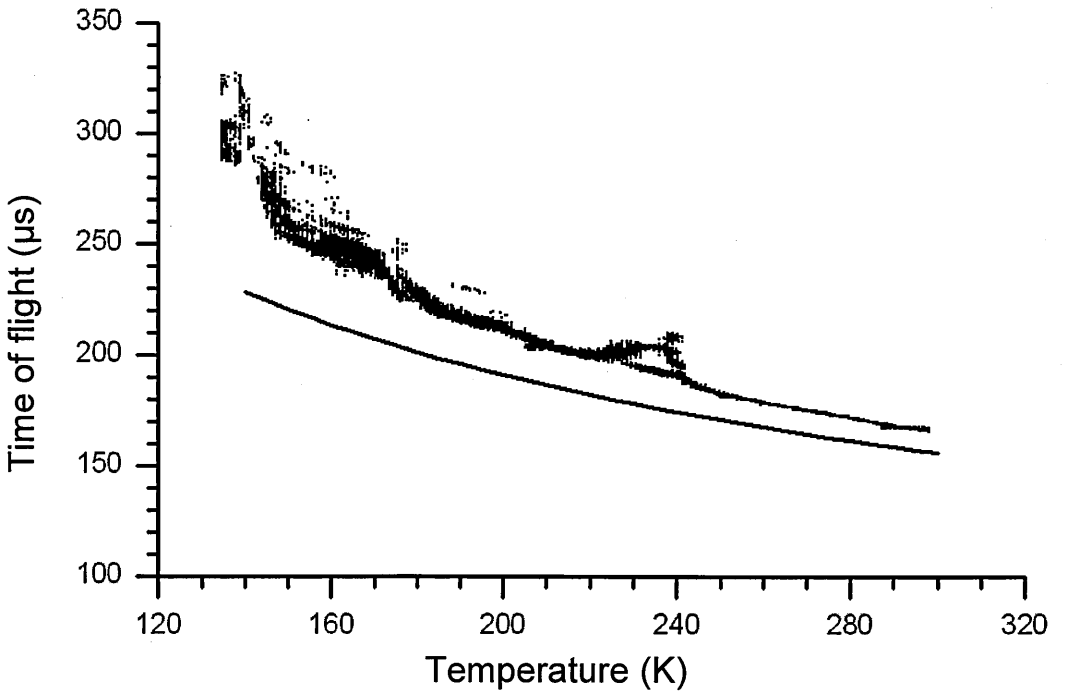

**Fig 2.6 Plot showing initial measurement of time of flight for a sound wave measured with a sensor separation of 83.0 mm. The solid line is the expected time of flight assuming ideal gas conditions.**

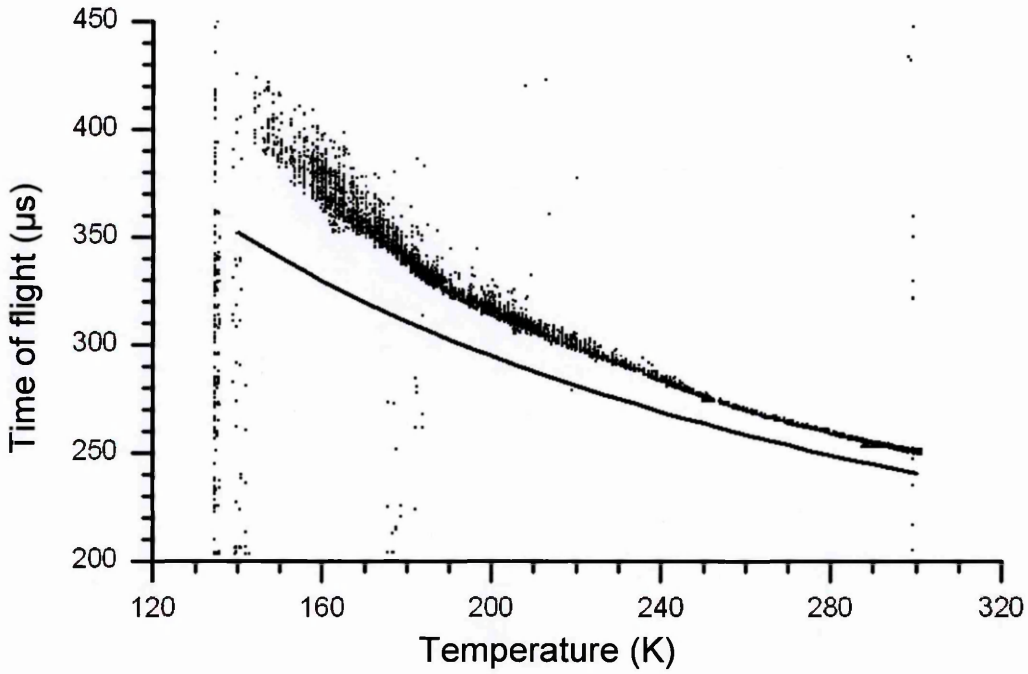


**Fig 2.7 Plot showing speeds of sound calculated for nitrogen from time of flight data measured by API-V at two different separations (as plotted in Fig 2.5 and Fig 2.6) with the expected ideal gas value shown for reference.**

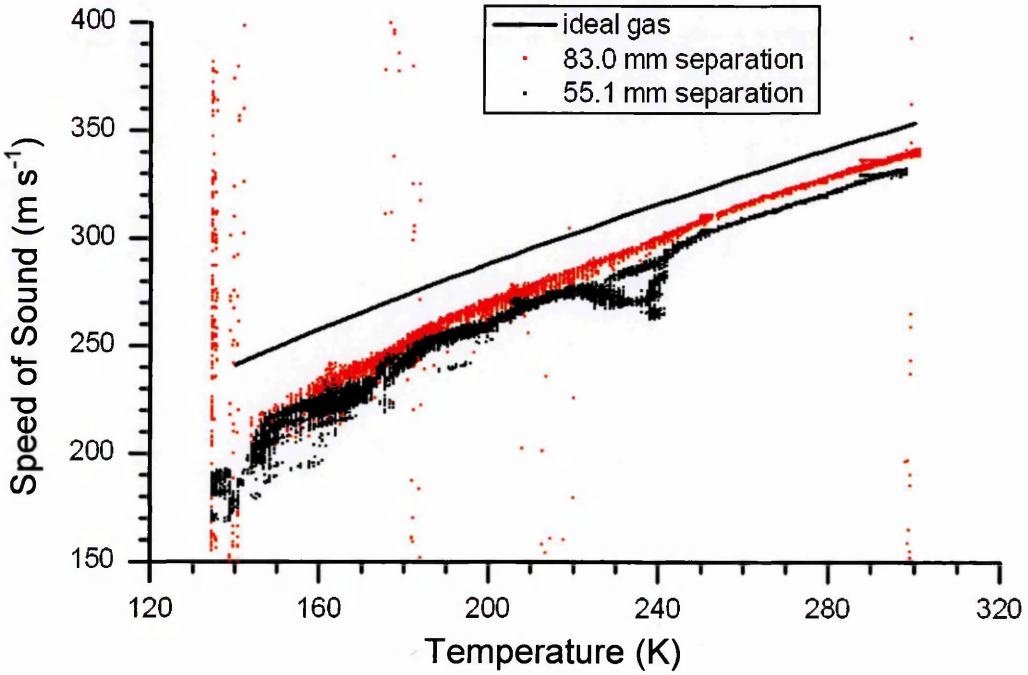

Another obvious problem evident in Fig 2.7 is that the two different separations produce different values for the speed of sound. This may indicate the presence of a systematic offset in the measurement, specifically a time delay in the system. Such a delay would cause an underestimate of the speed of sound which would increase with decreasing separation. The temperature measurement and systematic offset issues both required actions. These are discussed, in turn, in the following sections.

In addition Fig 2.5 shows some structure in the data beyond simply the smooth change with temperature that was expected. This could have been caused by gas flow in the chamber or reflections/resonances from the sensors' casings.

### §2.2.3 Temperature measurement

Comparison between the RTD and a mercury thermometer at room temperatures indicated a discrepancy of around 7-8 K. This probably should not have come as a complete surprise as the drive electronics were of an unknown design and had not been calibrated with the RTD, although a calibration curve had been provided with the RTD when purchased. The drive electronics were replaced with a Lakeshore Model 331S temperature controller and a four wire setup was used to ensure maximum accuracy. In this method two connections are used to supply a 1 mA constant excitation current through the RTD and the further two connections are used to measure the voltage dropped across the sensor. As a constant current flows through the current connections and negligible current flows through the voltage connections any uncertainties caused by wire resistances are eliminated. Hence, maximum accuracy can be achieved.

The use of a rhodium-iron RTD is acceptable in our temperature range of interest and studies have found rhodium-iron measurements to be extremely repeatable (Besley 1985). The new setup with a low excitation current should allow an accuracy of around 0.1 K to be achieved. However, Besley found that rhodium-iron sensors need settling by repeated cycling to cryogenic temperatures. This is achievable by simply immersing the sensor into

liquid nitrogen 10 times. This settling procedure is reversed by exposing the sensor to temperatures much in excess of room temperature. In addition it was found that exposing the sensor to very high temperatures, such as during soldering, could permanently alter its resistance characteristics. This is attributed to relaxation of stresses in the sensor during heating. As our sensor had been soldered a number of times since its initial calibration, it was put through the cryogenic cycling process and a two point recalibration process was performed. In this process the resistance of the sensor was measured by the temperature controller in a deionised water ice bath and also in liquid nitrogen. The results are shown in Table 2.2. Just by altering the drive electronics and switching to a four wire setup the accuracy has been greatly improved, giving accuracies around $0.2 - 0.3$ K. However, to achieve the 0.1 K accuracy that should be possible with this system, the two calibration points have been used to generate a weighting function to correct the previous calibration curve. If the previous calibration function gave temperature T' as a function of resistance R then the new calibration curve can be given by

$$T(R) = W(R)T'(R). \qquad \textbf{Eq 2.6}$$

Here W(R) is the weighting function determined from a linear interpolation through the two new calibration points. In this case W(R) was found to be given by

$$W(R) = 0.99592 + 1.12 \times 10^{-4} R, \qquad \textbf{Eq 2.7}$$

with R expressed in Ohms. The final calibration curve can be found in Fig 2.8.

**Table 2.2 Calibration points for rhodium-iron RTD**

| Calibration point | RTD Resistance | Temperature using old calibration |
|---|---|---|
| Nitrogen boiling point 77.28 K (at 1009 mbar) | 6.844 Ω | 77.54 K |
| Deionised water ice point 273.15 K | 27.051 Ω | 273.38 K |

Unfortunately, with the new electronics in use and working no comparison with the original setup was made. This means that it is impossible to retrospectively correct the temperature data used in Fig 2.5 and Fig 2.6.

In addition to the temperature sensor overhaul, problems caused by gas flow through the chamber also needed to be solved. The gas flowing through the chamber would have caused a number of problems. The gas coming into the chamber was not generally at the same temperature as that already inside. The gas was pre-cooled but no attempt was made to match the temperatures directly. As the speed of sound is very dependent upon temperature, the inflowing gas would have significantly effected the measured time of flight.

**Fig 2.8 Calibration curve for the atmospheric chamber's rhodium-iron temperature sensor.**

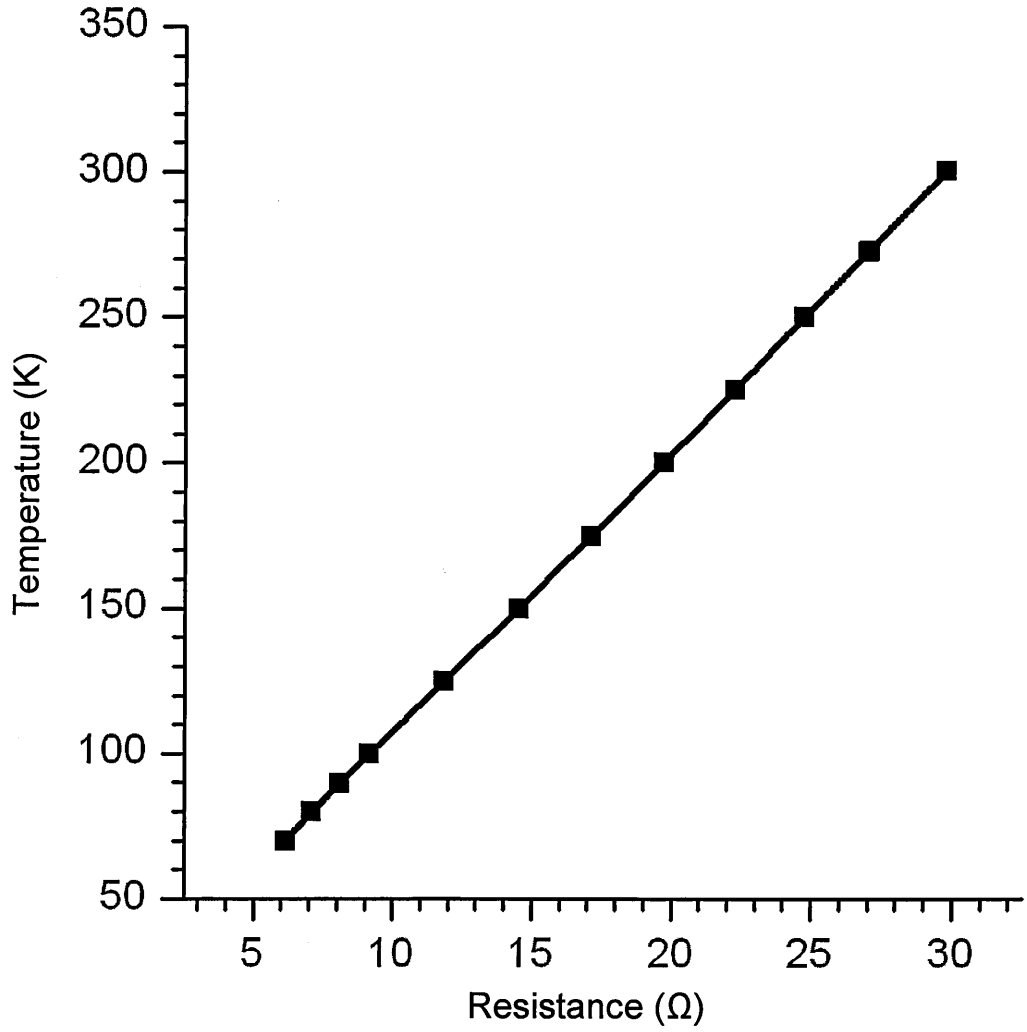


In addition, as the sound waves travel into the inflowing gas, they would have been refracted due to the change in travel speed. At low temperatures where the gas has a low viscosity and high density the Reynolds number of the flow may have been high enough to

produce turbulent flow into the chamber. It is reasonable to expect that a turbulent and constantly changing boundary between the gases of differing temperatures would cause the measured time of flight to vary from one measurement to the next. This may be the cause of the increased scatter at lower temperatures seen in Fig 2.5, Fig 2.6 and Fig 2.7. The flow of different temperature gas into the chamber rendered any temperature measurements difficult to interpret, as the gas in the chamber would not have been isothermal. In order to alleviate this problem the chamber was redesigned allowing it to be used without a flow through of gas. An inline pressure regulator was installed to allow gas to enter the chamber during cooling and then vent it while warming. The regulator could be adjusted to maintain the pressure to a particular value, however, when tested, some hysteresis was noticed as the regulator vented gas. This hysteresis allowed the pressure within the chamber to vary by approximately 200 mbar while using the chamber.

### §2.2.4 Detailed Characterisation

The initial characterisation of the sensor had led to the conclusion that there was a systematic offset occurring in our measurements. After upgrading the atmospheric chamber with increased accuracy temperature sensing and the ability for it to be used without flowing gas this offset could be measured effectively.

The increase in measured sound speed with decreasing sensor separation must come from either a systematic underestimate of the separation or a systematic overestimate of the time of flight. It is difficult to imagine a way in which the separation could be underestimated as this is directly measured, however, a number of possible sources of delay in the system exist that could cause an overestimate of the time of flight:

- Electronics delay. Each active element in the electronics that the signal passes through will add a small delay to the time measured. Typical slew rates for op-amps used are ~100 V/ns and typical propagation delays for other digital

components are 30 ns. This would lead to a total electronic delay of the order 100 ns.

- Crystal delay. Each crystal has a non-zero capacitance and a small but non-zero inertia. This means that there is a time delay between the voltage being applied to the crystal and it reaching the appropriate displacement. This can be seen by connecting an oscilloscope across a transmitting crystal. The pulse looks roughly sinusoidal compared to the driving square wave; this implies that the crystal does not reach, or only just reaches, its maximum displacement before the applied voltage swaps polarity. In addition, at the beginning of the pulse, the crystal is starting from zero displacement and zero velocity so there is a short time delay measured to be around 100 ns to allow the voltage across the crystal to build up and the crystal to accelerate.
- Sound travelling through the sensor. When sound is generated by the PXE5 crystal it must pass out of the crystal and through the impedance matching layer before it reaches the atmosphere. It must also pass through a similar layer before reaching the receiving crystal. The speed of sound in the impedance matching layer at room temperature is 2550 m $s^{-1}$. Therefore, using the 0.7 mm thickness stated in §2.1 gives a delay of 0.55 μs. In addition to this the crystals have a finite thickness, generating and sensing sound throughout this thickness. The speed of sound in PXE 5 is 3700 m $s^{-1}$ and with a thickness of 2 mm it would take a sound wave 0.54 μs to pass through a crystal.
- Missing Peaks. As the voltage pulse is converted to a sound wave, which then travels the distance between the sensor heads and is converted back to a voltage, its shape changes from a square wave to a dispersed wave pulse (Fig 2.9). Because of this the first few peaks in the received signal are significantly smaller than those later in the signal and may be missed. For every peak missed a delay of 1 μs is created. In flowing turbulent medium it may be that the signal is degraded and

many peaks are missed; however, even in perfectly still, ideal conditions one or more peaks are reproducibly missed by the sensors.

Clearly the total offset can be expected to be of the order of a microsecond or more. The offset could also be temperature dependent so should be measured under Titan-like conditions.

**Fig 2.9 Plot showing a typical received signal using the flight spare API-V sensors in the laboratory.**

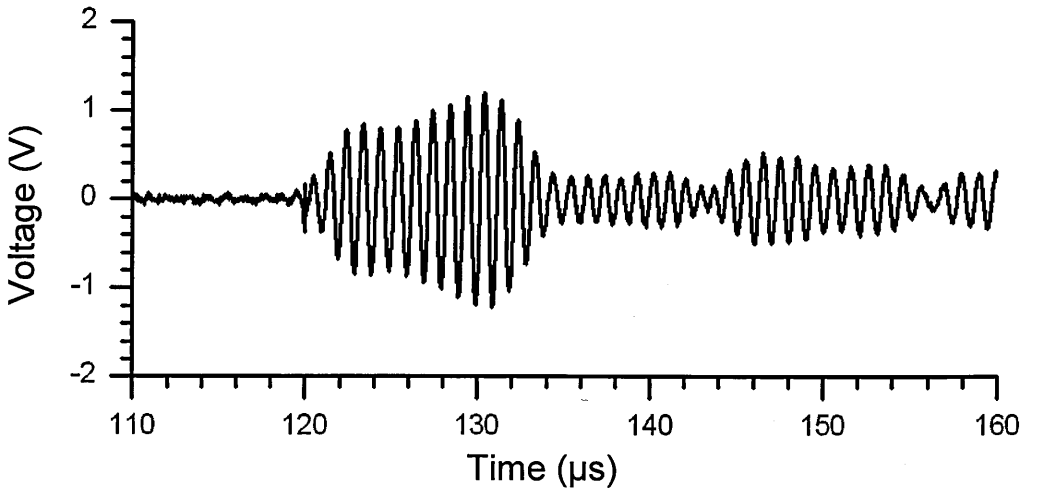


In order to measure the time offset, a pair of metal bars was manufactured that straddled the two API-V mounting blocks. The bars had a series of threaded holes to allow the sensors to be mounted at various different separations and using these mounting bars allowed the time of flight to be determined over these different distances. Plotting time of flight against separation yields the speed of sound from the gradient and the time offset from the intercept on the time axis. In this way the offset can be measured directly without reliance upon a speed of sound model, which may introduce its own systematic errors.

During the experiment API-V was driven by the engineering model electronics. However, a digital oscilloscope was connected directly to the electronics board to permit detailed analysis of the results. The start signal was employed as a trigger for the oscilloscope and the received signal was recorded by connecting the oscilloscope after the cleaning and

amplification stages but before the voltage trigger. See Fig 2.3 for details of the electronics chain.

The experiment ran over five sessions using nitrogen in the chamber. In each case the atmospheric chamber was cooled using liquid nitrogen to around 80 K, with the pressure regulator set to maintain the pressure around 1400 mbar. This pressure not only mimicked the surface pressure on Titan, but also ensured a positive pressure was maintained in the chamber. Consequently, any poor seals did not allow atmospheric gases to enter the chamber. This did, however, cause some problems at very low temperatures. As the chamber cooled the vapour pressure of nitrogen was depressed until it reached 1400 mbar at which point the nitrogen began to condense. This was evident during the experiments from an increased flow of nitrogen into the chamber as the regulator attempted to maintain the pressure at 1400 mbar. This could cause problems, as an abrupt rise in temperature that would cause the condensation in the chamber to boil may generate turbulence within the chamber therefore degrading results. A significant safety risk could also be posed if the regulator was unable to vent the gas fast enough. In order to minimise the safety risk the gas flow was switched off when condensation began to occur. Once the chamber had cooled to around 80 K the liquid nitrogen coolant was allowed to evaporate away and the chamber was allowed to warm up to ambient temperature slowly.

The oscilloscope and temperature controller were both connected to, and monitored by, a PC using a General Purpose Interface Bus (GPIB, also known as an IEEE-488 bus). At one Kelvin intervals a program on the PC recorded the trace from the oscilloscope and logged the temperature. The C++ code for this program is included in the appendix. Unfortunately, a pressure sensor with a PC logging facility was not available. Instead a webcam was set up and the logging program photographed the digital display of the sensor whenever a measurement was saved to the PC. The digital photographs were then manually transcribed after the session was complete. The complete setup is shown in Fig 2.10.

**Fig 2.10 Layout of system for calibration of API-V. Elements are 1) Sun computer for controlling Surface Science Package electronics; 2) Surface Science Package flight spare electronics; 3) oscilloscope; 4) pressure sensor; 5) atmospheric chamber; 6) web cam for recording display of the pressure sensor; 7) PC for logging data; 8) temperature controller.**

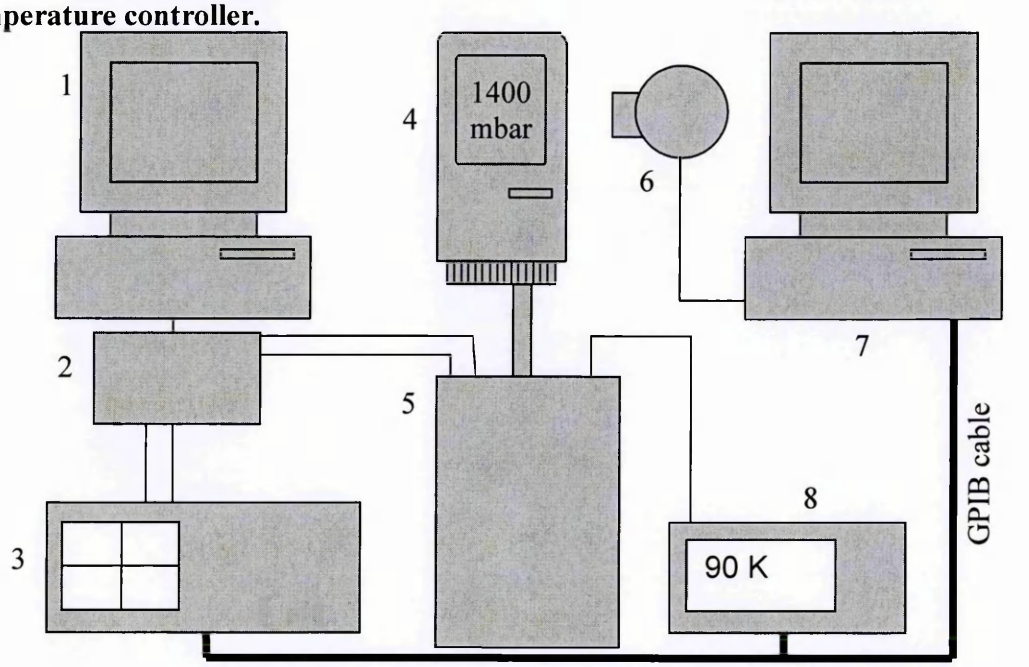


Once the data for a session was collected each trace was examined to determine the time between the start signal triggering the scope and the received sound signal crossing a threshold of 0.2 V. The electrical noise in the laboratory forced such a high threshold to be used despite it being nearly three times larger than the 69.9 mV value used on Huygens. However, the separation of the sensors in the cryogenic facility was smaller than that on Huygens and it is expected that classical absorption and spreading of the wave front would have caused the signal amplitude to be larger by a similar factor. Logging the oscilloscope trace and checking the time of flight in this manner was, however, preferable to using the time measured by the SSP flight spare electronics for a number of reasons:

- False triggers caused by noise, crosstalk or spikes in the signal could be filtered out.
- There was a significant download time to take measurements from the engineering model electronics to a logging PC. It was not known how this would effect time-stamping of the data. This uncertainty in the time each measurement was taken would create an uncertainty in the temperature at which the measurement was taken, possibly of the order a few Kelvin.

- The trigger on the engineering model electronics was not set identically to the flight model. In particular, the engineering model voltage trigger was set at a negative voltage, whereas the flight model was believed to be positive.

Five different separations were used to determine the offset. These were approximately 78, 64, 50, 36 and 22 mm, although corrections were made for the thermal contraction of the bracket at low temperatures.

It had been hoped that the results could be used to determine the offset independently of any speed of sound model. However, at low temperatures, where the pressure dependence of sound speed increases, it appears that the limited control of the pressure introduced a significant scatter into the measurements. In particular the pressure during the measurements made at ~36 mm separation was much lower than the other sessions, perhaps because less nitrogen condensed in the chamber. The pressure profiles of the sessions are shown in Fig 2.11.

In order to attempt to compensate for this effect a pressure corrected time of flight $t_{corr}(T,P)$ was generated from the measured time of flight, $t_{measured}(T,P)$, and a predicted time of flight generated by a non-deal equation of state $t_{predicted}$ by

$$t_{corr}(T,P) = t_{measured}(T,P) - t_{predicted}(T,P) + t_{predicted}(T,1500/\text{mbar}) \qquad \textbf{Eq 2.8}$$

The equation of state used was supplied by the National Institute of Standards and Technology (NIST) and will be discussed further in Chapter 3. The measurement of the offset is now no longer independent of a speed of sound model; however, this process is still preferable to simply comparing the measured time of flight to a predicted value. Comparing the measured time to the expected time would introduce a model dependant, systematic uncertainty, based upon the strong dependence between the speed of sound and temperature. Using Eq 2.8, the uncertainty introduced is based upon the much weaker relationship between the speed of sound and pressure.

**Fig 2.11 Plot showing how pressure varied in the atmospheric chamber as it warmed during each measurement session**

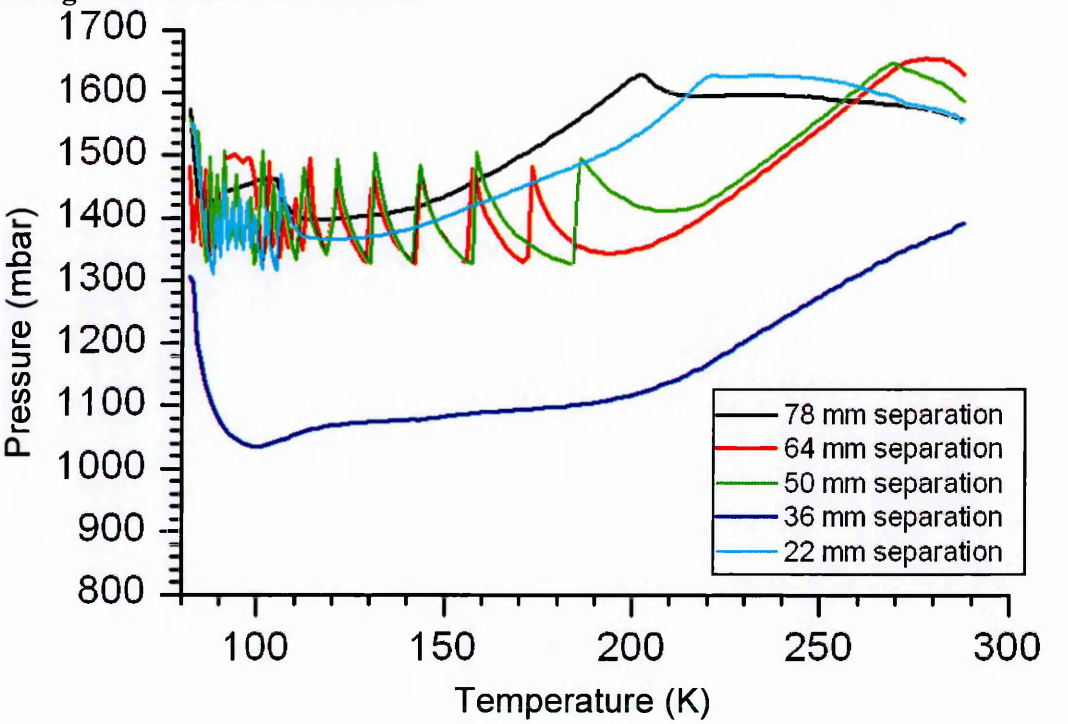


The only significant change made by this correction process is to increase the time of flight around 90-100 K for the 36 mm separation measurements. This is as would be expected, as the pressure dependence of the speed of sound increases with decreasing temperature and the pressure difference between the 36 mm separation measurements and the others is at its maximum in this temperature range. The result is to raise the measured offset in this temperature range by around 0.5 μs.

For each separation that was used a time of flight measurement was made at every integer temperature value throughout the range 82-288 K. For each temperature value a plot of separation vs. time of flight was produced. The intercept on the time axis of this plot was calculated and it is this value that represents the time offset in the measurement. An example, showing one of the 207 plots can be found in Fig 2.12.

**Fig 2.12 Plot showing the time of flight measured using the API-V flight spare sensors at different separations in nitrogen at 88 K. Uncertainties on the points are approximately the same size as the points themselves. The insert shows a zoomed view of the origin where a straight line fit has been extrapolated to the y axis. The plot shows an intercept of 3.48 ± 0.7 μs rather than passing directly through the origin as expected and indicating an offset in the API-V measurements.**

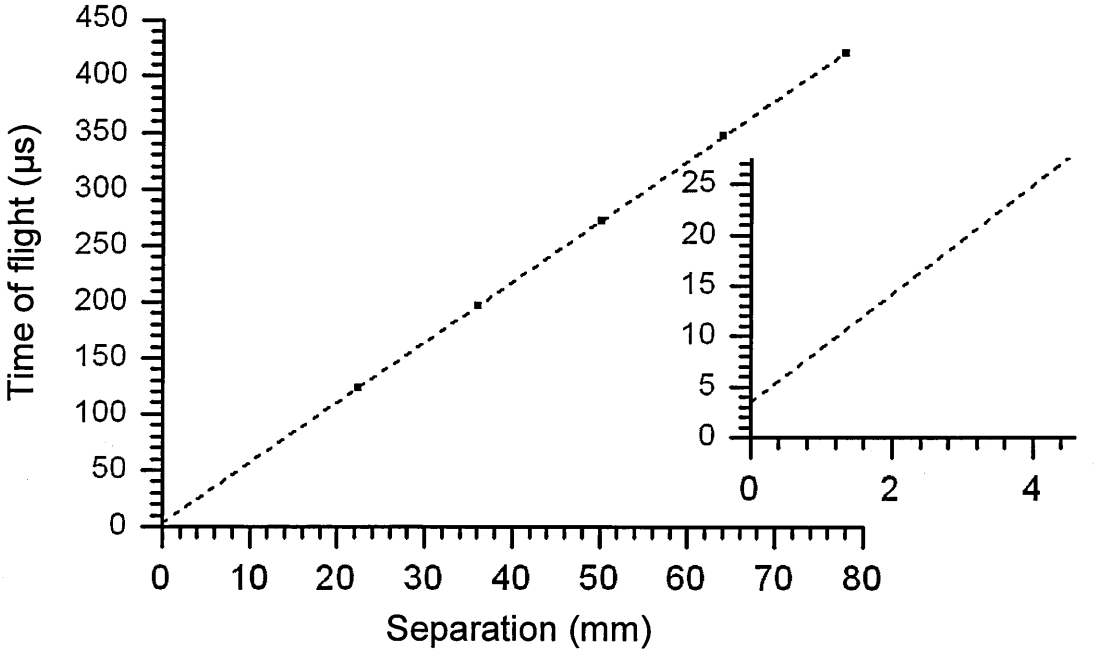


The offset measurements are presented in Fig 2.13 for all temperatures from 82 K to 288 K. The one-sigma error bars on each data point are derived from the scatter of the straight line fit between time of flight and separation. The plot seems to show a horizontal line with little deviation above 170 K. Below this temperature the data has a larger scatter, although this is appropriate as the error bars for these data points are also larger. This increased uncertainty is probably due to the difficulty maintaining accurate pressure control discussed earlier. The three leftmost data points all show slightly larger values for the offset. The uncertainties on these points, however, are large and it seems unlikely that this is a significant rise. The null hypothesis, that there is no dependence of the offset upon temperature, seems appropriate. To test this null hypothesis the correlation coefficient for the data in Fig 2.13 has been calculated. It's value is 0.07 showing a very low correlation. In addition a linear fit to the data gives a gradient of $5\times10^{-4}$ K $s^{-1}$. Based on this evidence it is appropriate to conclude that there is no temperature dependence in the offset. Taking a

**Fig 2.13 Plot showing the time of flight offset calculated at different temperatures from 82 to 288 K**

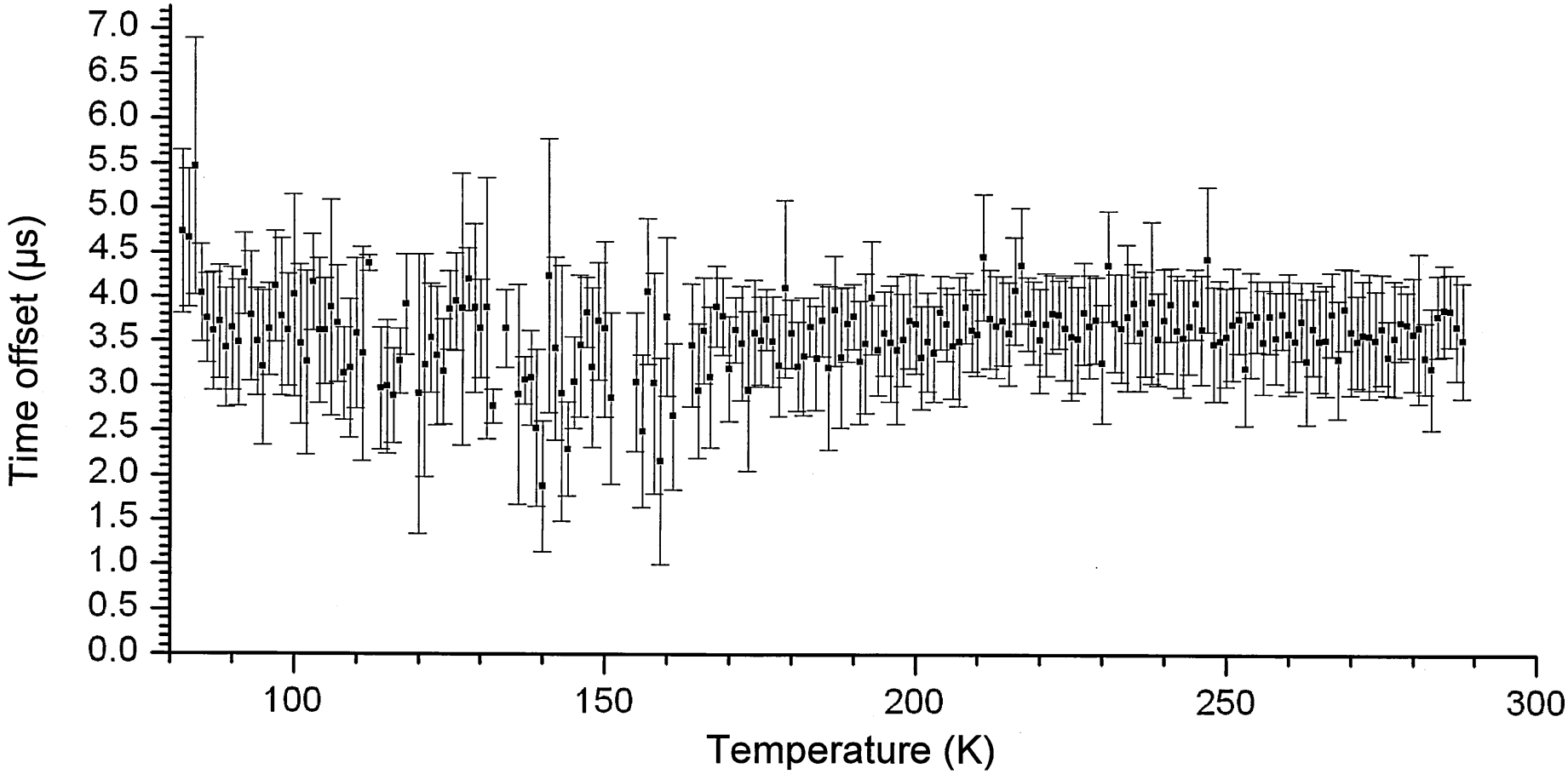

weighted mean of all the measured values results in an offset of 3.71±0.04 μs. 174 of the 188 data points (93%) lie within 1 error bar of this value.

It is also of interest to use the gradient of our time of flight vs. separation plots to generate speed of sound data. Again, the corrected time of flight measurements were used and the values compared with NIST equation of state predictions at 1500 mbar. The measurements are a good match for the NIST data and of the 188 data points all are within 0.9%, 179 are within 0.5% and 97 are within 0.1%.

### §2.2.5 Top Hat Contraction

Unfortunately, no measurements were made of the amount that the Top Hat would contract under Titan conditions. However, two prototype Top Hats were available that could be examined. One of these structures included an aluminium ring, bonded to the base for extra strength, as used on the flight model.

It is worth considering that the Top Hat is manufactured from a composite glass fibre reinforced polymer (GFRP), a material that is neither homogeneous nor isotropic. In addition, this material is used in a thin layer so there is little scope for averaging out inhomogeneous properties. The result of this is that no two Top Hats are likely to be identical in their thermal contraction properties and that the two prototypes may behave differently to the flight model. However, the two API-V sensor heads are mounted close to the reinforcing aluminium ring. As aluminium has a much higher stiffness than GFRP it may be expected that any stresses caused by different thermal expansion coefficients will result in the GFRP being deformed to match the contraction of the ring rather than the other way around. With this in mind the prototype Top Hat with the aluminium reinforcing ring was chosen as the one most representative of the flight model.

This prototype was cooled to liquid nitrogen temperatures to measure its contraction. The method employed was to measure between 7 pairs of points on the Top Hat at room temperature using digital callipers then submerge the Top Hat in liquid nitrogen. The Top

Hat was then lifted from the liquid nitrogen and one of the pairs of points quickly remeasured. This was repeated for all 7 pairs. Digital callipers were the favoured instrument for measurement, anticipating that the speed with which they could be used would minimise any temperature rise which would occur between lifting the Top Hat from the liquid nitrogen and taking the measurement. The results are shown in Table 2.3. The average fractional change is (-0.37±0.13) % where the stated uncertainty is the standard deviation of the measurements. The uncertainty in this value is rather large. This may be due to the crude manner by which the measurements were taken or to the inhomogeneous nature of the material. However, it is worth noting that the value measured is consistent with the value for aluminium at 80 K of -0.391 %.

**Table 2.3**
**Change in separation between points on a prototype Top Hat caused by cooling to liquid nitrogen temperatures**

| Separation at room temperature (mm) | Separation at liquid nitrogen temperature (mm) | Fractional change (%) |
|---|---|---|
| 93.78 | 93.32 | -0.49 |
| 93.81 | 93.49 | -0.34 |
| 93.88 | 93.5 | -0.40 |
| 93.57 | 93.19 | -0.41 |
| 93.59 | 93.08 | -0.54 |
| 93.65 | 93.47 | -0.19 |
| 208.02 | 207.6 | -0.20 |
| 93.78 | 93.32 | -0.49 |
| 208.02 | 207.6 | -0.20 |
| | Average | **-0.36** |
| | Standard deviation | **0.13** |

During the mission it is expected that gas will have been flowing through the Top Hat and that certainly at the entrance where API-V was mounted, the temperature of the structure would have been very close to ambient. Hence, to estimate the separation of the sensors, it has been assumed that the flight model Top Hat is the same as the prototype measured in the lab, the coefficient of thermal expansion is constant from room temperature to 80 K and that the temperature of the Top Hat was equal to the ambient temperature measured by HASI. This gives a separation at Titan's surface conditions of 128.5±0.1 mm. The uncertainty quoted is simply based upon the standard deviation given in Table 2.3; any

uncertainty due to uncertainty in temperature is small. Changing the temperature by 10 K only alters the separation by 0.02 mm, much less than the 0.1 mm quoted accuracy.

## §2.3 Signal Strength

In order to estimate the altitude at which API-V will begin making successful measurements in Titan's atmosphere it is important to understand how the signal strength will vary with changes in the medium being sampled. As the voltage response of the piezoelectric crystals is proportional to the pressure exerted onto the front face by the sound wave, it is useful to define a transmission coefficient, T, in terms of pressure amplitude rather than intensity, which is a measure of incident energy. If an acoustic wave passes from material 1 to material 2 then the pressure amplitude of the transmitted wave, $P_t$, relative to the pressure amplitude of the incident wave, $P_i$, is given by

$$T = \frac{P_t}{P_i} = \left( \frac{2}{1 + Z_2 / Z_1} \right), \qquad \textbf{Eq 2.9}$$

where $Z_1$ and $Z_2$ are the acoustic impedances before and after the boundary respectively. The acoustic impedance of any material is given by

$$Z = \rho c \qquad \textbf{Eq 2.10}$$

where $\rho$ is the density and c is the speed of sound. An interesting effect is that despite energy being reflected from the boundary, if $Z_2 < Z_1$ the amplitude of the pressure wave can increase. Clearly, as Huygens descends towards Titan's surface, the density of the atmosphere will increase and the speed of sound will change, altering the acoustic impedance and the signal strength.

We can apply Eq 2.9 to every boundary the sound wave passes through to determine an expected combined transmission coefficient, $T_{expected}(Z_{crystal}, Z_{matching\ layer}, Z_{gas})$. The voltage response of the receiving piezoelectric transducer is proportional to pressure. However, it

is then amplified, introducing possible offset voltages. Hence, if the voltage amplitude of the transmitted signal is constant, then

$$V_r \propto A + T_{expected} \qquad \textbf{Eq 2.11}$$

where $V_r$ is the voltage amplitude of the received signal, and A is a constant. This assumes that the sensors emit a plane wave and no absorption takes place.

**Fig 2.14 Plot showing the variation of the peak received signal voltage with the expected transmission coefficient from sensor to sensor.**

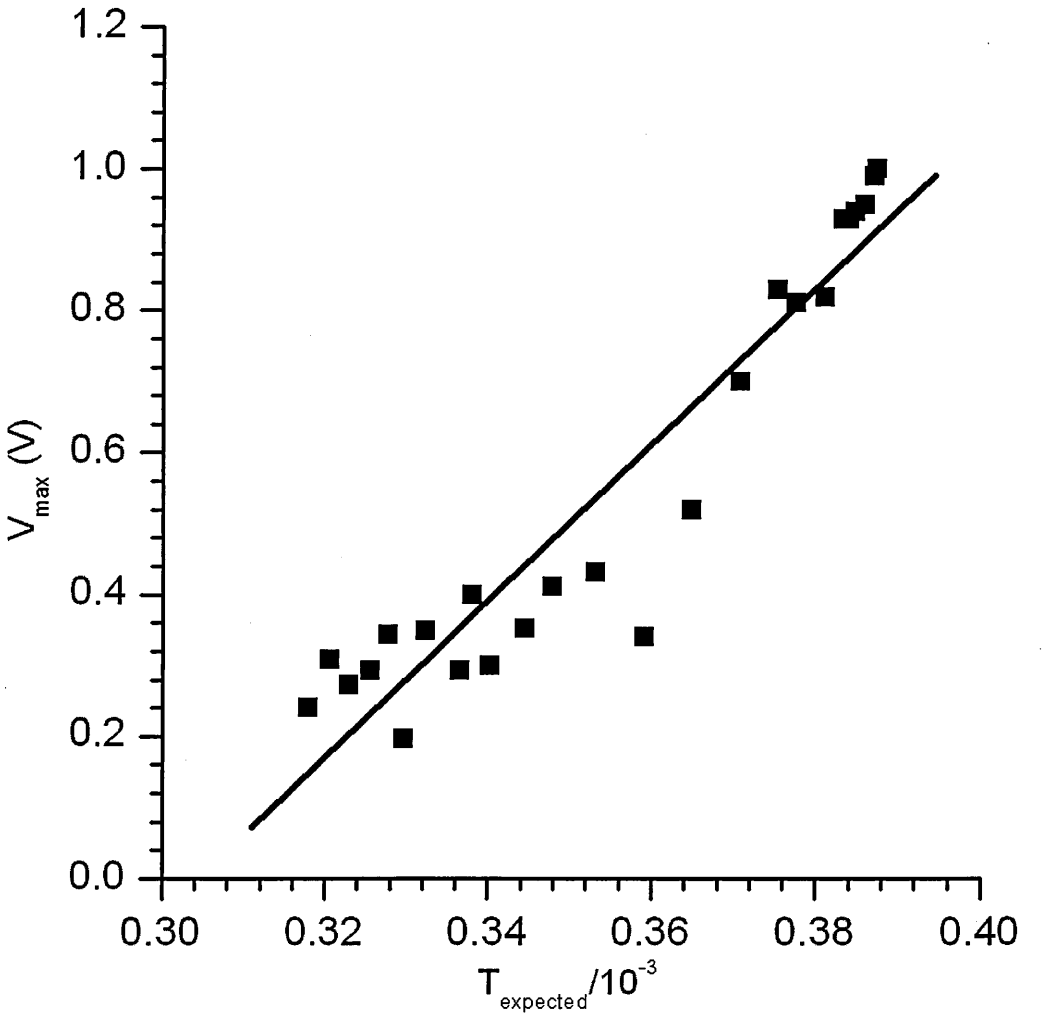


Values for A and the constant of proportionality were determined by experiment using the atmospheric simulation chamber. The chamber was filled with pure nitrogen gas at room temperature then pressure of the chamber was gradually reduced using a vacuum pump in order to reduce the density, and hence acoustic impedance, of the gas. The maximum value of the received signal, $V_{max}$, was recorded and has been plotted against $T_{expected}$ in Fig 2.14.

The data extends only to values of $T_{expected}$ of around $0.32\times10^{-3}$, which corresponds to a pressure of around 850 mbar. Below this pressure the signal was too weak to be reliably distinguished from the background noise level. However, extrapolating a straight line fit just past the lower limit of the data indicates that the flight sensor with a voltage trigger of 69.9 mV will require a transmission coefficient of at least $\sim0.315\times10^{-3}$ which, using room temperature data for the sensor materials, corresponds to a required impedance of the sampled gas of at least ~629 Rayl. Examining the predicted engineering model for Titan's atmosphere, it should have been expected that the sensor would begin to operate at around 10-12 km altitude. As will be seen in Chapter 4, the first successful measurement of the speed of sound was achieved at ~11 km altitude, so at this point the sensors were working as expected.

# Chapter 3
# Speed of Sound

The speed of a sound wave as a diagnostic of composition of gas is something we have probably all seen performed when someone's voice becomes high pitched if they breathe helium. In this case the speed of sound is greater in helium than in air, and hence the resonant frequency of the person's throat increases in proportion to this. From this simple example, it is easy to imagine that the speed of sound can be used as an indicator of composition. In order to do this, however, *a-priori* knowledge must exist defining the speed of sound in different fluids. In addition, if mixtures of fluids are to be considered then the way in which the speed of sound varies with mixing ratio must be known also.

This chapter describes how a wave propagates through a medium and from this, demonstrates how the speed of sound in gases can be predicted. Particular reference is made to Titan's atmosphere, where the ideal gas law cannot be applied. Both pure fluids and mixtures are considered.

## §3.1 Wave Propagation in a Medium

To describe a sound wave in its most general form a property of a medium, y, is considered to vary along the x direction at a given time. We can therefore describe y as a function of x

$$y = f(x) \,. \qquad \textbf{Eq 3.1}$$

This is clearly a very general statement; however, for a periodic wave, y represents any periodically varying property (such as the transverse displacement of a string or variation of pressure in air) and f would be a periodic function which, for example, could be as simple as a sinusoid or a more complex Fourier series. If the wave is moving in the x direction with a velocity c, but otherwise does not change, we can incorporate this movement over time, t, by altering Eq 3.1 to

$$y = f(x - ct). \qquad \textbf{Eq 3.2}$$

Despite the generality of Eq 3.2 the speed term can be extracted from the function f by differentiating twice with respect to t and x giving

$$\frac{\partial^2 y}{\partial t^2} = c^2 \frac{\partial^2 f(x-ct)}{\partial (x-ct)^2}, \qquad \textbf{Eq 3.3}$$

$$\frac{\partial^2 y}{\partial x^2} = \frac{\partial^2 f(x-ct)}{\partial (x-ct)^2}. \qquad \textbf{Eq 3.4}$$

These can be combined to produce

$$c^2 = \frac{\partial^2 y}{\partial t^2} \Big/ \frac{\partial^2 y}{\partial x^2}. \qquad \textbf{Eq 3.5}$$

This equation is valid for any kind of periodic wave motion and can be used to determine how the speed of sound varies in a material. As Titan's atmosphere is being considered in this work, the speed of sound in a gas will be investigated further. Consider an infinite tube of cross sectional area A, down which a plane wave is transmitted. Molecules at a distance x along the tube from an arbitrary origin are on average displaced by a distance s, which is a function of x-ct, and we can consider this displacement as the periodically changing variable y given in Eq 3.1 to Eq 3.5. At a time, t, the fractional volume change for a given small mass of gas is given by

$$\frac{\partial V}{V} = \frac{\partial s}{\partial x}. \qquad \textbf{Eq 3.6}$$

Therefore, if two points are considered along the tube, a and b, separated by a small distance $\delta x$ then the difference in fractional volume change between gas at the two locations is given by

$$\delta \frac{\partial V}{V} = \frac{\partial^2 s}{\partial x^2} \delta x \qquad \textbf{Eq 3.7}$$

The bulk modulus of a gas is defined as

$$K = -V\frac{\partial P}{\partial V} \qquad \textbf{Eq 3.8}$$

which can then be used to estimate the difference in pressure between a and b.

$$\delta P = \frac{\partial^2 s}{\partial x^2}\delta x K \qquad \textbf{Eq 3.9}$$

The net force on the element of fluid between a and b is $A\delta P$ and the mass of this element is $\delta x A\rho$. Applying Newton's 2nd law of motion to the element and using Eq 3.9 to define $\delta P$ gives

$$A\frac{\partial^2 s}{\partial x^2}\delta x K = \delta x A\rho\frac{\partial^2 s}{\partial t^2} \qquad \textbf{Eq 3.10}$$

This rearranges to

$$K/\rho = \frac{\partial^2 s}{\partial t^2} \Big/ \frac{\partial^2 s}{\partial x^2} \qquad \textbf{Eq 3.11}$$

and then comparison to

$$c^2 = \frac{\partial^2 y}{\partial t^2} \Big/ \frac{\partial^2 y}{\partial x^2}. \qquad \textbf{Eq 3.5}$$

shows that

$$c^2 = K/\rho. \qquad \textbf{Eq 3.12}$$

From Eq 3.12 it is clear that the speed of sound is dependent upon composition as K will vary between different types of gases. However, K is a thermodynamic quantity and will vary depending upon whether the conditions are isothermal or adiabatic. For a sound wave of high frequency the adiabatic approximation is most appropriate. However, at low frequencies this becomes a less good approximation meaning that K, and hence c, will vary with frequency. This property can cause dispersion to occur for broad band signals.

In order to investigate sound speed further, an appropriate equation of state based on either experimental data or theoretical models is required so that the appropriate value of K can be determined. This is considered in the next section.

## §3.2 Ideal Gas Equations of State

The most basic equation of state that can be used is the ideal gas law

$$P = \frac{\rho}{m} RT \qquad \textbf{Eq 3.13}$$

where m is the mean molecular mass and R is the gas constant. P, T and ρ are pressure temperature and density respectively. Under adiabatic conditions it is known that for a fixed number of ideal gas molecules

$$PV^{\gamma} = \text{constant} \qquad \textbf{Eq 3.14}$$

where γ is the ratio of specific heats. This can be differentiated to give

$$\frac{\partial P}{\partial V} = -\frac{\gamma P}{V} \qquad \textbf{Eq 3.15}$$

We can combine Eq 3.8, Eq 3.13 and Eq 3.15 to find that

$$K = \gamma P = \frac{\gamma \rho}{m} RT, \qquad \textbf{Eq 3.16}$$

So from Eq 3.12

$$c = \sqrt{\frac{\gamma RT}{m}}. \qquad \textbf{Eq 3.17}$$

Therefore, it can easily be seen that measurement of temperature and the speed of sound in an ideal gas allows calculation of the ratio γ/m; in a binary mixture we can therefore determine the mole fraction of each constituent. If we assume that in a binary mixture m and γ vary linearly with mixing ratio[2], then Eq 3.17 can be used to investigate how sensitive this composition calculation is to the speed of sound and temperature. For a mixture of nitrogen and methane at temperatures close to those expected in Titan's lower

[2] This is rather crude as γ is not a linear function of mixing ratio. However, it is a useful approximation at this stage.

atmosphere Eq 3.17 indicates that a change of 1 m $s^{-1}$ in the speed of sound would be caused by a change of ~2.5 % in mole fraction of methane. Clearly temperature must also be considered and a change of 1 K in temperature is equivalent to a change of ~2.8 % in mole fraction. These calculations suggest that measurement of the speed of sound has the potential to be a reasonably sensitive probe into the composition of Titan's atmosphere. However, care must be taken in ensuring accurate measurements are taken and that temperature change is not misinterpreted as composition change.

## §3.3 Non-Ideal Equations of State

Eq 3.13 - Eq 3.17 and the calculations in §3.2 have all assumed the ideal gas law; unfortunately on Titan the atmosphere is dense, meaning that interactions between molecules occur, i.e. we cannot assume that gas molecules are infinitely small point masses as in an ideal gas. This causes deviation from the ideal gas law that must be accounted for in our calculations. A number of different equations of state have been investigated for use with the Huygens data and comparison to scarce experimental data has been used to decide which equation of state should be used. A description of each equation of state investigated follows.

### §3.3.1 Modified Benedict-Webb-Rubin Equation of State

The National Institute of Standards and Technology (NIST) is able to provide a number of different programmed implementations of equations of state. Database 14 is such an implementation and can predict the speed of sound in pure substances and mixtures of 17 different components including nitrogen and methane.

For a given pressure and temperature, the database uses a Peng-Robinson equation of state (PREOS) (Peng & Robinson 1976) to determine the stable phase(s). The PREOS is an evolution of the van der Waals equation of state and builds upon earlier modifications (Redlich & Kwong 1949; Soave 1972), all of which have the advantage of having only two

terms. This ensures only two empirical constants are required. The two constants can hence be determined from the fluid's critical properties only. In addition, the computing power required to use these equations of state is minimal. The further advantages of the PREOS over previous work include an improved agreement between measured and predicted vapour pressures for pure substances and an increase in agreement with vapour liquid equilibrium results for mixtures, especially those including paraffins, hydrogen and nitrogen (Han, et al. 1988).

To determine the thermodynamic properties of the respective phases, a modified Benedict-Webb-Rubin equation of state (MBWREOS) (Jacobsen & Stewart 1973) is used. This equation of state essentially describes the pressure as a 32 term polynomial with terms in $\rho^1$-$\rho^{13}$, $T^1$-$T^{-3}$ and $\exp(-\rho^2/\rho_c^2)$ where $\rho_c$ is the critical density of the fluid. These 32 terms were selected from a possible 50 as those with the most significant correlation factors to experimental data. The 32 terms each require an empirical constant determined by least squares fitting to experimental data for each of the seventeen components available in the database (Younglove 1982; Younglove & Ely 1987).

To calculate the properties of mixtures, an extended version of the corresponding states theory is used with the van der Waals mixing rules (Ely 1990). In the corresponding states theory all molecules are assumed to have a spherically symmetric potential with the same functional form. This leads to the conclusion that the pressure at a particular reduced temperature and reduced density is equal for all gases. This can be represented such that for fluids i and j

$$P_i(\rho_i, T_i) = P_j(\rho_j h_{ij}, T_j / f_{ij}), \qquad \textbf{Eq 3.18}$$

where h and f are constants used to map the temperature-pressure-density curve between the two fluids. They are given by the ratios of critical densities and temperatures respectively,

$$h_{ij} = \rho_j^c / \rho_i^c , \qquad \textbf{Eq 3.19}$$

$$f_{ij} = T_i^c / T_j^c , \qquad \textbf{Eq 3.20}$$

where superscript c indicates the critical property. We can then define the pressure of a mixture of n components by

$$P_{mix}(\rho_{mix}, T_{mix}) = P_j(\rho_j h_{mix}, T_j / f_{mix}), \qquad \textbf{Eq 3.21}$$

where $h_{mix}$ and $f_{mix}$ are given by the van der Waals mixing rule as

$$h_{mix} = \sum_{i=1}^{n}\sum_{j=1}^{n} x_i x_j \frac{\left(h_{ij}^{1/3}+1\right)^3}{8}\left(1-l_{ij}\right) \qquad \textbf{Eq 3.22}$$

$$f_{mix}h_{mix} = \sum_{i=1}^{n}\sum_{j=1}^{n} x_i x_j f_{ij}^{1/2}\left(1-k_{ij}\right)\frac{\left(h_{ij}^{1/3}+1\right)^3}{8}\left(1-l_{ij}\right) \qquad \textbf{Eq 3.23}$$

where $x_i$ is the mole fraction of component i and $l_{ij}$ and $k_{ij}$ are empirical interaction parameters determined by experiment and equal to zero when i=j.

The corresponding state model has been extended to include non spherically symmetric molecules by the inclusion of shape factors $\theta(T,\rho)$ and $\varphi(\rho,T)$ such that

$$f_{ij} = \theta_{ij} T_i / T_j , \qquad \textbf{Eq 3.24}$$

$$h_{ij} = \varphi_{ij} \rho_j / \rho_i . \qquad \textbf{Eq 3.25}$$

These factors modify the shape of the pressure-volume-temperature surfaces to improve accuracy but they also add extra complexity. As temperature and density dependence of f and h has been introduced, their derivatives occur in calculations of some thermodynamic properties. This is, however, a necessary complication to improve accuracy. The functions for the shape factors are derived by comparing the MBWREOS for the two components and ensuring that Eq 3.18 is satisfied.

The NIST Database 14 is an implementation of the PREOS and the MBWREOS that takes as inputs the pressure, temperature and composition of a pure fluid or mixture. The density of the fluid is determined iteratively using the MBWREOS and this density is then used to determine further thermodynamic parameters such as heat capacities and the speed of

sound. In the case of mixtures the values of $f_{mix}$ and $h_{mix}$ must also be found iteratively and a separate algorithm is used to determine the density.

Unfortunately, a fundamental problem exists in the database. This manifests itself in the fact that for a mixture of two components, as the mole fraction of one component tends to unity the density calculated by the mixing algorithm does not tend towards the density calculated by the pure fluid algorithm, i.e. there is a discontinuity at the pure fluid limit. This discontinuity is shown in Fig 3.1 for the speed of sound of a mixture of nitrogen and methane at Titan's surface conditions. Although the source of this discontinuity has so far eluded detection, it is clear that it could introduce significant errors in our calculation of composition from sound speed.

**Fig 3.1 Plot showing the discontinuity at the pure nitrogen limit in a nitrogen/methane mixture at approximately Titan's surface conditions – 93.5 K, 0.147 MPa**

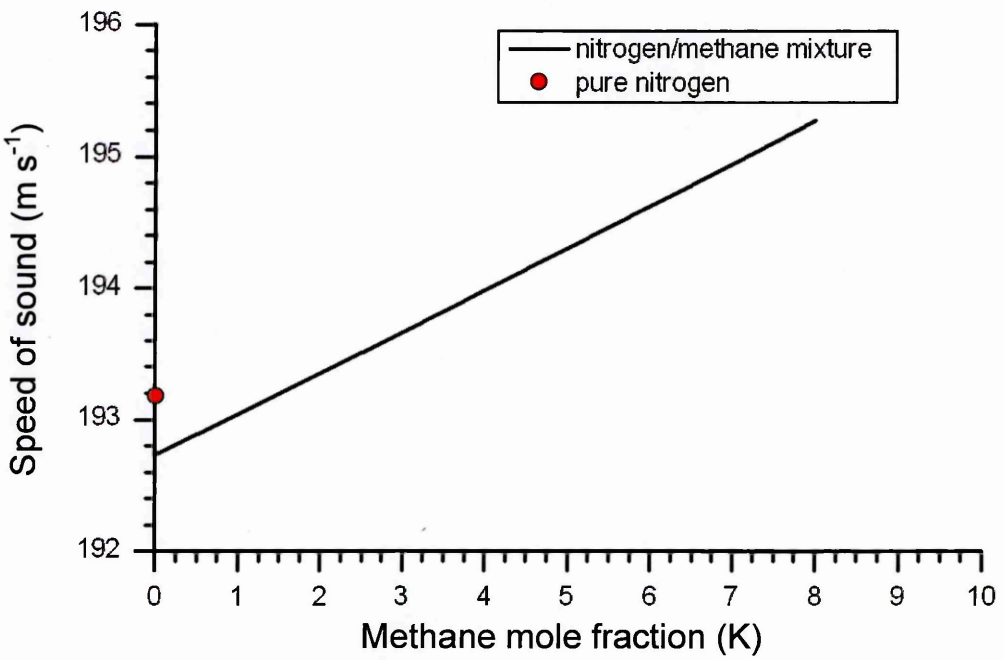

## §3.3.2 Virial Equation of State

The Virial equation of state (VEOS) has been specifically considered for use in Titan's atmosphere in the work of Hagermann & Zarnecki (2006). The VEOS itself is described by

$$\frac{PV_m}{RT} = 1 + \frac{B(T)}{V_m} + \frac{C(T)}{V_m^2} + \ldots \qquad \textbf{Eq 3.26}$$

where $V_m$ is the molar volume, B and C are the second and third virial coefficients and are functions of temperature. The second virial coefficient describes two-molecule interactions, the third describes three-molecule interactions and so on. This means that, given a sufficiently accurate inter-molecular potential, values for the virial coefficients can be calculated directly through statistical mechanics (Reichl 1980). This is in contrast to the MBWREOS where the terms in the equation are chosen through experience and are entirely empirical. Unfortunately, the inter-molecular potentials are generally not known with sufficient accuracy to allow accurate virial coefficients to be calculated so, in practice, they are usually determined by experiment. Because the later virial terms become less important, due to the increasing power of the $1/V_m$ term, the second virial coefficient is often sufficient to make accurate predictions. However, for dense gases, such as Titan's lower atmosphere, the third virial coefficient is required (Hagermann & Zarnecki 2006). Unfortunately high precision values for third virial coefficients are scarce. The situation is particularly poor for low temperatures (especially for older data, e.g. Dymond & Smith (1969) provided C = -13600 ± 90% at 131.93 K).

Despite this problem, treatment of mixtures is relatively simple as a mixing rule can be determined directly from statistical mechanics (see e.g. Feynman (1972)). The virial coefficients, $B_{mix}$ and $C_{mix}$ for a mixture of n components each having mole fractions $x_1$, $x_2,\ldots,x_n$. are given by

$$B_{mix} = \sum_{i=1}^{n}\sum_{j=1}^{n} B_{ij} x_i x_j , \qquad \textbf{Eq 3.27}$$

$$C_{mix} = \sum_{i=1}^{n}\sum_{j=1}^{n}\sum_{k=1}^{n} C_{ijk} x_i x_j x_k , \qquad \textbf{Eq 3.28}$$

where the virial cross coefficients $B_{ij}$, $C_{ijk}$ can, for example, be given by

$$B_{ij} = \frac{B_i + B_j}{2}, \qquad \textbf{Eq 3.29}$$

$$C_{ijk} = \frac{C_i + C_j + C_k}{3}. \qquad \textbf{Eq 3.30}$$

Hence, given appropriate functions for the virial coefficients of each component at the appropriate temperatures, the speed of sound can be determined for gas mixtures through the use of Eq 3.12 and Eq 3.8.

### §3.3.3 Helmholtz Energy Equation of State

The Helmholtz energy, A, is defined by

$$A = U - TS, \qquad \textbf{Eq 3.31}$$

where U is the internal energy and S is the entropy. Because A is a state variable (in a similar manner to pressure, temperature and density), an equation of state can be explicit in A rather than being explicit in P such as in Eq 3.18 or Eq 3.24. From a Helmholtz energy equation of state (HEEOS) all other thermodynamic properties of a fluid can be determined. Setzmann & Wagner (1991) presented this equation of state developed for methane in the form

$$A(\rho, T) = A_0(\rho, T) + A_r(\rho, T), \qquad \textbf{Eq 3.32}$$

where $A_0$ is the ideal gas Helmholtz energy and $A_r$ is residual Helmholtz energy that is the contribution of the intermolecular interactions, i.e. the non-ideal part. In practice the equation is used in a reduced, dimensionless form such that

$$\frac{A(\rho,T)}{RT} = \alpha(\delta,\tau) = \alpha_0(\delta,\tau) + \alpha_r(\delta,\tau), \qquad \textbf{Eq 3.33}$$

where $\delta = \rho/\rho_c$ and $\tau = T_c/T$. The ideal part, $\alpha_0$, is derived directly from thermodynamics, but $\alpha_r$ is determined empirically from experimental data. Setzmann & Wagner initially included 393 polynomial, exponential and Gaussian terms in the function for $\alpha_r$ and a fitting and optimisation algorithm was used to select the most important terms and fit to the experimental data.

A similar equation of state, explicit in the Helmholtz energy, has been generated for nitrogen (Span, et al. 2000) as well as carbon dioxide (Span & Wagner 1996), a number of short chain hydrocarbons (Smukala, et al. 2000; Lemmon & Ihmels 2005; Bucker & Wagner 2006a, b) and some further industrially important fluids (Lemmon & Span 2006). A number of these substances, as well as others, were also considered with a generalised form for $\alpha_r$ for polar and non-polar fluids by Span & Wagner (2003b; 2003a; 2003c).

In order to generalise the HEEOS to mixtures, Lemmon & Jacobsen (1999) developed a method similar to the corresponding states model mentioned in §3.3.1. Here we find that for a mixture of n components

$$\alpha(\delta,\tau,\mathbf{x}) = \sum_{i=1}^{n} x_i[\alpha_{0i}(\rho,T) + \alpha_{ri}(\delta,\tau) + \ln(x_i)] + \Delta\alpha(\delta,\tau,\mathbf{x}). \qquad \textbf{Eq 3.34}$$

$\alpha_{0i}$, $\alpha_{ri}$ and $x_i$ are the ideal Helmholtz energy, the residual Helmholtz energy and the mole fraction, respectively, of the $i^{th}$ component. The natural log term is derived from the entropy contribution to Helmholtz energy and $\Delta\alpha$ is the extra contribution due to mixing. $\delta$ and $\tau$ are now functions of the mole fractions and the critical properties of all components. Lemmon & Jacobsen (1999) presented $\Delta\alpha$ as an empirical function summed over each binary pair within the mixture,

$$\Delta\alpha = \sum_{i=1}^{n-1}\sum_{j=i}^{n} x_i x_j F_{ij} N(\delta,\tau), \qquad \textbf{Eq 3.35}$$

where F is a fitting parameter and N is a fitting function respectively. They have been separated because only F varies with different components whereas the function N is the

same for any fluid at a given $\delta$ and $\tau$ and can be arbitrarily complex. This form, therefore, has the advantage that it is general to all fluids and can be easily fitted to even small datasets for binary mixtures as only the fitting parameter F must be derived. In addition, binary data can be easily extrapolated to provide estimates for mixtures of many components. This is, however, not the only function for $\Delta\alpha$ that has been derived. It is also possible to produce functions for $\Delta\alpha$ that are specific to a mixture of two particular components. A comparison of these two methods can be found in the work of Lemmon & Tillner-Roth (1999).

The HEEOS for many components has been compiled by Kunz et al. (in press) along with a generalisation for mixtures based on Eq 3.34 and the subsequent work described here. The work of Kunz et al. has been adopted by Groupe Européen de Recherches Gazières (GERG) as the standard reference equation of state for natural gases and a numerical library, named GERG-2004, has been produced. GERG-2004 allows properties of fluids and mixtures of fluids to be determined within specified temperature and pressure ranges and the implementation can be used in a similar manner to the NIST database 14 considered in §3.3.1.

## §3.4 Comparison of Equations of State

Three non-ideal models for the speed of sound under Titan-like conditions have been presented and Fig 3.2 shows the predictions for each equation of state under approximate Titan surface conditions. The non-ideal equations of state produce predictions that are broadly similar, but the ideal gas prediction is very different. The agreement, however, is not perfect; the virial and Helmholtz equations almost converge at the pure nitrogen limit as seen by their intercept on the plot. At the pure nitrogen limit the MBWREOS does not agree with the other two equations of state. However, as seen in Fig 3.1 the NIST implementation of the MBWREOS shows a discontinuity in the pure fluid limit. The NIST pure fluid algorithm does agree well with the other non-ideal equations of state for pure

nitrogen. Despite fairly good agreement for pure nitrogen, the predictions for mixtures vary considerably between the equations of state. In addition to the discrepancy between predictions for pure fluids and mixtures of fluids from NIST database 14, the virial and Helmholtz predictions diverge as methane mole fraction increases to 0.09 creating a discrepancy of ~1.4 m $s^{-1}$.

The importance of selecting the most accurate equation of state from those investigated can be highlighted by considering the methane abundance predicted by each model for a particular speed of sound measurement. For the conditions represented in Fig 3.1, i.e. temperature of 93.5 K and pressure of 0.147 MPa, a speed of sound measurement of 194 m $s^{-1}$ would result in predicted methane mole fractions as follows:

- Ideal gas – no valid solution
- MBWREOS – 0.041
- Virial equation of state – 0.066
- Helmholtz equation of state – 0.027

It can therefore be clearly seen that a discrepancy of almost 0.04 exists between the minimum and maximum predicted values.

**Fig 3.2 Plot showing variation in predicted sound speed with methane mole fraction for the discussed equations of state at approximately Titan's surface conditions of 93.5 K and 0.147 MPa.**

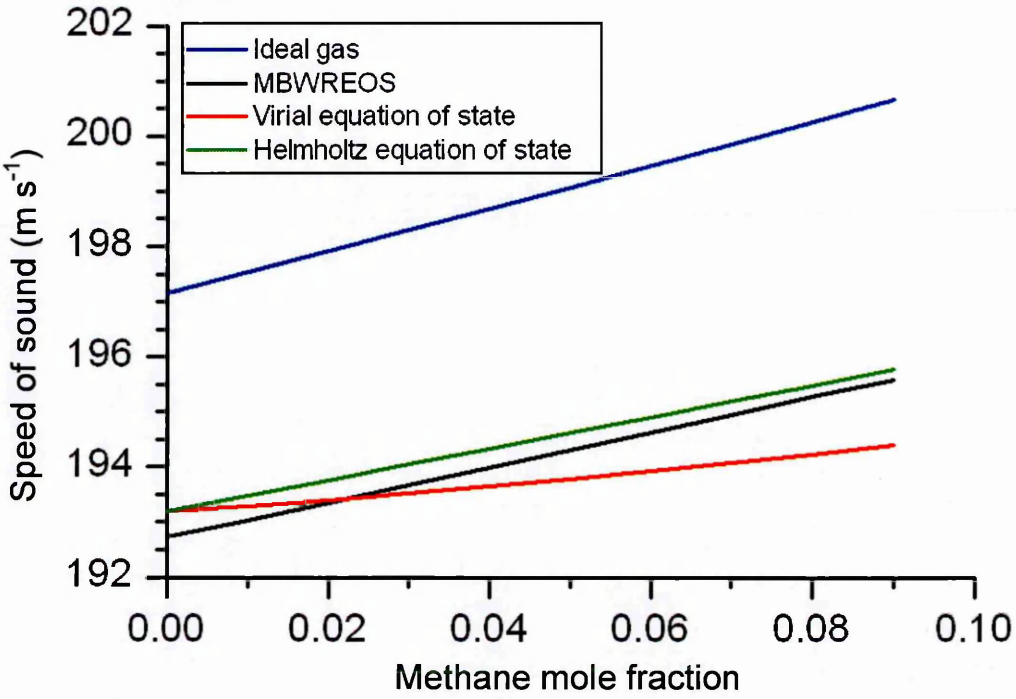


In order to decide effectively which equation of state should be used, comparison with experimental data is essential. Unfortunately, to the knowledge of the author, speed of sound data under Titan-like conditions do not exist. However, data do exist for mixtures of methane and nitrogen down to 170 K (Estela-Uribe, et al. 2006) and these data have been used to assess the accuracy of the equations of state. These measurements were performed for methane mole fractions of 0.89999, 0.80001 and 0.4578 using a high accuracy resonance method. The stated uncertainties were ±0.0 2% except for the highest pressure measurements with the methane mole fractions of 0.4578. Here the expected uncertainty was not more than 0.06 %. High accuracy pure nitrogen data has also been considered (Estela-Uribe & Trusler 2000). As Titan's atmosphere is expected to contain only a few percent methane, the nitrogen data is closer to the expected composition than the mixture data. The equations of state were compared to the experimental data and the fractional residuals have been plotted in Fig 3.3 through Fig 3.6. The fractional residual was calculated as the difference between the experimental data and the equation of state

prediction divided by the experimental data. Clearly the closer this value is to zero the better the equation of state fits the data.

**Fig 3.3 Comparison between non-ideal equations of state and experimental data for pure nitrogen**

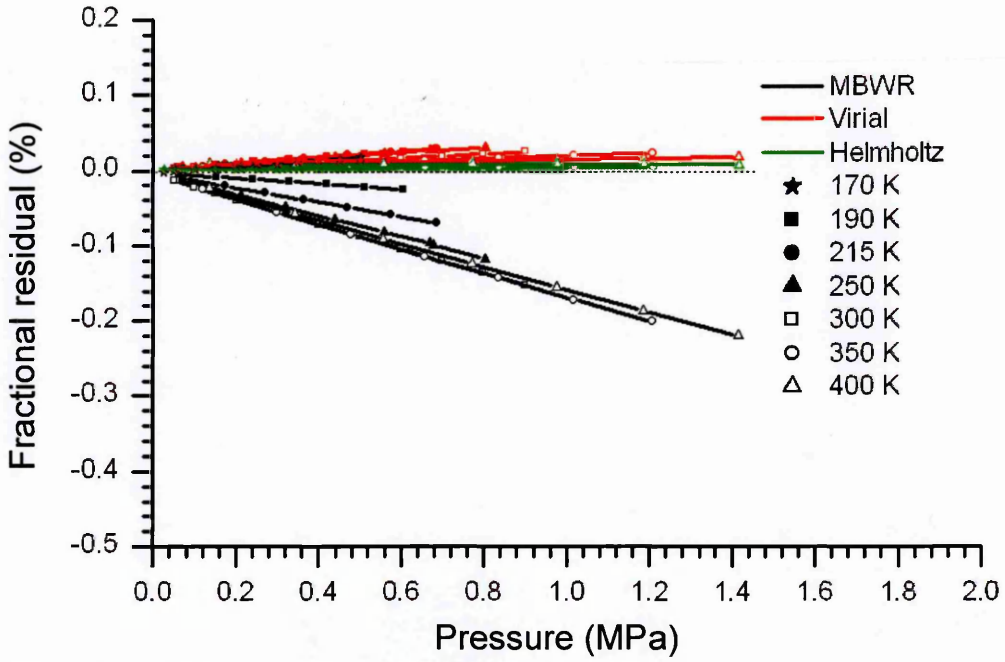


**Fig 3.4 Comparison between non-ideal equations of state and experimental data for nitrogen and methane mixtures with a methane mole fraction of 0.4578**

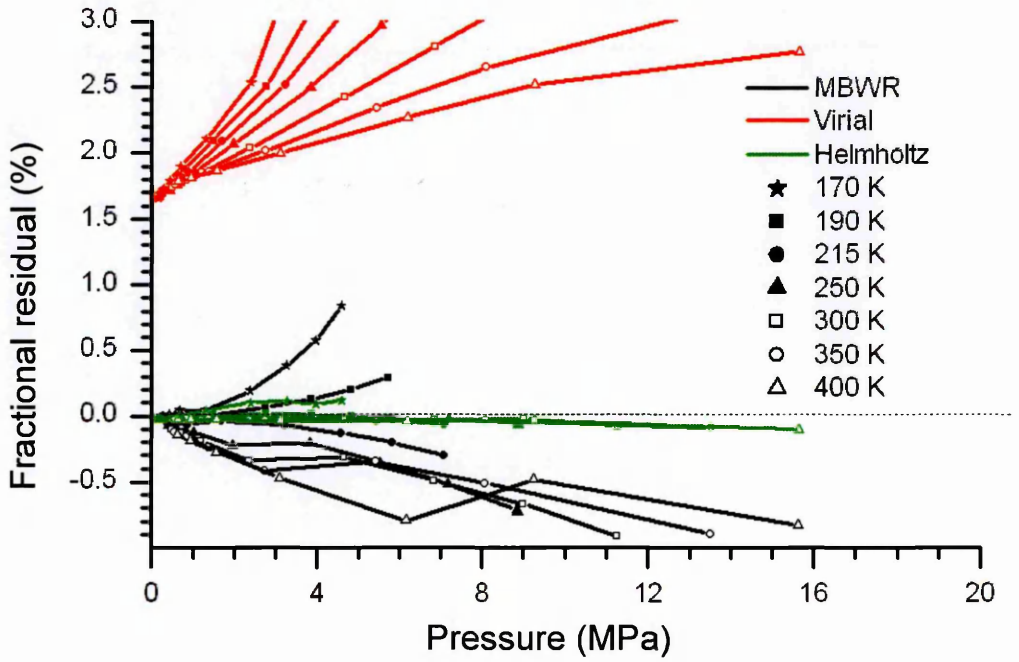

**Fig 3.5 Comparison between non-ideal equations of state and experimental data for nitrogen and methane mixtures with a methane mole fraction of 0.80001**

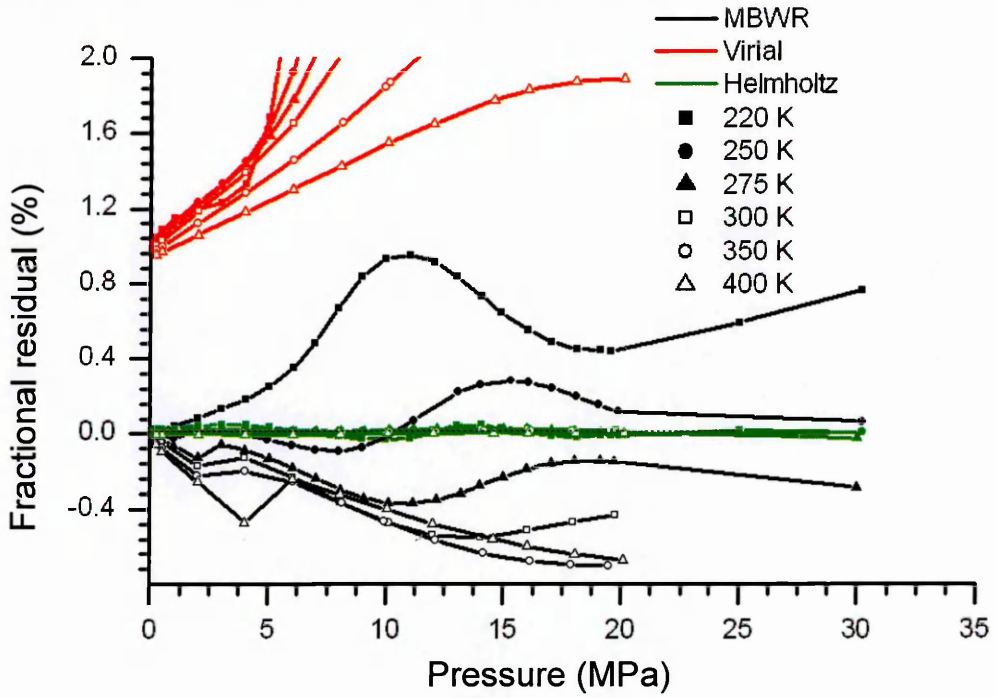


**Fig 3.6 Comparison between non-ideal equations of state and experimental data for nitrogen and methane mixtures with a methane mole fraction of 0.89999**

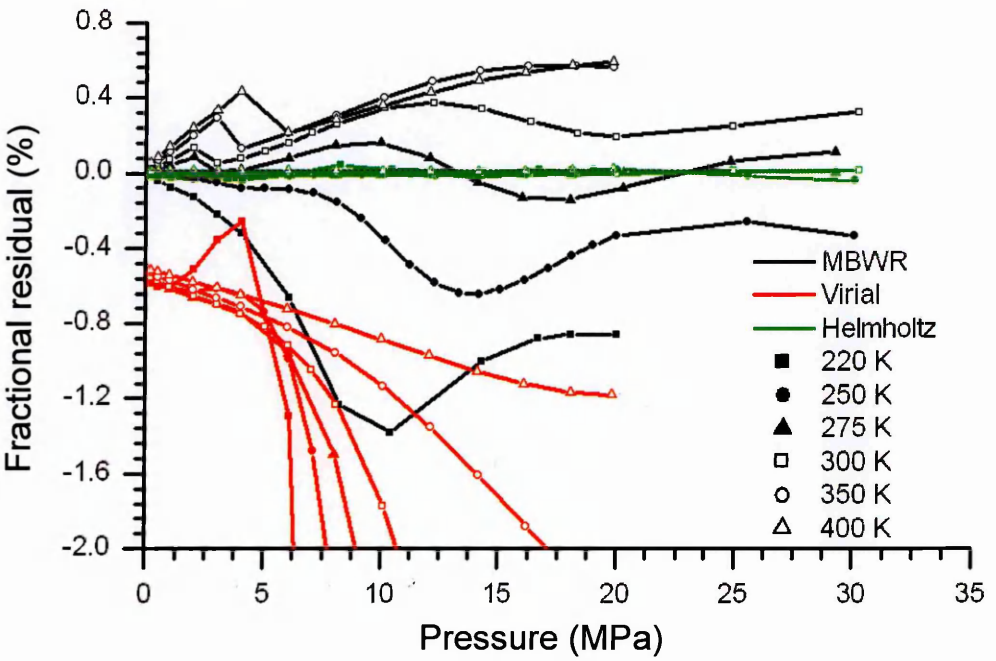


The plots in Fig 3.3 to Fig 3.6 indicate clearly that the Helmholtz equation of state implemented as GERG-2004 has the residuals closest to zero and most closely fits the experimental data used, with the maximum residual being 0.11 %. This matches well with

the claimed uncertainty of ± 0.1 % in the temperature range 250 – 450 K (Kunz, et al. in press).

The virial equation of state performs well for pure nitrogen at pressures up to around 0.15 MPa. However, for mixtures, this equation of state does not perform well. This is perhaps either due to the mixing rules used or due to the methane virial constants used. It is worth noting that although for pure nitrogen the virial and Helmholtz equations of state match well, this is not the case for pure methane. The accuracy of the virial equation of state also decreases with increasing pressure. This is perhaps to be expected because as pressure increases, four or even five molecule interactions are likely to become important possibly leading to further virial coefficients being required.

In considering the MBWREOS as supplied in the NIST database 14, the mixture algorithm has been used even in the case of pure nitrogen. As described in §3.3.1 there is a problem with the implementation of this equation of state, such that as the concentration of one component in a mixture approaches unity, the pure fluid properties are not reached. The pure fluid algorithm for nitrogen may perform better than shown in Fig 3.3, however, as only the mixture algorithm would be used when determining the composition of Titan's atmosphere, only this algorithm is considered here. For the mixtures used in this investigation the MBWREOS almost always performs better than the virial equation of state, although it is clear that even for the lower pressure data it does not perform as well as the GERG-2004 implementation of the Helmholtz equation of state.

Based on this analysis, the GERG-2004 implementation of the Helmholtz equation of state has been chosen for use in determining methane abundance in Titan's atmosphere. However, this decision has been made knowing that there is currently no data available to test this equation of state for mixtures with methane mole fraction <0.1 at the very low temperatures found near the surface of Titan. There is, therefore, a possibility that under these conditions the accuracy may not be as high as that found by comparison with higher temperature data.

# Chapter 4
# Analysis of Huygens Data

During descent, all of the SSP instruments, including API-V, worked as planned; the descent sequence began at a time $t_0$ which corresponded to UTC of 09:10:21 on the 14th January 2005 (Lebreton, et al. 2005) with API-V beginning to taking measurements at a time of 600 seconds after $t_0$ at an altitude of ~120 km. The entire dataset is shown in its raw uncalibrated form in Fig 4.1. The most obvious features in Fig 4.1 are the two stripes of data above 750 μs, a second stripe at 50-80 μs and an intermediate group of data points in the range of around 650 to 720 μs. The stripes above 750 μs are timeout values recorded when the transmitted signal is not strong enough to trigger the clock to stop as described in §2.2. The stripe at 50 μs is caused by noise, from the transmit pulse, falsely triggering the clock. In order to avoid crosstalk between the transmitting and receiving sensors triggering the clock immediately, a 50 μs blanking period was used, i.e. the clock cannot stop in the first 50 μs. However, ringing on the transmitting sensor sometimes continued beyond 50 μs and in this case crosstalk between the electronics caused false triggering. This ringing was more common when the atmosphere was thin and the damping was less. Hence, it occurred mostly in the upper atmosphere.

The intermediate band of data is almost entirely the useful API-V data. However, there are a few further data points, that can be seen on Fig 4.1, which can be excluded from the analysis as it is not believed that they represent true API-V measurements. For example, there are a number of data points at 614.25 μs which only occur when SSP changes measurement mode and are likely to be caused by software or hardware limitations. There are also some measurements at 512 μs which are only measured in one direction and happen to coincide with the binary value 100000000000 in Huygens internal units. These data points are all deemed to be unreliable and are excluded from the analysis.

**Fig 4.1 Entire API-V dataset collected during the Huygens mission in raw uncalibrated format.**

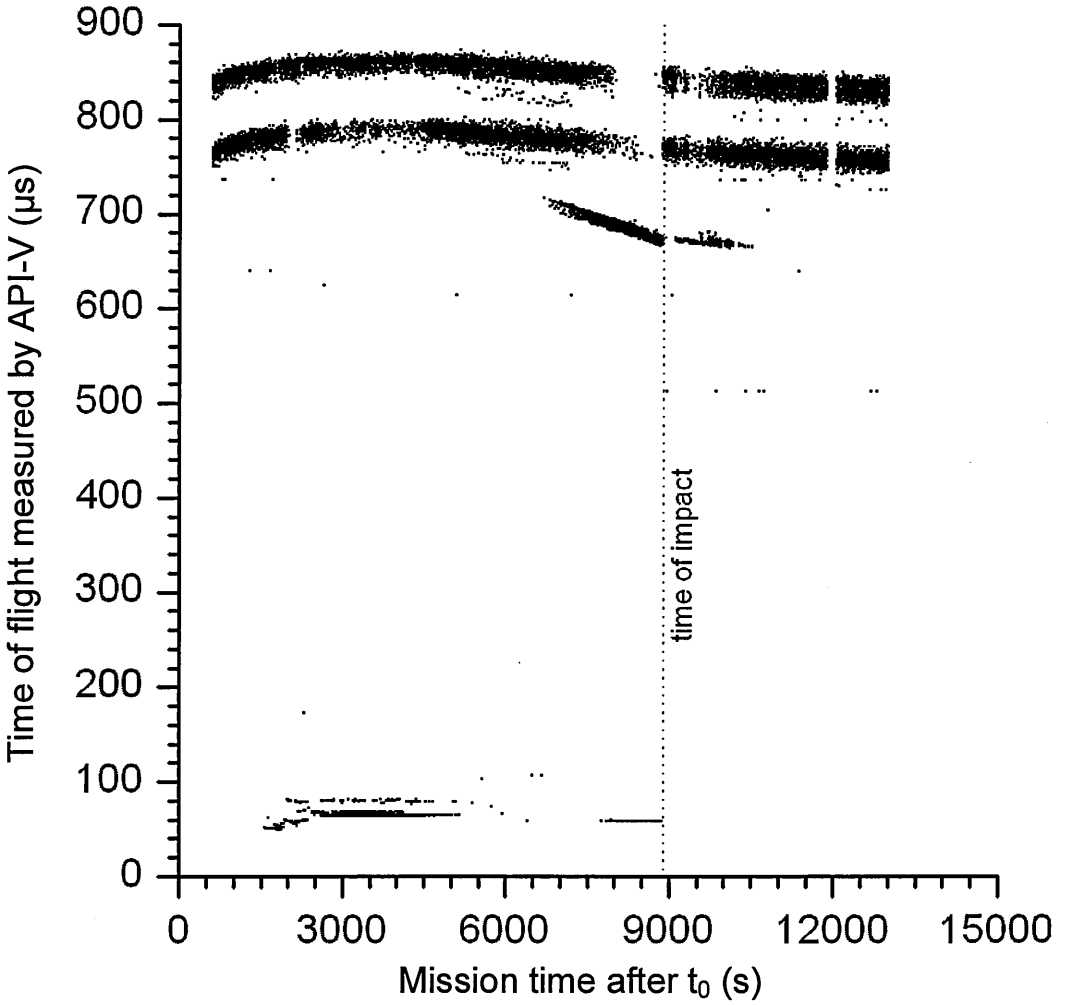


The useful API-V data has been extracted and calibrated by subtraction of the 3.71 μs offset described in §2.2.4 and are shown in Fig 4.2. We can see that the first successful measurement was made at a time of $t_0$ + 6685 s which corresponds to an altitude of approximately 11.1 km or a pressure of around 81.9 kPa. The time of flight decreased as the probe descended. This is as would be expected, as the temperature was also increasing during the descent in this altitude range, increasing the speed of sound. The probe impacted the surface at a time of $t_0$ + 8869.7598 s (Zarnecki, et al. 2005) and the sensors stopped functioning for a short period. Once good data collection resumed, the time of flight continued decreasing, although at a much slower rate compared to that during descent. It is also very noticeable from Fig 4.2 that the spread of data during descent is much higher

than the initial data after impact. The final successful measurement was made at time $t_0$ + 10517 s, 1647 s after landing, although timeout readings continued to be recorded until the data link to Cassini was lost at 13,009 s after $t_0$.

**Fig 4.2 Useful, calibrated API-V data collected during the Huygens descent and after landing.**

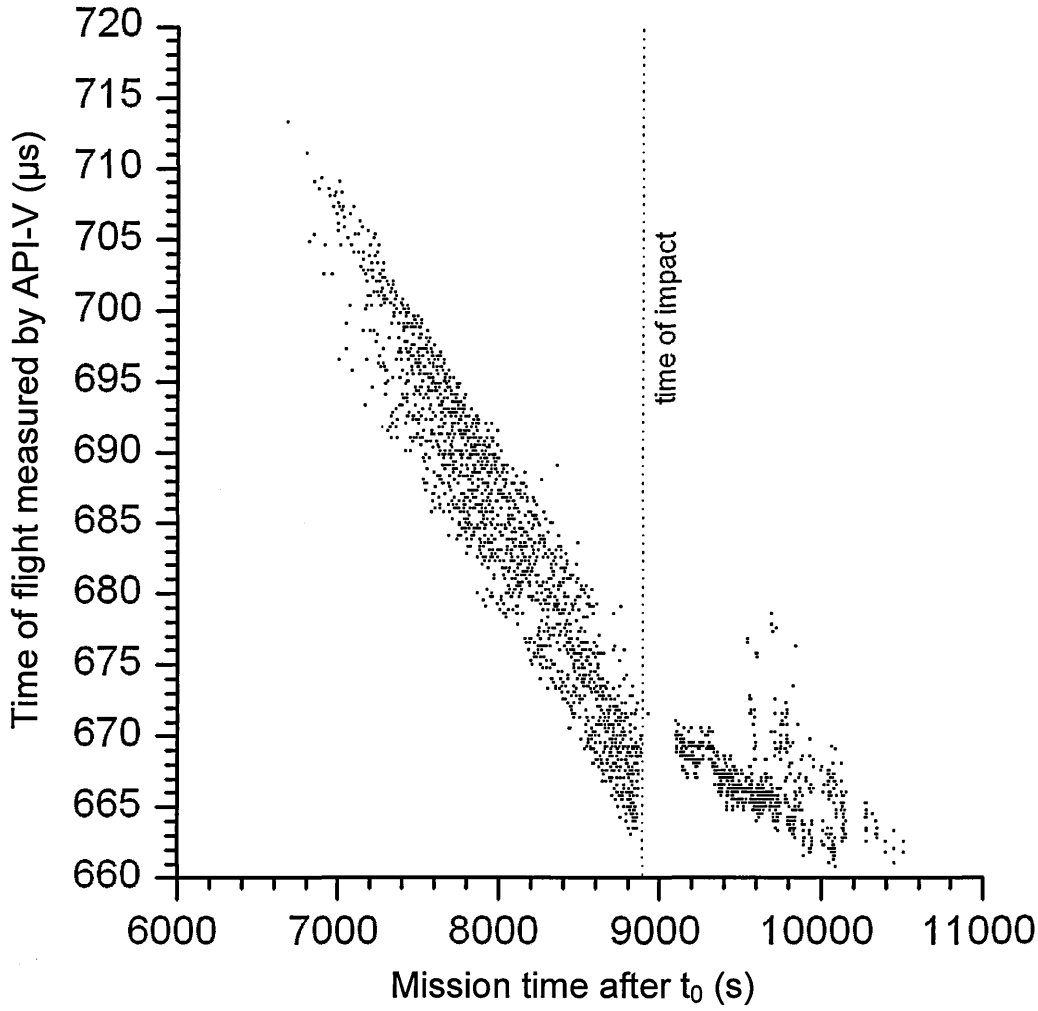


## §4.1 Atmospheric Data

Before discussing the measurements made during descent it is important to first consider the temperature environment of the sensors. Temperature has two significant effects on the measurements. To determine the speed of sound from the time of flight measurements, the separation of the sensor heads must be known. As the temperature varied this separation varied as discussed in 0. Also, any calculation deriving composition from the speed of

sound is very sensitive to temperature as discussed in Chapter 3. For both these purposes the temperature used was that measured by the HASI TEM temperature sensor. HASI measured the external atmospheric temperature with a claimed accuracy of 0.25 K (Ruffino, et al. 1996; Fulchignoni, et al. 2005). This external temperature was considered the most appropriate to use for calculating the thermal contraction of the API-V mountings as they are directly exposed to the atmosphere and thermally insulated from the warm internal structure of the probe. Using other temperature measurements from other sensors makes a negligible difference to the separation. It was also decided that the HASI measurements would be best for use in composition calculations as the API-V sensors are mounted at the opening of the Top Hat on the very front of the probe, with atmospheric gas flowing past. Other temperature sensors are located within the Top Hat, although all are positioned further within the cavity, where heating from thermal leaks and heat generated by other sensors affect the thermal conditions.

### §4.1.1 Measurement Scatter

The descent data, as shown in Fig 4.2, has a spread of around 13 μs. In laboratory tests of the sensors a much smaller spread of around 1-2 μs was seen both using the flight spare sensors and the flight models (Garry 1996). It is also much larger than the spread seen after impact. This would indicate that the increased spread was caused by the air flow during descent. In order to understand further the cause and implications of this spread, its functional form has been examined in some detail. This is important, since, if the scatter has a Gaussian functional form this may have different implications for the analysis and interpretation of the data compared to any other functional form. Visual inspection of Fig 4.2 reveals that, close to the surface, the distribution has a sharp boundary towards lower times of flight, tailing off towards higher values. At higher altitudes the reverse appears to be true.

Unfortunately, however, further investigation is complicated by the changing nature of the property being measured. A histogram of the measured times of flight would be dominated by the change with altitude rather than the scatter, so to understand the scatter the trend in the data must first be removed. This has been attempted by comparison to a reference atmosphere.

For each measurement, an expected value for the time of flight was calculated using the temperature and pressure from HASI and the GERG-2004 equation of state discussed in §3.3.3. For the composition of the reference atmosphere, the value of 4.9 % methane with the remainder nitrogen was used. This is as measured at Titan's surface by the Huygens GCMS (Niemann, et al. 2005). Using this constant value for methane abundance with altitude allows the temperature dependence to be removed yet any changes in methane abundance with altitude will remain.

For each measurement, the difference compared to a prediction based on the reference atmosphere was calculated and a histogram was produce using 0.25 μs bins. The results are shown in Fig 4.3. It is immediately clear that Fig 4.3 does not represent a normal distribution. The histogram does not rise to a single central peak as may be expected by a Gaussian distribution and there is a significant dip in the distribution at 10.5 μs. In addition, rather than being smooth, the distribution contains multiple small peaks. It would be easy to dismiss these as noise; however, they tend to occur with a regular spacing of around 1 μs. This is most obvious in the 8-14 μs range. To check if this is a genuine periodicity a Fourier transform of the histogram has been performed and is shown in Fig 4.4. A clear peak with a frequency of 1 MHz, corresponding to a period of 1 μs, can be seen.

**Fig 4.3 Histogram of the difference between measured and expected values of time of flight.**

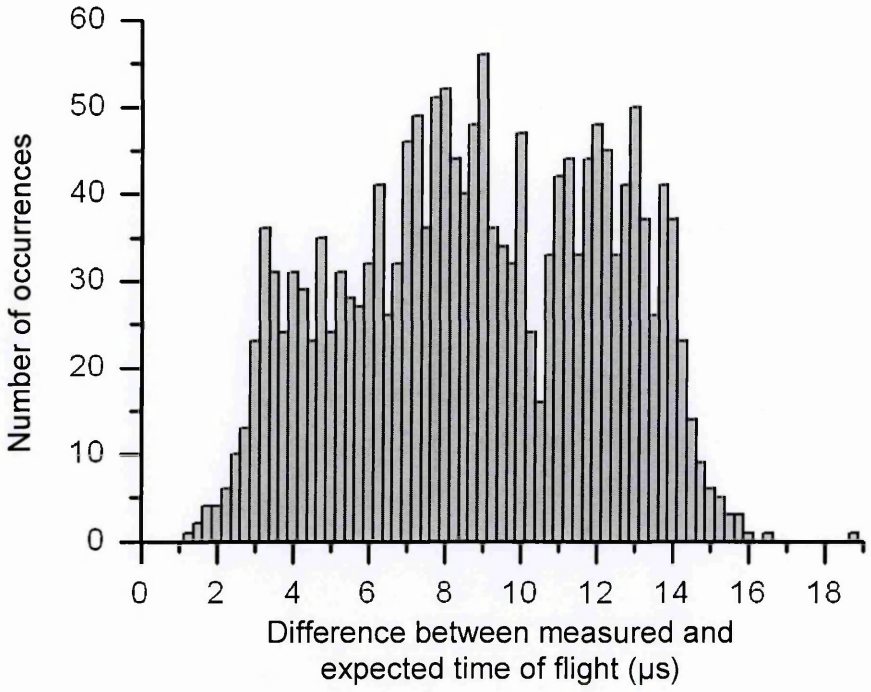


**Fig 4.4 Fourier transform of Fig 4.3. The power axis has been left without a scale because only relative values are of significance.**

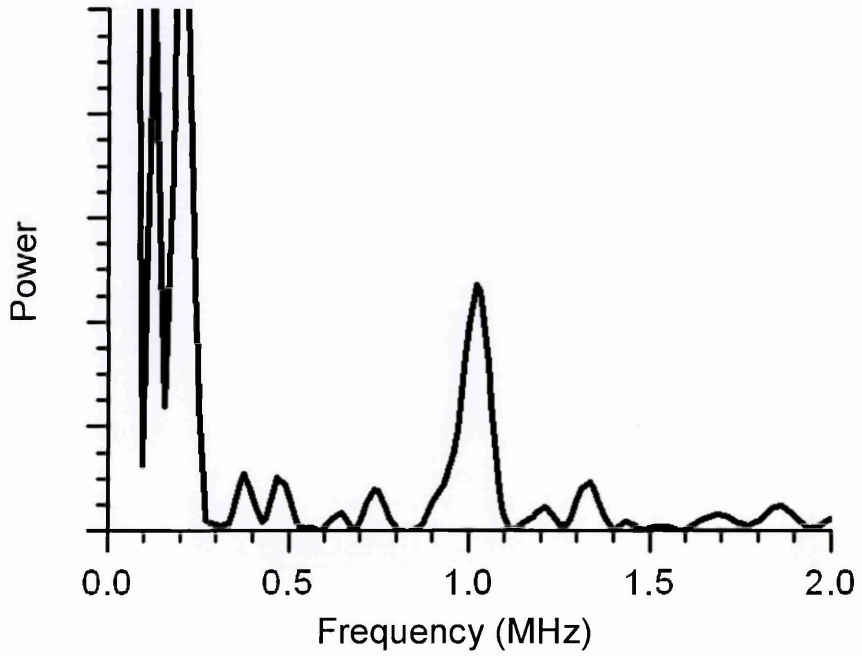


Having determined that the scatter in the API-V data is not Gaussian, but shows a number of 'stripes' with a separation of around 1 μs, the cause must now be discussed. The separation of the stripes is, of course, equal to the period of the sound wave transmitted by

API-V and the total spread of the scatter is slightly longer than the nominal wave train duration (~13 μs compared to 10 μs). However, as some ringing of the sensors occurred this is a good match. This approximate matching of the spread of the data to the transmitted signal and the separation of peaks in the data to the period of the signal indicates that the properties of the wave train are directly related to the spread. The spread could be explained if the clock has triggered on different peaks in the wave train for each measurement in a random or semi-random manner. This is different to the prediction made in Chapter 2, that, as the signal strengthens during the descent, the trigger point would move to earlier peaks on the wave train.

The interpretation that the clock can be stopped on almost any peak in the wave train means that the lower values for time of flight at a particular altitude are closest to the correct value. However, the probability of stopping the clock on each of the peaks may not be identical and is likely to vary with altitude. Hence it is possible that either no measurements triggered on the first peak or that this happened only at low altitudes where the atmosphere is most dense and transmission is most efficient.

The cause of triggering on different peaks is unknown. However, as the scatter reduces after impact, a likely candidate hypothesis is that it was caused by atmospheric gas passing between the sensors. One possible mechanism is that something that could scatter sound waves moved past the sensors in a random or chaotic fashion changing the strength of the signal. These scatterers could be particulates or raindrops, or perhaps turbulent eddies created as gas passed through the electromagnetic shield into the Top Hat. Unfortunately, it has not been possible to thoroughly test any of these hypotheses in the lab. Turbulence occurs when the Reynolds number for a flow exceeds a specified value and as Reynolds number increases with decreasing temperature and increasing pressure we would expect its value to be ~15 times greater on Titan than under standard conditions on Earth. This makes turbulent effects difficult to study. In addition, little is known about the existence or

characteristics of any raindrops in the atmosphere rendering it difficult to specify how likely they are to affect the measurements.

### §4.1.2 Analysis techniques

The hypothesis that the scatter is caused by triggering on the different peaks of the wave train complicates the analysis of the Huygens data somewhat. The usual method of fitting a least squares trend line by minimising the summed, squared residuals cannot be used. Such a method would overestimate the time of flight because each point is systematically too high by an amount varying from perhaps 0 to ~13 μs. In addition, as conditions changed during descent, the probability of triggering on different peaks may have altered, meaning that even the relative change in time of flight produced by a least squares fit cannot be expected to be useful. In a bid to overcome these challenges, other techniques have been employed in order to attempt to either fit an appropriate trend line to the data, or extract a useful dataset from the raw data that better represents the actual speed of sound in the atmosphere.

#### §4.1.2.1 Upper Limit

Triggering on different peaks can only increase the measured time of flight, meaning that each point can be considered as an upper limit. Therefore, the lower edge of the data set provides the strictest limits and represents the closest estimate of the true time of flight. Although simply inspecting Fig 4.2 by eye allows one to estimate where the lower edge of the data lies, this then becomes a matter of judgement. To improve reproducibility, a subset of the data has been selected to represent the lower edge of the data in the following manner. The first N adjacent points were extracted and the lowest point within this sample was kept and the rest discarded. In the case of a tie all the tied points were kept. By rolling this sample along the dataset, the data points which represent the strictest limits were selected. The sample size, N, is clearly critical in balancing smoothing against resolution. If it is assumed that the clock can trigger on any one of 13 peaks and that the probability of

triggering on each peak is equal, then to give a 99 % probability that at least one measurement triggered on the first peak would require 58 successful measurements. A 99.9 % probability would require 87 measurements and a 99.99 % probability would require 116 measurements. Based on these figures a sample size of 100 data points was selected. The results of this process are shown in Fig 4.5.

**Fig 4.5 Plot showing the API-V data against height. The data points selected as the lowest in a rolling sample of 100 are shown in bold.**

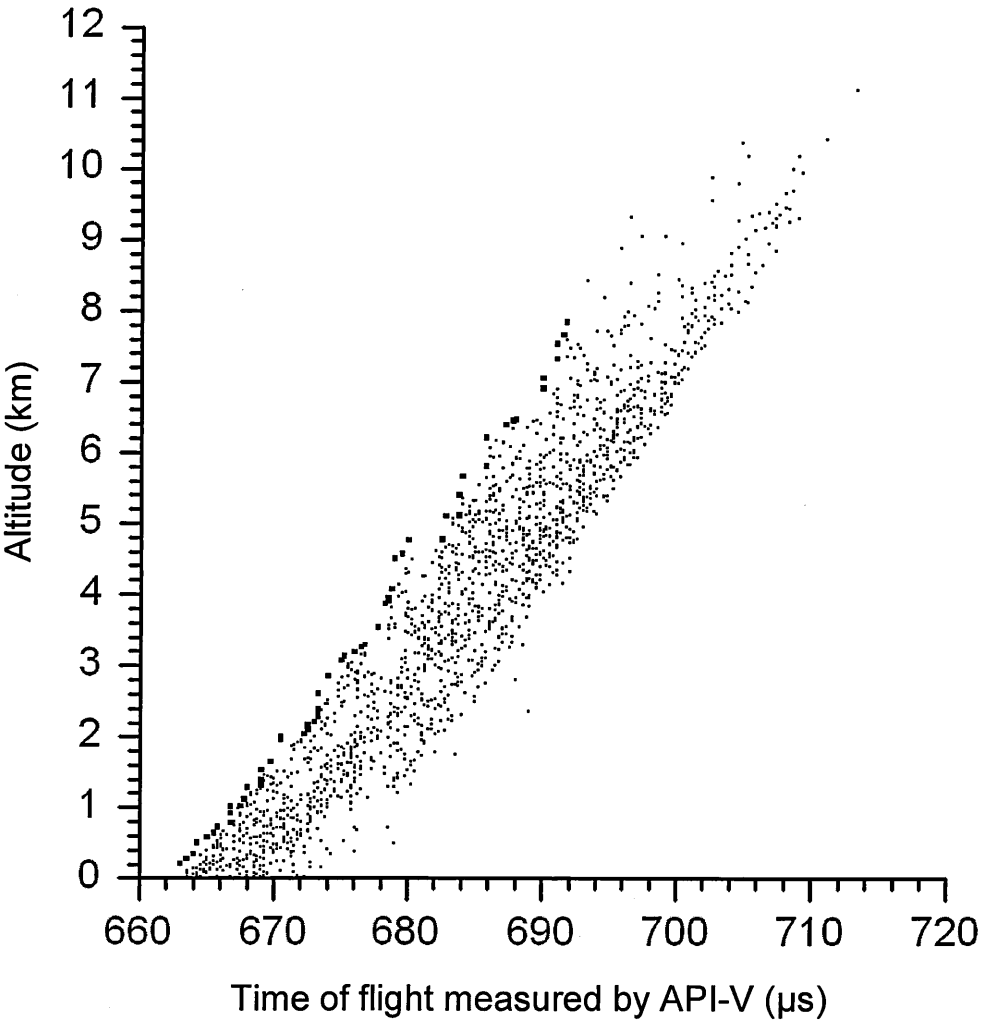


This method's major weakness is the loss of much of the detail. The speed of sound over the entire altitude range is defined by only 58 data points which provide the limits, whilst the other 1686 points (over 96 % of the dataset) have been discarded. The discarded points indirectly contribute to the profile; however, there is information in this data that has been

discarded. Fig 4.3 and Fig 4.4 show that there are stripes in the data which could be exploited to produce an improved trend.

#### §4.1.2.2 Numerical Optimisation

Another way to consider each API-V measurement is as the true time of flight, plus an integral number of periods of the sound wave representing triggering on different peaks of the wave train, plus a small uncertainty. If the peak, which triggered the clock for each measurement, were known then the appropriate integer number of microseconds could be subtracted.

Unfortunately, it is not possible to know this value for certain for any of the Huygens data points; however, if we assume that the speed of sound varies smoothly then if two sequential data points differ by, for example, 8 microseconds, it would seem likely that one measurement triggered 8 peaks later than the other and 8 microseconds could be justifiably subtracted from the time of flight of the larger measurement. If these two points were then 2 μs larger than the next adjacent point then they could be adjusted again and so on. This can be formalised by considering an optimisation parameter, such as the sum of the squares of the differences between subsequent points. Different integer number of periods could then be subtracted from each of the measurements and a value for the optimisation parameter calculated. The process could then be repeated with the data adjusted by different amounts and a new value for the optimisation parameter calculated. This process could be repeated again until a value for the optimization parameter is reached which is considered to be 'good enough' at which point the adjusted data is accepted as an estimate of the 'true' time of flight.

Formally, if we consider an array, $\mathbf{D}_{\mathbf{measured}}$, containing the API-V data and another array of the same size, **N**, containing a set of integers, then if the period of the wave train is T, an optimised version of the API-V data can be defined as

$$\mathbf{D}_{\text{optimised}} = \mathbf{D}_{\text{measured}} - \mathrm{TN}. \qquad \textbf{Eq 4.1}$$

The optimisation parameter, O, can then be defined as

$$O = \sum_{a=1}^{n-1} \left( D_{\text{optimised},a} - D_{\text{optimised},a+1} \right)^2. \qquad \textbf{Eq 4.2}$$

This optimisation parameter is defined only by the relative values of the data, not their absolute values. Hence, once the optimisation is complete, only the relative values for the data are meaningful. To find the absolute values for the data an integral value must be added to **N** such that at least one element of **N** is equal to zero and no elements of **N** are negative. This value will simply be the lowest value element of **N** multiplied by -1.

The basic optimisation strategy which can then be followed is shown in Fig 4.6.

**Fig 4.6 Graphical representation of the basic structure of an optimisation algorithm that could be used for the API-V data.**

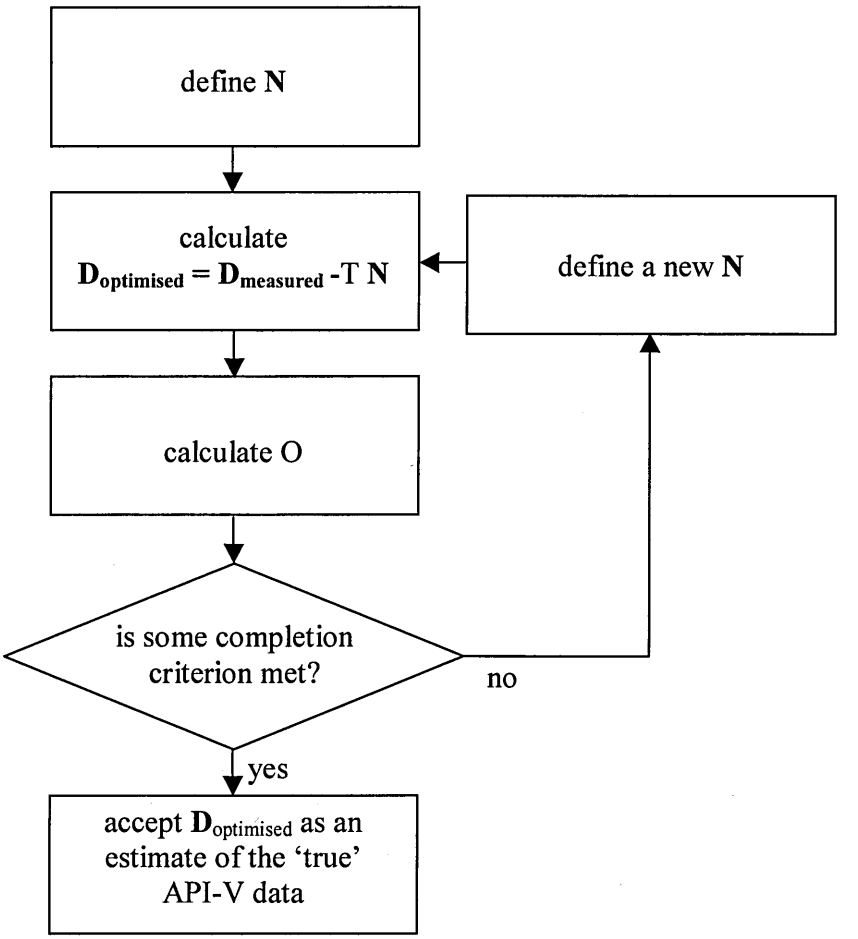


The detail of this method is determined by exactly how the new **N** is defined and by the completion criterion used. Ideally every possible configuration of **N** would be tested; however, if we consider that the data has a spread of ~13 μs so there are perhaps 13

different values for each element of **N** and that **N** has 1744 elements, then this means there are $13^{1744}$ possibilities. Even if an algorithm could test a million possibilities per second then to test all possibilities would take $10^{1919}$ times the age of the universe! Instead, a method must be determined that allows this vast solution space to be searched effectively. One of the simplest methods would be simply to try random implementations of **N** and, after a specified number of random guesses, accept the implementation with the lowest value of O. This is known as a random search. Although easy to implement, the random search is not a very efficient method for optimisation. As there is no way to improve upon good solutions, finding the best solution could take very large amounts of time.

Another strategy could be to start with every element of **N** equal to zero and incrementally increase each element by 1 in a random order. If the adjustment reduces O then it is accepted and if it increases O then it is rejected and the previous solution is maintained. This could be continued until there are no more incremental adjustments that can be made to reduce O. This method will be referred to in this work as an incremental search. Unfortunately, this method suffers from a tendency to become trapped in a local minimum and only a small fraction of the solution space is searched meaning this method is unlikely to reach the global minimum.

A number of algorithms have been developed to avoid this problem of becoming trapped in local minima. The one that was examined for this work is known as simulated annealing.

Simulated annealing takes its inspiration from the science of annealing metal. It is similar to the incremental search described above; however, in this method, even if O increases when an element of **N** is altered there is a finite probability that the new solution is accepted. This probability is related to a simulated temperature and the process is somewhat analogous to atoms moving in a metal during an annealing process. Specifically, the metal is heated so that atoms can move to higher energy states in the hope that as the metal cools the final energy state will be lower than the initial energy state. The same is true in the simulated annealing case. O is allowed to occasionally increase in the hope that

a lower energy state can eventually be found. The probability that an atom will move into a higher energy state is defined by Boltzmann statistics and is proportional to the exponent of the negative of the energy change divided by the temperature. In the optimisation strategy the parameter O is equivalent to energy and we can define a simulated temperature that starts high and decreases throughout the analysis. In fact, the incremental search discussed earlier, is equivalent to simulated annealing with a temperature of zero (perhaps a more appropriate term would be simulated quenching).

The algorithm begins with an initial guess for **N** as all zeros. Each element of **N** is then selected in a random order and the value of the element is increased or decreased by 1, again the direction is chosen at random. The change in O is calculated and if O has decreased then the change is accepted. If O has increased then the probability of the change being accepted is given by

$$P = \exp(-\Delta O / T_{sim}) \qquad \textbf{Eq 4.3}$$

where $\Delta O$ is the change in O and $T_{sim}$ is the simulated temperature. This means that for large increases in O the probability of accepting the change is small unless $T_{sim}$ is also high. When all elements have been selected the temperature is reduced by a factor, $\alpha$, and the process is repeated. This continues until the solution is fully annealed - deemed to have occurred when the temperature is so low that no changes in O occur for 10,000 iterations.

Initial testing on trial datasets indicated that this method could not reliably find an appropriate solution for the atmospheric data. This occurred because the separation of the stripes in the data was not large compared to the width of each stripe. Hence, the solution would tend to switch between the stripes.

#### §4.1.2.3 Bayesian Analysis

Bayesian analysis relies on determining the probability that a particular hypothesis is true by testing it against real life experiments. As an example, consider a 6 sided die which may, or may not, be fair. The only method for testing the fairness of the die would be to

roll it multiple times. However, at what point does one decide that a die is unfair rather than an unlikely distribution of values has been rolled by chance? Bayesian analysis allows calculation of the probability that a hypothesis is true given a set of data. To do this the situation is considered in reverse, i.e. the hypothesis is assumed to be true and the probability of getting the dataset is calculated. Bayesian analysis relates the probability of arriving at a dataset assuming a hypothesis is true to the probability that the hypothesis is true. Returning to the above example, it may be hypothesised that the probability of rolling a 1 on the die is 1/6. Given a set of data from the die, Bayesian analysis can be used to estimate the probability that this hypothesis is correct. The power of Bayesian analysis is that this process could be repeated with a range of hypotheses from 0-1 to consider dice with varying degrees of bias. This allows one to find the most likely probability of rolling a 1 and, in addition, by examining how quickly the probability falls towards zero around this value, an uncertainty can be estimated.

An excellent introduction to Bayesian analysis is given in Sivia (1996), but to summarise here, formally, the Bayes' theorem states that the probability that a hypothesis is true, given a data set and relevant background knowledge, is given by

$$\text{prob}(\text{hypothesis}|\text{data},\text{I}) \propto \text{prob}(\text{data}|\text{hypothesis},\text{I}) \times \text{prob}(\text{hypothesis}|\text{I}). \qquad \textbf{Eq 4.4}$$

Here I represents the relevant background knowledge, the vertical bar represents 'given that' and the comma represents the logical 'and.' The terms in turn from left to right are referred to as the posterior, the likelihood function and the prior. If it is assumed that there is no background knowledge then the prior becomes equal to unity and

$$\text{prob}(\text{hypothesis}|\text{data}) \propto \text{prob}(\text{data}|\text{hypothesis}) \qquad \textbf{Eq 4.5}$$

Eq 4.4 shows that if the probability of arriving at a dataset, given that the hypothesis is true, can be calculated, then this can be used to determine the probability that the hypothesis is true given that particular dataset. In the case of the API-V data the hypothesis is that 'the true time of flight is equal to a value $t_{hypothesis}$.' Bayesian analysis allows subset

of the Huygens data to be used to determine the probability of the hypothesis being true for different values of $t_{hypothesis}$. Hopefully, a plot of probability vs. $t_{hypothesis}$ would reveal a peak and the most probable value of t could be accepted as true with the uncertainty being represented by the width of the peak. However, this method presents a similar problem to that seen when plotting the histogram in §4.1.1. The larger the subset of data used the sharper the peak can become, however, the temperature and pressure change with altitude so the true time of flight also changes between each measurement. This has the effect of widening the peak. To help to reduce this effect the same remedial technique is employed. The dataset is compared to a prediction of the time of flight based on a reference atmosphere to produce a time of flight difference $\Delta t_{data}$ for each data point. The hypothesis now becomes 'the true time-of-flight-difference compared to the reference atmosphere is equal to a value $\Delta t_{hypothesis}$.' Hence Eq 4.5 can be written as

$$\text{prob}\left(\Delta t_{\text{hypothesis}} \middle| \mathbf{\Delta t_{data}}\right) \propto \text{prob}\left(\mathbf{\Delta t_{data}} \middle| \Delta t_{\text{hypothesis}}\right). \qquad \textbf{Eq 4.6}$$

Now an appropriate hypothesis is defined, the likelihood function must be determined. If a subset of the data is selected with n data then the likelihood function is given by

$$\begin{aligned}\text{prob}\left(\mathbf{\Delta t_{data}} \middle| \Delta t_{\text{hypothesis}}\right) = \text{prob}\left(\Delta t_{\text{data 1}} \middle| \Delta t_{\text{hypothesis}}\right) \times \\ \times \text{prob}\left(\Delta t_{\text{data 2}} \middle| \Delta t_{\text{hypothesis}}\right) \times \\ \ldots \times \text{prob}\left(\Delta t_{\text{data n}} \middle| \Delta t_{\text{hypothesis}}\right)\end{aligned} \qquad \textbf{Eq 4.7}$$

Each term in Eq 4.7 can be calculated individually if a probability density function (pdf) is produced which defines the probabilities of getting a particular value for $\Delta t_{data}$ given $\Delta t_{hypothesis}$. In particular, this should be a function of $\Delta t_{data}$-$\Delta t_{hypothesis}$. §4.1.1 described the distribution as approximately 13 peaks separated by ~1 μs, hence, the pdf used in the sum of 13 Gaussian curves, separated by 1 μs. The width of the Gaussians has been set so that the full width half maximum is approximately 0.9 μs. This value was chosen so that a small but significant dip occurs between each Gaussian; however, the value of this parameter makes little difference to the final result. It has also been seen in laboratory tests

that reflections can occur from the back cases of the API-V sensor casings and if no peak in the directly transmitted signal triggers the clock, then a peak in the reflected signal may do so instead. To account for this the pdf is not allowed to fall below a finite value for $\Delta t_{data}-\Delta t_{hypothesis} > 13$ μs. The pdf is shown in Fig 4.7. Obviously, this rather simple pdf has limitations. For example, the probability of triggering on each peak is not equal and the probabilities may change with altitude. If it were possible to quantify these effects then a much improved pdf could be determined. However, improperly adding these effects would inappropriately skew the results, so, lacking knowledge of these details, this pdf has been used.

**Fig 4.7 Probability density function (pdf) used in the Bayesian analysis. The final pdf is the solid line made up of the sum of thirteen Gaussian curves shown as dashed lines. The pdf does not reach zero at the right hand side to allow for the possibility of reflected signals producing long times of flight.**

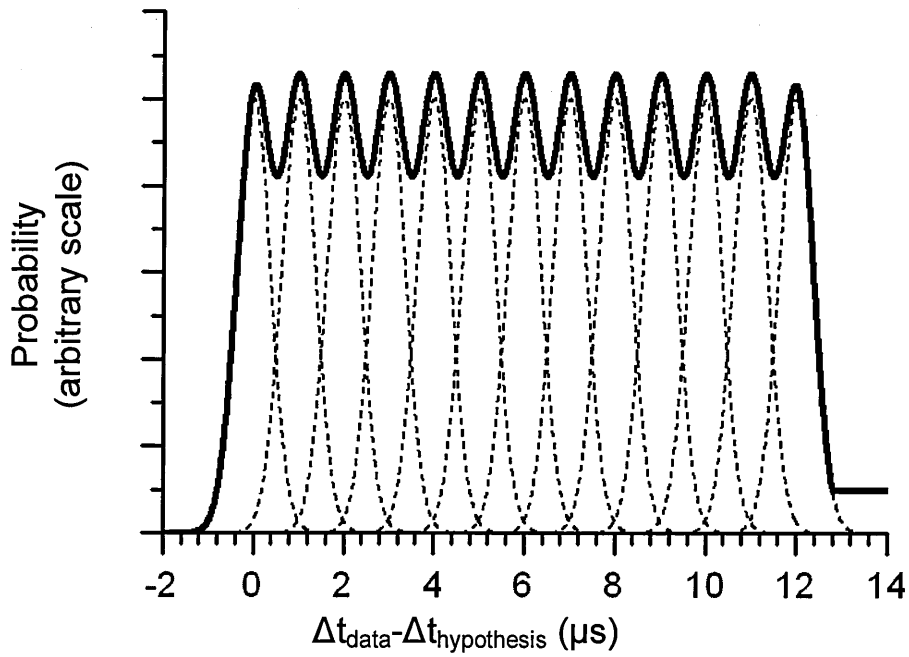


Because the pdf used does not have a single central peak and has steep edges, the data points near the edges are most important in defining the final result. The peaks across the top of the pdf allow correlation with the stripes seen in the data. One disadvantage of this method, however, is that if the spread of the data is less than the ~13 μs width of the pdf then there is an ambiguity in the solution. This can be seen by considering the solution if

the data were only around 12 μs wide. Clearly either the first peak or last peak in the pdf would be redundant, however, as it is impossible to tell which, an ambiguity of 1 μs will occur. This will manifest itself in the solution as two peaks at different values of $\Delta t_{hypothesis}$. Because it is important to ensure that the full spread of the data is represented in each subset of the data used in the analysis, the size of this subset was chosen to be double that used in §4.1.2.1, i.e. 200 data points instead of 100. For each data point, the expected value for time of flight was calculated using the GERG-2004 equation of state using a value for the methane mole fraction of 4.9 %. Again, this is simply a reference to remove the contribution of temperature. This was subtracted from the data to generate values for $\Delta t_{data}$ and subsets of 200 data points starting from the surface were taken to perform the Bayesian analysis. The GERG-2004 reference values were then added back to the results of the Bayesian analysis to provide solutions in terms of the time of flight. The results, along with the measured time of flight data, are shown in Fig 4.8. On the plot the black areas represent high probability and a white background represents zero probability. Essentially, the plot shows a black line which represents the best solution. Although it is difficult to see on this scale, the black line actually has a smooth transition into the white background along either side. Given the pdf chosen, the narrowness of the line shows how high the degree of confidence in the solution is. There are some altitudes where more than one line exists, giving two potential solutions. However, in these cases, one line is found to be more probable than the other (represented by the darker line) and is hence preferred. Multiple black lines would imply that the spread of the data was less than 13 μs as discussed above, but the lighter shading of one line may be caused by a lower than expected number of data points at one edge of the spread. In some cases there are discontinuities where different solutions for different subsets of the data meet. This could be caused by changes in composition on altitude scales greater than covered by one subset, i.e. of the order 1 km.

**Fig 4.8 The result of Bayesian analysis on subsets of 200 data points. The black line shows the most probable solution at that particular altitude. The white background represents zero probability and grey areas are intermediate probability.**

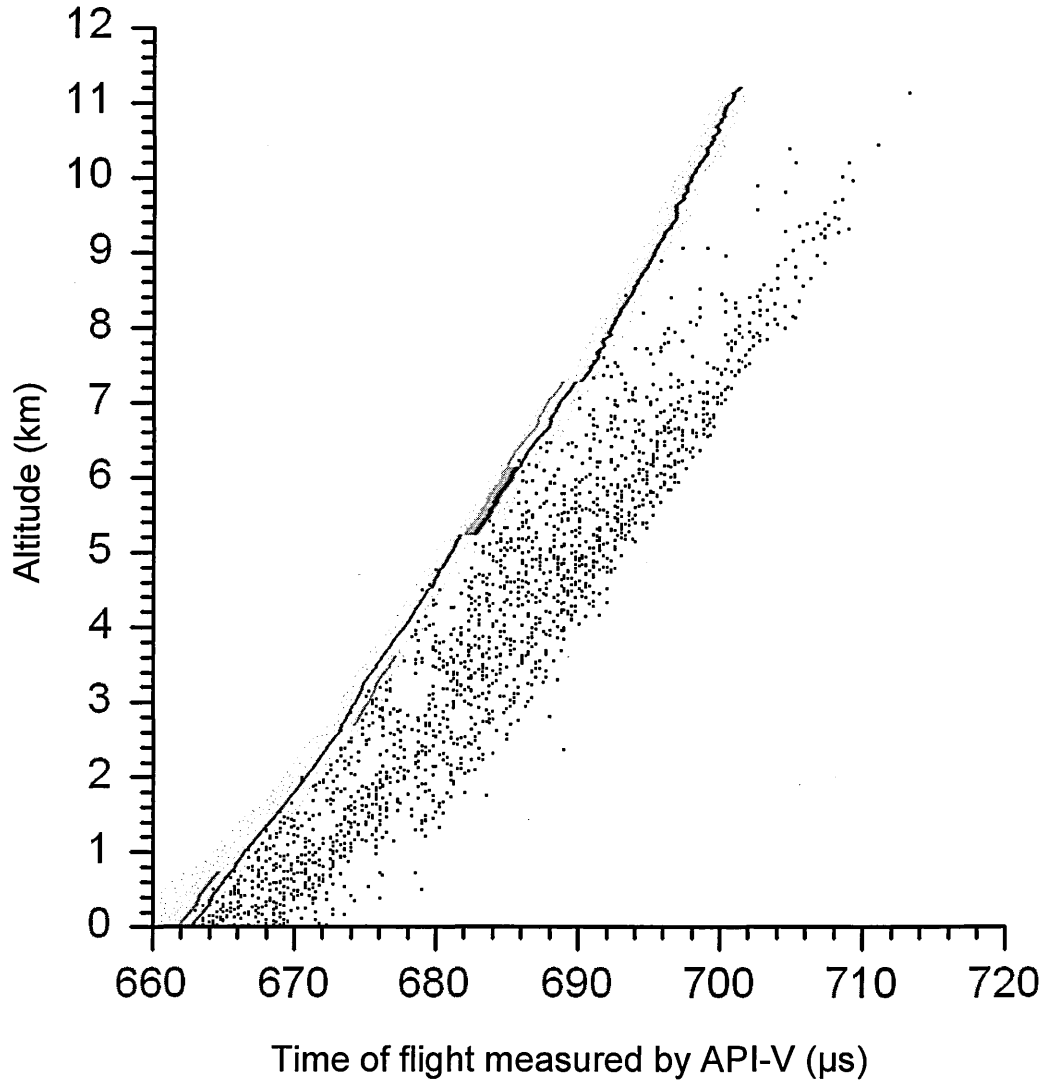


### §4.1.3 Resultant Speed of Sound

The results of the lower limit and Bayesian analysis techniques can now be used to generate the speed of sound in Titan's atmosphere. The speed of sound is given simply by dividing the separation by the time of flight; however, the separation is a function of temperature. At room temperature the separation between the two faces of the API-V sensors was 128.9 mm and was expected to shrink at cold temperatures as discussed in 0. The results of both data analysis methods are given in Fig 4.9. The two results match very well which increases confidence in their accuracy. The maximum deviation between the two methods is ~0.3 m $s^{-1}$.

**Fig 4.9 Speed of sound in Titan's atmosphere as determined by API-V. The red dots show the sound speed as calculated by the upper limit method of §4.1.2.1 and the line is the result of the Bayesian analysis of §4.1.2.3. As in Fig 4.8 the black line represents the highest probability solution and white indicates zero probability. Grey represents intermediate solutions. The estimated uncertainty in the results is ±0.3 $ms^{-1}$ as shown as a single error bar.**

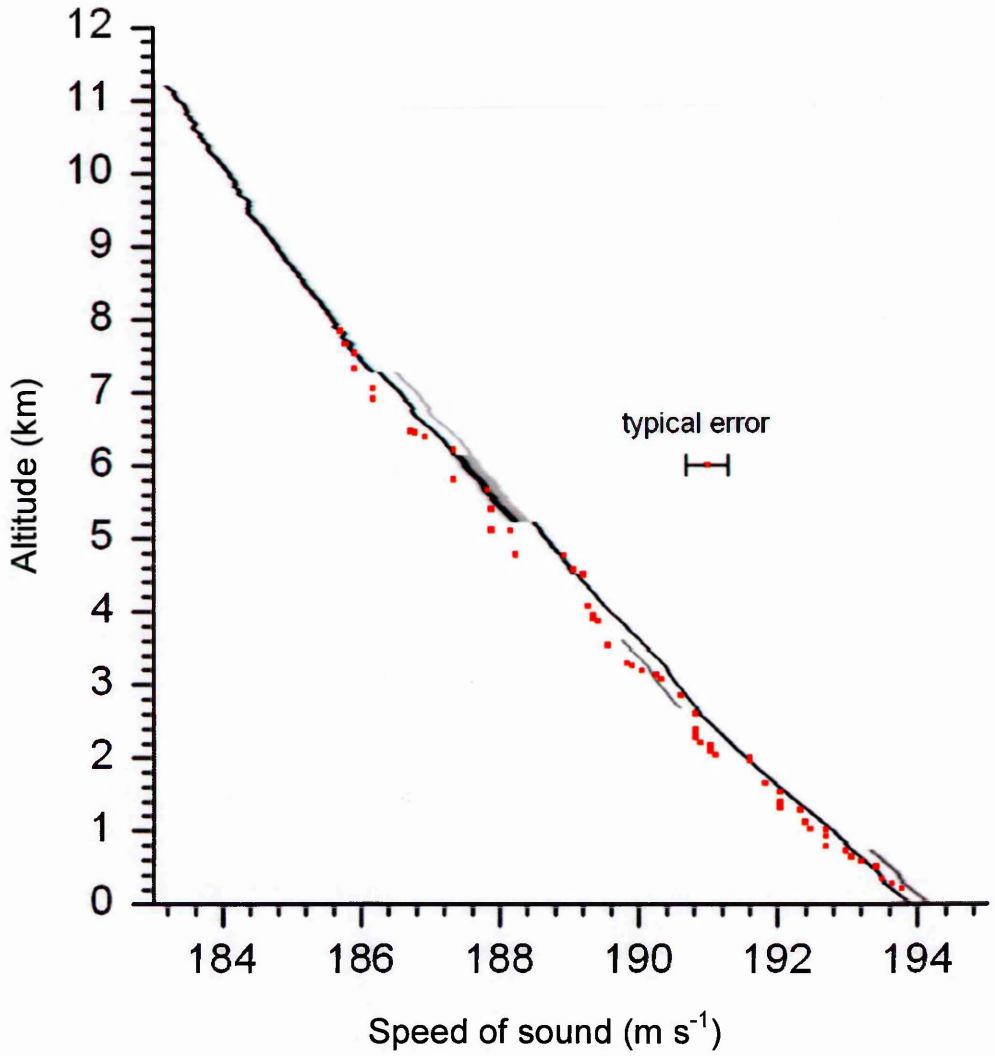


Although the sensors took measurements with a resolution of 0.25 μs, the added complication of performing the analyses described here warrants increasing the uncertainty somewhat. A value of 1 μs has been selected as it is equivalent to one period of the wave train. Hence, this allows for the analysis techniques to miss the correct solution by one peak of the sound wave. Combining this with the uncertainty in the separation of the sensors of 0.1 mm as discussed in 0 gives an estimate of the uncertainty in speed of sound

measurements of $\pm 0.3\ ms^{-1}$. This matches with the deviation seen between the two methods.

## §4.2 Surface Data

The data gathered by API-V on Titan's surface, as shown in Fig 4.11, represents a complex story that perhaps, may never be fully understood. The probe impacted the surface at 8869.7598 s after $t_0$. By 8872 s after $t_0$ the Surface Science Package had changed its mode of operation from proximity mode to surface mode. Before impact API-V was making successful measurements of time of flight on about two thirds of its attempts, the remaining one third being timeout values or interference from ringing. After landing, only 10 of the first 32 measurements were successful and then API-V returned timeout for 217 seconds except for one measurement. At 9050 s after $t_0$ SSP changed from surface mode to extended surface mode and at 9103 s after $t_0$ successful measurements began to be taken again. This gap can be clearly seen in Fig 4.2.

The cause of this poor performance just after impact is unknown. Perhaps, upon landing, surface material entered the Top Hat. The penetrometer indicated that the top 5mm of the landing site consisted of very fine grained soft material that could potentially pass through the electromagnetic shield across the opening (Zarnecki, et al. 2005). If fine grain material was deposited on the sensors, or formed an obstruction between the sensors, then this could inhibit the sensors functioning. If this material slowly fell off the sensors, perhaps by sliding down their faces, or evaporated away, then the sensors would begin working again. Fig 4.1 shows that no false triggering due to ringing occurred after landing which again could be consistent with increased damping due to material inside the Top Hat coming into contact with the sensors. However, if material inside the Top Hat was preventing the sensors from functioning, it is difficult to understand how a few measurements were able to be taken almost immediately after landing, prior to the sensors stopping.

It seems unlikely that the poor function is related to the change in mode of operation of SSP. The improvement in performance occurs over a minute after the change to extended surface mode and any software or hardware bug caused by a change in mode would be expected to correlate precisely with the mode change events.

Once functioning again, API-V worked much better on the surface than during descent, with the spread being generally much lower. However, ~700 s after landing the spread of the data increased and more timeouts were generated. Eventually the occurrence of timeouts increased until the last successful measurement was made at 10517 s after $t_0$.

Hypotheses for the increase in spread and eventual cessation of function of API-V can be formed, although it is impossible to test these hypotheses effectively. They should, therefore, be regarded as speculative possibilities rather than definite conclusions.

Timeout data was still being recorded from API-V indicating that the signal strength became too weak to trigger the clock. If the ground was wet with methane, as has been indicated (Niemann, et al. 2005; Lorenz, et al. 2006a), and if this methane was being evaporated into the Top Hat, then perhaps the API-V sensors, close to the ground, formed a cold surface on which condensation could occur. This would reduce the effectiveness of the sensors and increase the spread or cause the sensors to cease functioning altogether. Another, rather speculative, possibility, is that if the ground was sufficiently saturated then the depression formed by the impact of Huygens (Zarnecki, et al. 2005) could have slowly filled with liquid methane. The API-V sensors could have then become submerged. If Huygens was horizontal and the depression filled, then it would be expected that the time of flight would have changed dramatically to represent the transition into liquid. However, images from the surface indicate an upward pitch of around 1.7° (Tomasko, et al. 2005), hence, one of the API-V sensors could have become submerged prior to the other. This would place the plane of the liquid surface between the two sensors, reflecting the emitted sound wave as shown in Fig 4.10. It would be expected that as the liquid level increased, covering the lower sensor, the strength of the signal travelling between the sensors would

reduce until such a large fraction of the sensor face was covered that the signal strength became too low to be detected.

It also seems that the spread of data at late times on the surface is larger than the spread in the atmosphere and varies in an almost periodic fashion as time passes. This may be explained by invoking reflections off a nearby liquid surface, increasing the distance travelled by the wave train and creating interference. This could change the signal strength at the receiving sensor as the liquid level changed.

**Fig 4.10 Effect of fluid on API-V sensors if not horizontally aligned. A moderate tilt could cause reflections that would produce interference above the liquid level or reflect the signal away altogether below the liquid level. A larger tilt would allow more of the lower sensor to become submerged meaning less signal could travel between the sensors stopping the sensors functioning.**

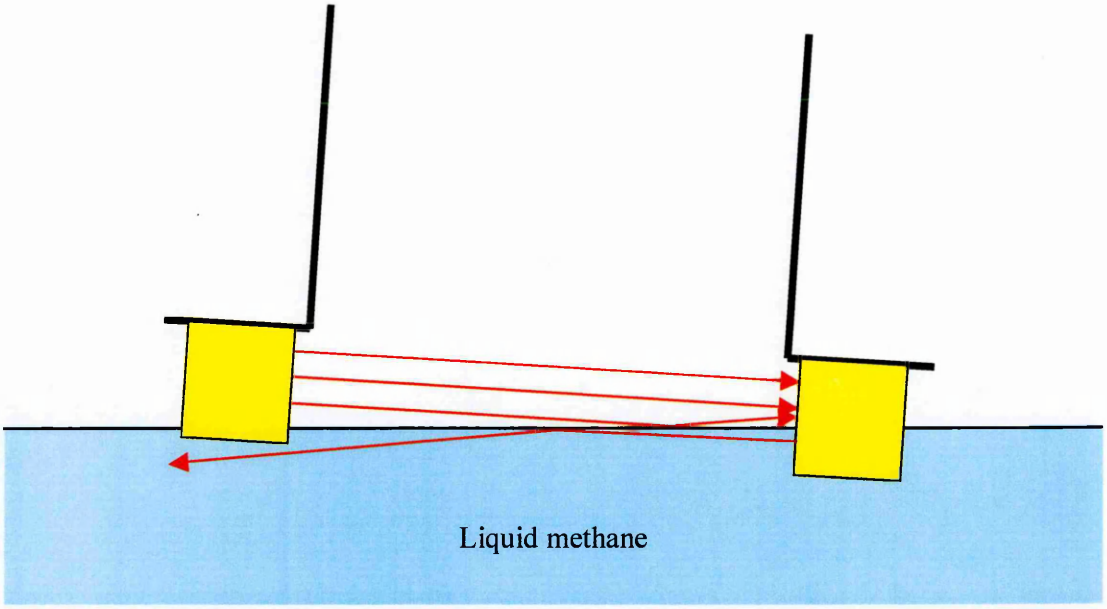


The idea of liquid filling the depression is also consistent with data gathered by the Acoustic Properties Instrument - Sonar (API-S) after impact. Although the surface was too close to be seen by the sonar, the instrument rang, i.e. continued vibrating after the transmit pulse was sent due to low damping, with this ringing being recorded. At a time of 1270±50 s after impact the ringing of API-S became greatly reduced and a rising liquid could be responsible for damping this ringing (M. C. Towner, personal communication).

These are all rather speculative possibilities which may be consistent with the surface data. The only laboratory measurements that have been made to find out what the effects of liquids would be on the sensor involved full submersion (Garry 1996). Future work to constrain these speculations may be possible by using a liquid which is stable at room temperatures and does not conduct electricity, such as isopropyl alcohol.

Another feature worth considering is that the measurements made immediately after impact do not match the results of the upper limit and Bayesian analysis of the atmospheric data immediately before impact. Fig 4.2 shows that the time of flight measured on the surface is larger than that during descent by approximately 5-6 μs. This change is difficult to explain. Either the speed of sound has altered or the separation of the sensors has increased by ~1 mm. The change in sound speed would require either a drop in temperature, or an increase in the mean molecular weight of the atmosphere. However, no temperature decrease was measured inside the Top Hat by any of the engineering temperature sensors. To alter the separation of the sensors would likely require deformation of the Top Hat. Taking a model for deforming an annulus of material (Timoshenko & Woinowsky-Krieger 1959) it has been calculated that deforming the metal reinforcing ring at the base of the Top Hat by 1mm would require a force of ~12 kN . It is difficult to imagine how such a large force could be applied to the side of the Top Hat structure. It is also difficult to imagine how the sensors themselves could be bent without the direction of their beam being altered, permanently preventing them from working. Another method by which the separation could be increased is by removing the impedance matching layers from one or both of the sensors. These layers are 0.7 mm thick and their removal would increase the time of flight by approximately 3 μs each. It is impossible to state, with much certainty, the force of impact that would have been required to cause these layers to become detached. Peak atmospheric deceleration was ~120 m $s^{-2}$, similar in magnitude to the ~175 m $s^{-2}$ measured at impact. However, the Top Hat was, at least partly, dynamically isolated from the Huygens accelerometer by a set of expansion

bellows, so SSP could have experienced a greater deceleration. In fact, it is likely that the penetrometer hit a cobble on Titan's surface (Zarnecki et al. 2005) so such a scenario is rather plausible. This theory has one significant problem, if the impedance matching layer was detached from both sensors then the transmission coefficient would drop to approximately $1.5\times10^{-3}$. This is lower than the value of $3.15\times10^{-3}$ required for operation. Even if only one impedance matching layer was detached the transmission coefficient would be reduced to $2.8\times10^{-3}$.

**Fig 4.11 Data collected by API-V after impact on Titan's surface.**

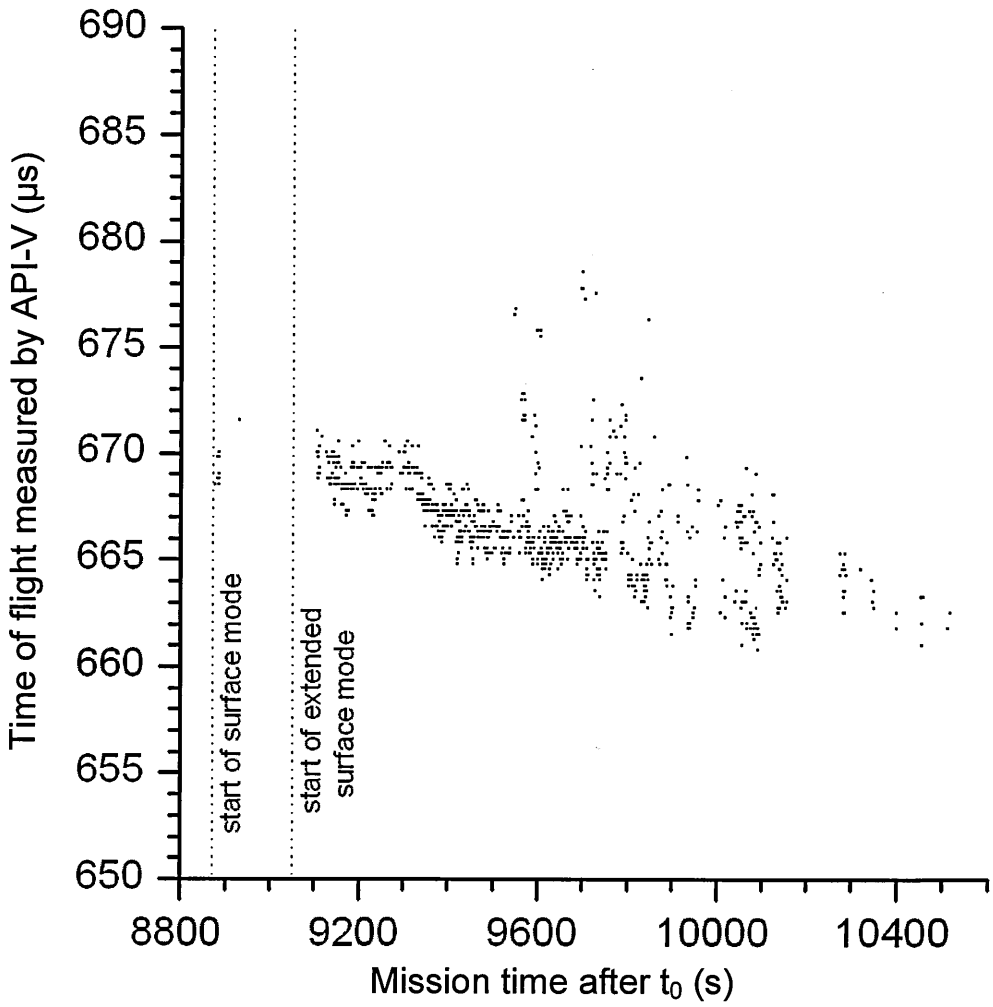


## §4.2.1 Data Analysis

Due to the uncertainty in the both the conditions after landing and cause of the increase in spread, it is difficult to state with high confidence exactly how the data should be best

analysed and which, if any, of the techniques described in §4.1.2 is appropriate. As a result of these difficulties, every data point collected after landing has been treated as an independent measurement and the associated speed of sound calculated. Some of the data, such as that between 9100 and 9400 s after $t_0$, show clear stripes. This makes it tempting to apply the simulated annealing method discussed in §4.1.2.2. However, as no satisfactory explanation has been devised to explain the increase in spread after $t_0$+9500 s, such an analysis of the whole surface dataset could be misleading. Equally, applying the upper limit method would unnecessarily remove detail from this region and hence it was decided that each data point should be treated independently as an upper limit of the time of flight and a lower limit of the speed of sound.

**Fig 4.12 The speed of sound as measured by API-V after Huygens' impact on Titan's surface. None of the analysis techniques from §4.1.2 have been used and each data point should be considered as a lower limit for the speed of sound.**

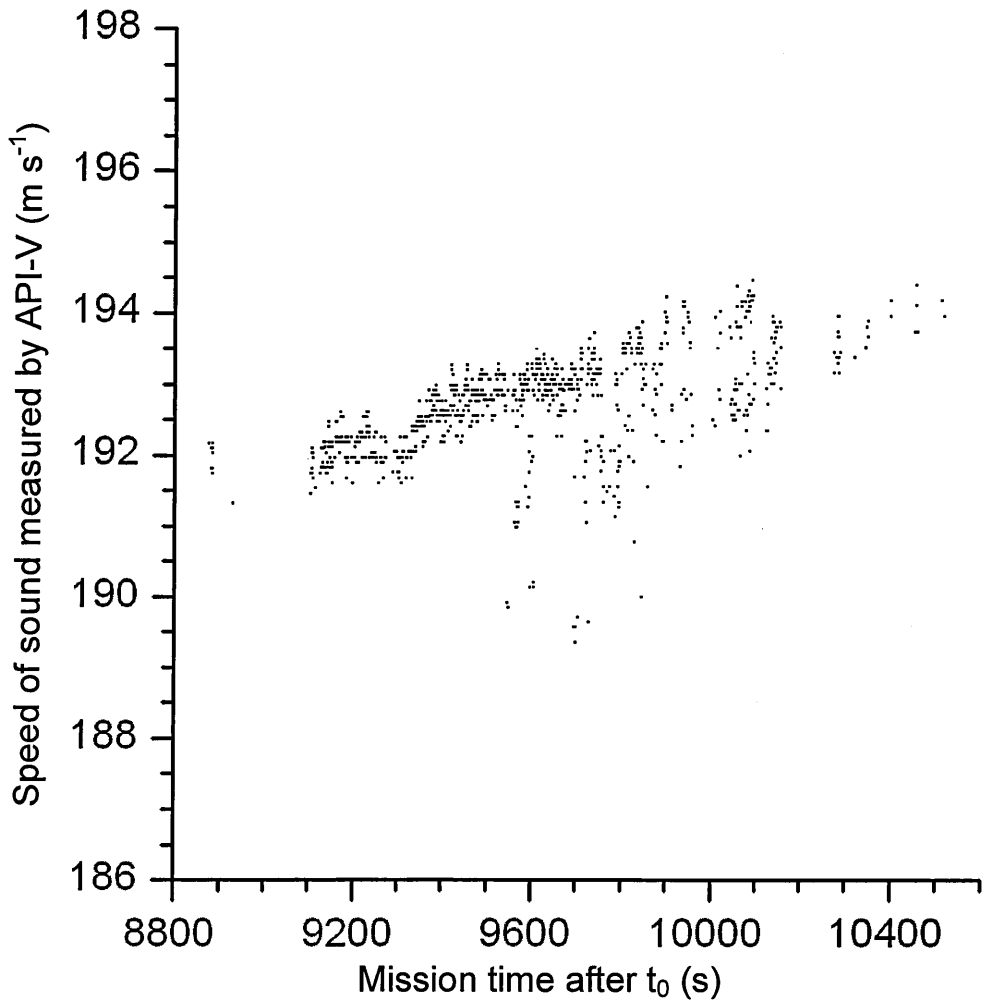

To determine the speed of sound, the separation must be known accurately and, as has been discussed, there may be some doubt about the separation after landing. In addition, as with the surface data, the separation varies slightly with temperature. As no temperature sensor is located at the base of the Top Hat it is difficult to know the temperature after landing. A number of temperature sensors are, however, located inside the Top Hat which all show some rise in temperature after landing. It was decided that the refractive index sensor mounting structure temperature sensor would be most representative therefore this was used to determine the thermal expansion of the Top Hat. However, the thermal expansion coefficient is relatively small and most temperatures measured inside the Top Hat are similar. Therefore, there is a negligible difference in the calculated separation if other temperature sensors are used.

The speed of sound profile presented in Fig 4.12 shows the speed of sound measured, assuming that the separation did not alter after Huygens' impact with the surface.

# Chapter 5
# Interpretation of API-V Results

## §5.1 Atmospheric Methane Concentration

For each sound speed measurement made by API-V, the composition has been calculated based on the conditions measured by the HASI TEM temperature sensor and PPI pressure sensor (Fulchignoni, et al. 2005; Harri, et al. 2006) and the GERG-2004 equation of state, which, in §3.4, was determined to be the most appropriate equation of state for representing Titan's conditions.

To determine atmospheric composition from the API-V data the assumption was made that the only two bulk constituents of Titan's atmosphere were methane and nitrogen. Before Huygens arrived at Titan, the available data were consistent with a third bulk constituent, argon, also being present (Lindal, et al. 1983; Lellouch, et al. 1989; Samuelson, et al. 1997); however, the Huygens GCMS found argon in only trace amounts. Should any unknown constituents be present in Titan's atmosphere with a molecular weight greater than methane, the methane abundances presented in this chapter would be an underestimate.

Chapter 4 presented two datasets for the speed of sound, one based on the upper limit method and a second based on the Bayesian method. Both of these datasets have been used to generate methane abundance estimates. For the data points from the upper limit dataset, the conditions at the time of measurement were estimated by interpolating the temperature and pressure data using a cubic spline fit. These temperatures and pressures were initially used with the GERG-2004 equation of state to find the speed of sound for mixtures of 0 and 10 % methane; a simple bisection method was then used to find a methane concentration which agreed with the speed of sound measurement. For the Bayesian analysis, the temperature and pressure for each pixel on Fig 5.1 were determined, again

using a cubic spline interpolation of the HASI data. The methane abundance, read from the x axis below that pixel, was used to determine a value for the hypothesised speed of sound and hence time of flight. This time of flight was then used to form the basis of a Bayesian analysis as described earlier in §4.1.2.3. As in Fig 4.8 and Fig 4.9, at any given altitude the most likely solution is represented by black; white areas represent solutions with zero probability. The resulting methane abundance estimates are shown in Fig 5.1.

**Fig 5.1 Atmospheric composition based on API-V data using the upper limit and Bayesian techniques discussed in §4.1.2.3. The black shading represents maximum probability of a correct solution and the white areas represent zero probability of a correct solution. Also Shown are the Huygens Gas Chromatograph Mass Spectrometer data (Niemann, et al. 2005) and the predicted saturation levels generated using the GERG-2004 and NIST database 14 equations of state.**

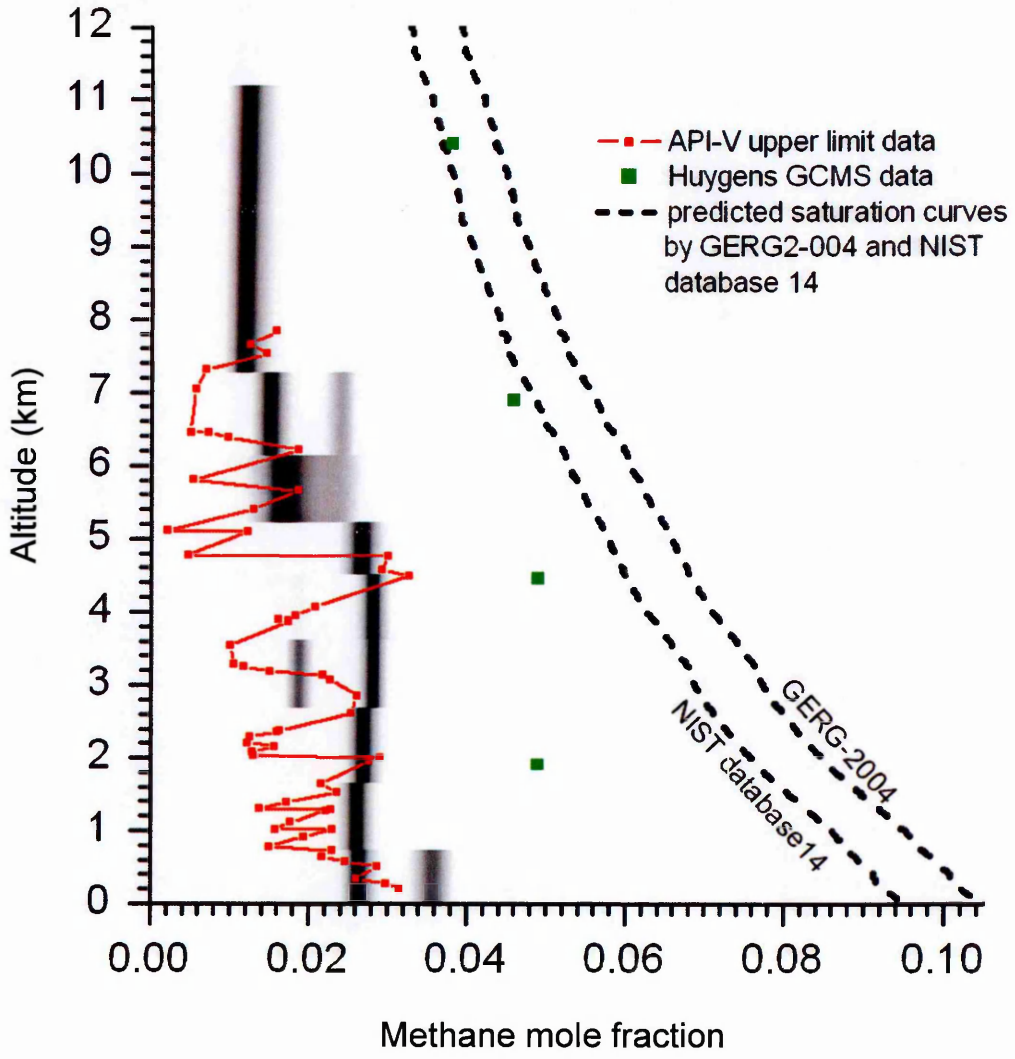

In addition to the API-V composition estimates, the measurements from the Huygens GCMS (Niemann, et al. 2005) and the predicted saturation profile are plotted on Fig 5.1. Two saturation curves are shown, one is the prediction by the GERG-2004 equation of state and the second is the prediction by the NIST equation of state. Both are based on temperature and pressure data provided by HASI (Fulchignoni, et al. 2005; Harri, et al. 2006). As was described in §3.4, laboratory data at the very cold temperatures found on Titan for comparison to the equation of state estimates do not exist. The coldest relevant experimental data that could be found in the scientific literature were produced by Stryjek, et al. (1974). This work provided measurements of vapour mole fractions of nitrogen-methane mixtures at temperatures of 113.7 K and pressures from 0.208 to 1.72 MPa. Fig 5.2 shows that the closest match to these data was the GERG-2004 equation of state; however both GERG-2004 and NIST database 14 underestimated the methane mole fraction compared to the Stryjek data.

**Fig 5.2 plot comparing predicted and measured saturation mole fractions of methane in a methane nitrogen mix at 113.7 K**

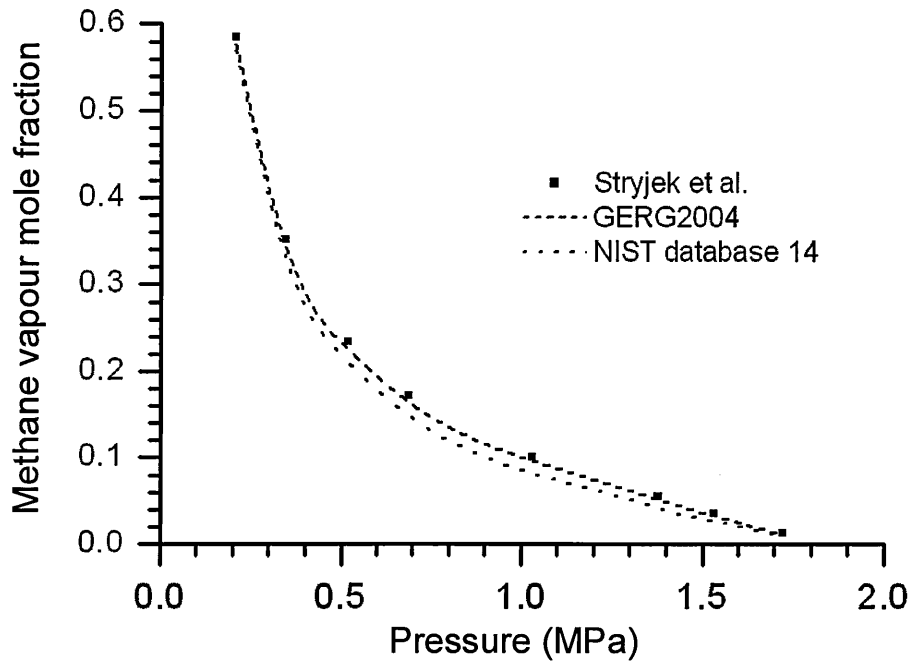


The API-V upper limit data in Fig 5.1 show a considerable spread in mole fraction of around 0.02. Some of this scatter is almost certainly noise such as at that occurring at

around 1 km altitude, however, at around 3 km altitude there is a smooth decrease and then an increase in methane abundance covered by 10 data points, which may represent a true change in composition. Regardless of the source of the scatter, these data do show a general trend of decreasing methane abundance with increasing height.

The Bayesian analysis gives a much clearer interpretation of the API-V data. It shows a methane mole fraction from the surface to ~5 km of approximately 0.026–0.029 with a slight trend to increasing concentration with increasing altitude. Above 5 km the methane abundance decreased with height to a mole fraction of 0.012 by 7.2 km. The vertical resolution of the Bayesian varies with altitude because each analysis was performed using 200 points. As API-V makes successful measurements more frequently and is descending slower at low altitudes, the resolution is better here. However, below 7 km the resolution is better than 1 km. The apparent constant composition above 7.2 km is caused by the low resolution of the analysis which is in turn due to the sparse nature of data at this altitude. The analysis also indicates the possibility of an increased mole fraction at the surface and a diminished mole fraction at 3 km in the form of a lower probability alternate solution. Although in both cases a more probable solution exists, the possibility of the alternative solutions is non-negligible; they both have probabilities of approximately half the preferred solution. The discontinuity of the alternative solutions could be explained by changes in abundance over smaller scales than the ~1 km resolution of the analysis. As more probable solutions to the Bayesian analysis exist and as Titan's troposphere is expected to undergo convection and be well mixed, it seems likely that these variations are the result of the probability density function used in the Bayesian analysis not being a perfect representation of the scatter in the data.

It should be noted that the composition derived here is slightly lower than that derived in a similar analysis of the API-V data by Hagermann et al. (2007). In the work of Hagermann et al., the derived composition from the surface up to around 5 km altitude was 0.033 and constant compared to 0.026-0029 in this analysis. This difference occurred because a

different probability density function was used in the Bayesian analysis and also a different number of data points were used in each altitude band. In the Hagermann et al. analysis the probability density function did not allow any data point to have a value of $\Delta t$ greater than 13 μs, unlike that used here as shown in Fig 4.7. In addition, the Hagermann et al. work assumed that the atmospheric composition was constant unless two data points provided mutually exclusive solution. Only then was composition allowed to vary. This work splits the data into blocks of 200 data points and allows each of these blocks to define an independent solution. The uncertainty in the speed of sound presented in Chapter 2 was $\pm 0.3$ m $s^{-1}$. This translates to an uncertainty in mole fraction of 0.011. Hence, the difference between this analysis and that by Hagermann (2007) is within the uncertainty.

There is also a contribution to the uncertainty in composition from the uncertainty in temperature. The expected uncertainty in temperature measurements is 0.25 K which translates to an uncertainty in mole fraction of 0.012. Because the dependence of the speed of sound upon pressure is low, the uncertainty in the pressure measurements has a negligible effect. Of course, the accuracy of the equation of state also contributes to the overall uncertainty. The contribution caused by the equation of state is difficult to estimate due to the lack of experimental data; however, the claimed accuracy for the speed of sound measurements for the GERG-2004 equation of state is of the order 0.1 %. This equates to an uncertainty in mole fraction of 0.008. If we combine these three sources of uncertainty then a final uncertainty is reached of $\pm 0.018$. Of course summing uncertainties in this way is not valid in the case of systematic uncertainties, such as for the equation of state uncertainty, though this figure may serve as an approximate guide to the accuracy of the measurements.

The API-V data provide consistently lower estimates of the methane mole fraction compared to the GCMS, although the overall trend is similar. Measuring abundances with a mass spectrometer is a challenging procedure requiring careful calibration and an unconsidered factor in the GCMS measurements could potentially create a systematic

offset. There is also the possibility for systematic offsets to occur in the estimates presented here. Three possible reasons for API-V to have underestimated the methane abundance are:

- API-V may not ever have triggered on the first peak of the wave train during atmospheric descent causing sound speed and hence the methane abundance to be underestimated. For every peak that may have been missed in this way the methane mole fraction would have been underestimated by ~0.008. For this effect to be wholly responsible for the difference between the API_V and GCMS composition estimates, two to three peaks would have to have been missed. The conditions during the measurement were clearly difficult for the operation of the sensor and hence it is plausible that missing some peaks has had an effect. However it should be noted that in §4.1.1 it was found that the spread of the data was a good match to the length of the wave train. This may indicate that even the first peak was regularly detected.
- As manufacturing tolerances can never be absolutely zero, the flight spare sensors, used for calibration, may have differed slightly from the flight model. Details such as the dimensions of the piezoelectric crystal or thickness of the impedance matching layer may have varied. This could mean that the offset described in §2.2.4 may not be correct. However it is likely that differences between the sensors would have had a relatively small impact upon the final result. Although specific tolerances are not available the sensors were made from nominally identical high quality parts, as would be expected for any space mission. To cause the speed of sound to be underestimated by the value predicted by the GCMS would require the piezoelectric crystals and impedance matching layers of the flight sensors to be 2.5 times the thickness of those used for the flight spare. Differences of a few percent seem more likely for such parts.

- The methane abundances derived from API-V measurements are entirely dependant upon the accuracy of the equation of state used. It has not been possible to compare the equation of state used with laboratory data under Titan-like conditions and the variation between models seen in Chapter 3 is testament to the difficulty in modelling properties of non-ideal gas mixtures. This particular part of the analysis is largely out of the control of the author. Ideally, accurate measurements of the speed of sound under Titan-like conditions would be performed. Unfortunately such measurements are difficult to perform, especially as the temperatures in question are close to the condensation point of methane and nitrogen. The results of such measurements do not exist in he scientific literature and they were not able to be made as part of this work. This means that, for the conditions present on Titan , the available non-ideal equations of state are essentially interpolations and extrapolations of fits to other data. The result of such extrapolations is that predictions of the speed of sound differ by up to 1 m $s^{-1}$ between equations of state. Such variations could cause variations in the estimated methane mole fraction of up to ~0.04. This variation alone could cover the difference between the API-V and GCMS results and improvement of equations of state would be key to the further use of a speed of sound sensor for investigating planetary environments.

Of the possible reasons discussed above, it is likely that the largest contributor to a systematic error in the methane abundance estimates is the uncertainty caused by the equations of state. As equations of state tend to rely on empirical fitting to experimental data, their accuracies poorly defined where no experimental data exists. There may also be some contribution due to missing the first peaks in the wave train. However, to produce the spread of data seen by API-V, this would require that the damping within the sensors was very low, allowing the piezoelectric crystals to ring for 4 or 5 wave-cycles after the nominal 10 cycle duration of the wave train. This is not seen in the laboratory.

Although there are possibilities for inaccuracies in the API-V estimates of composition, this does not preclude the possibility that the GCMS measurements may be systematically overestimating the methane abundance. The currently published GCMS measurements are still only preliminary and further work is ongoing. A mass spectrometer is a very useful detection unit for determining if a particular species exists within a sample, however, making abundance estimates based on mass spectrometer data is difficult. This is because a molecule such as methane can be broken into smaller species (e.g. hydrogen atoms or methyl groups) by the ionisation process employed. This means that any composition estimate is dependant upon the model of molecular breakup employed. Further comparisons would be made if updated results are published.

### §5.1.1 Atmospheric Implications

Detailed dynamical atmospheric modelling is beyond the scope of this work; however, some of the implications for Titan's weather are presented here. Titan's weather can be thought in some ways to be analogous to the Earth's. Titan has a troposphere, inside which air, heated by the ground, can become unstable to convection. Methane on Titan may then perform a role similar to that of water on the Earth, creating a possibility for condensation and precipitation to occur. Indeed, images taken during Huygens' descent show a number of fluvial features (Tomasko, et al. 2005).

The GERG-2004 equation of state can be used to determine the adiabatic lapse rate on Titan, given the atmospheric pressure profile provided by HASI. As the implementation of the equation of state does not allow calculation of the appropriate differentials, an iterative process was used. An initial guess was used for the lapse rate near the surface. A small increase in altitude was then applied and the lapse rate was used with the GERG-2004 equation of state to calculate the heat capacity and change in density at the new altitude. These values were in turn used to calculate the adiabatic change in temperature using the 1$^{st}$ law of thermodynamics,

$$\Delta T = -\frac{P\Delta V}{c_v}. \qquad \textbf{Eq 5.1}$$

Inevitably the initial guess for temperature change and the value calculated with Eq 5.1 did not match. The initial guess was therefore modified and the process repeated in an iterative manner until a consistent value for the lapse rate was determined. The adiabatic lapse rate for the surface of Titan was found to be -1.25 K $km^{-1}$, slightly lower in magnitude than the ideal gas value of -1.32 K $km^{-1}$ determined in a similar manner. Although large sections of Titan's troposphere have lapse rates smaller than the adiabatic lapse rate (Fulchignoni, et al. 2005) and the atmospheric profile measured by HASI is likely to be stable to convection (Barth & Rafkin 2007), the HASI accelerometry measurements have been used to show that as Huygens descended, there may have been a slow upward atmospheric flow with a velocity of approximately 0.1 m $s^{-1}$ (Teemu, et al. 2006) in the troposphere. As the atmosphere above the landing site was stable to convection, this upward flow was attributed to global circulation. In a similar manner to upward atmospheric flow on Earth, it may be expected that as moist (or methane laden) air rises adiabatically, it will cool and condensation may occur. The GERG-2004 equation of state has been used to determine the methane saturation mole fraction for a pocket of air which rises adiabatically from the surface based on conditions measured at the Huygens landing site. The results shown in Fig 5.3 reveal that for a surface methane mole fraction of 0.026 condensation will begin to occur at an altitude of 9.2 km, whereas for the methane mole fraction of 0.049, as measured by GCMS, condensation will begin at 6.9 km altitude. Note that although the plot reaches zero methane content by 16 km, this does not imply that all methane condenses by this altitude. The plot assumes a dry adiabatic lapse rate as calculated earlier and once methane condensation begins the latent energy released invalidates this assumption. This plot is hence only valid below any cloud layer.

**Fig 5.3 Saturation mole fraction of methane for a pocket of air rising adiabatically from Titan's surface. This plot ceases to be valid above any condensation layer.**

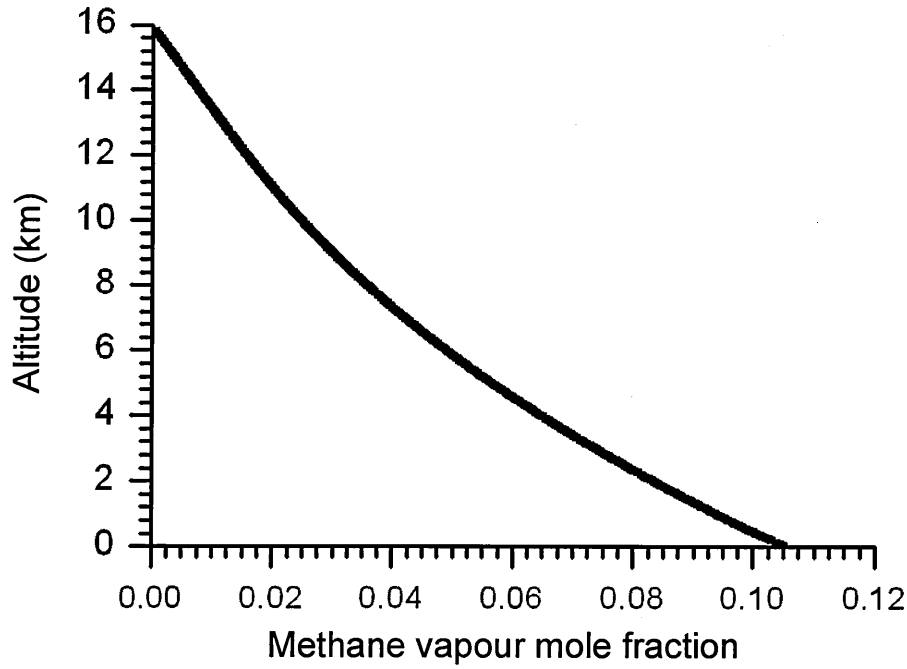


No cloud was seen during the descent, either by the cameras or in measurements of atmospheric opacity (Tomasko, et al. 2005), despite the slow upward motion measured by HASI. However, Barth & Rafkin (2007) recently modelled cloud formation, predicting that stratiform clouds could form at the Huygens landing site. Tokano (2006) also postulated a sub-visible, non convective, stratus type methane cloud with dissolved nitrogen above ~8 km that was producing drizzle at the time of Huygens' descent. As Titan's atmosphere is dense and its gravity weak, the time taken for a small raindrop to descend to the surface can be longer than the time taken for evaporation (Lorenz 1993), so if it was drizzling when Huygens landed on Titan, the evaporation of fine raindrops in the atmosphere could explain the slight increase in methane abundance seen in Fig 5.1 from the surface to 5 km altitude.

Detailed modelling of cloud formation on Titan should, however, be considered with caution. Significant differences can occur with different equations of state as seen in Fig 5.1 and until experimental data exist for Titan-like conditions, it is difficult to make an informed decision about which equation of state is most suitable.

## §5.2 Interpretation of Surface Data

The surface data produced by API-V is difficult to interpret, as the temperature environment after landing, (when the Top Hat was likely sealed off by the ground below) was very different to that during descent and as there was no temperature sensor in the vicinity of API-V, the new conditions were poorly understood. For this reason there are at least two possible contributions to the increase in sound speed after landing.

- Once on the ground, without the forced convection that occurred during descent, the temperature within the Top Hat increased significantly. This is seen on all the engineering sensors within the cavity. However, each sensor is in a different thermal environment and measures a different temperature. For example, the Thermal Properties Instrument, which is itself a large source of heat and located at the deepest point within the Top Hat, sees the largest temperature rise.
- There is tantalising evidence that heat transmitted to Titan's surface from the probe led to evaporation of methane that was present in liquid form amongst the granular surface material (Niemann, et al. 2005; Lorenz, et al. 2006a). If methane was evaporated from the surface, this would have caused an increase in the speed of sound in the Top Hat.

Unfortunately, without constraints on the temperature change, it is impossible to tell how much, if any, of the change is caused by increased methane fraction. However, the limiting cases can be determined by assuming that either temperature or methane abundance do not change after landing.

As was discussed in §5.2, there was a discontinuity in time of flight measurements after landing - the time of flight data after landing were higher than that before. One result of this is that the speeds of sound calculated are unphysical, i.e. no mixture of nitrogen and methane can give speeds of sound as low as measured by API-V for sensible temperatures and pressures after landing. This change could potentially be caused by an extra

component being added to the atmosphere although as there is no evidence from the GCMS of any other constituents increasing enough to make this a likely possibility. Despite this, the relative change in sound speed on the surface may provide useful information. Hence to investigate this, it has been assumed that the time of flight measured after landing was 6 μs too long. As was discussed in §5.2 this is the extra time of flight that would be expected if the impedance matching layers on the front face of the sensors became detached, one of the possible reasons for the discontinuity. Although the reason for the discontinuity is not known with any great certainty, this assumption provides

**Fig 5.4 Methane abundance from API-V surface data, assuming no temperature increase. Note that a 6 μs offset has been applied to the data as discussed in the text.**

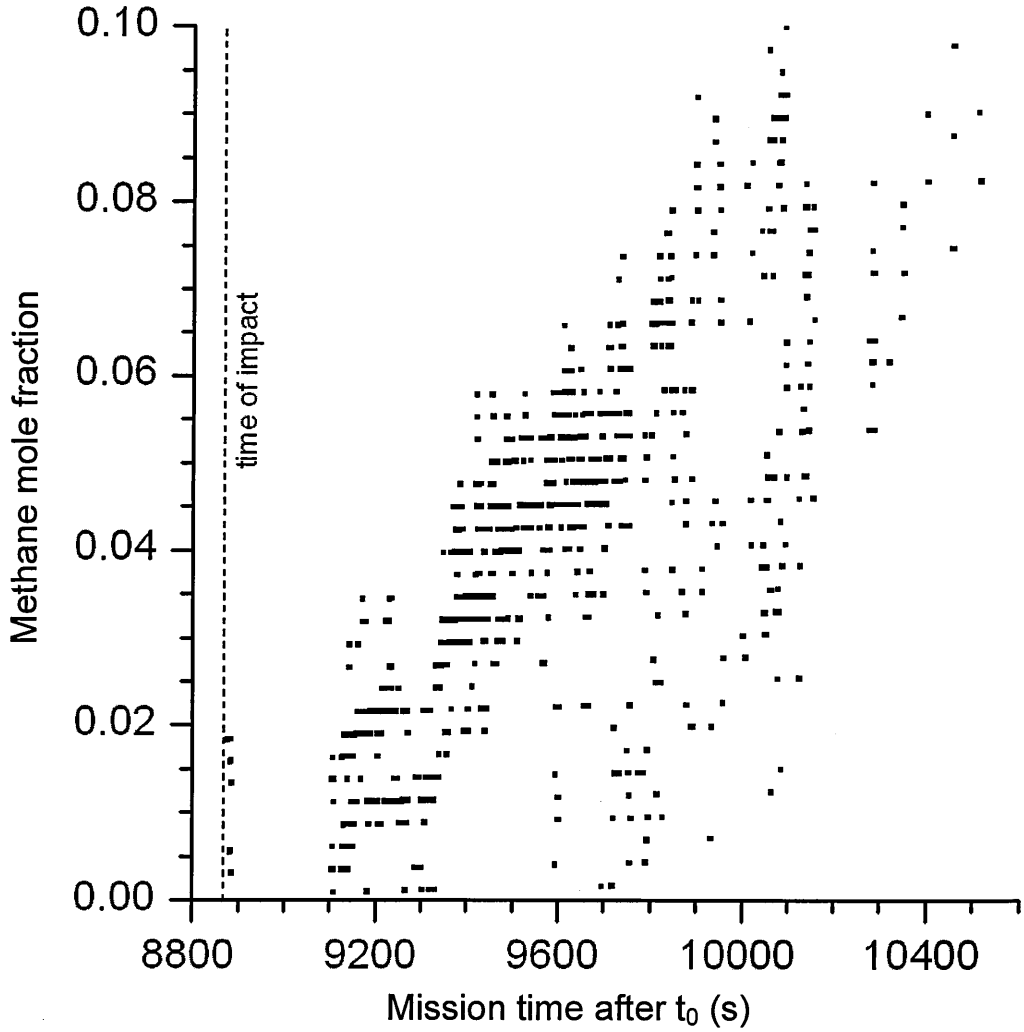

**Fig 5.5 Temperature change at API-V assuming constant methane abundance. As in Fig 5.4 a 6 μs offset has been applied as discussed in the text.**

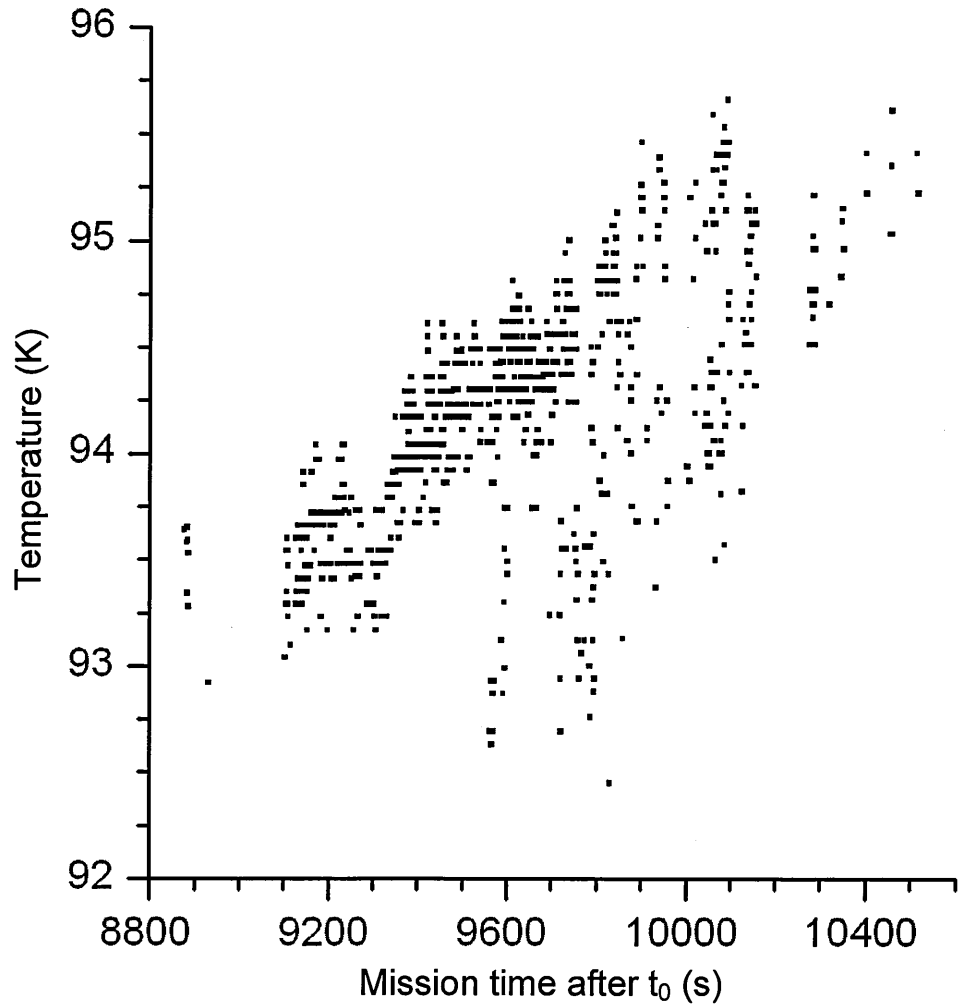


a way of investigating the change in sound speed after landing. Because of this, Fig 5.4 and Fig 5.5 should only be considered in a relative sense, i.e. showing changes with time and the absolute values of methane abundance and temperature derived may not be accurate.

The methane abundance derived in Fig 5.4 shows an increase in methane mole fraction of 0.08, which could be the result of evaporation from the surface. The volume of the Top Hat cavity is approximately 1.9 litres so if pure methane is being evaporated into this space, displacing some of the mixture that was already there and uniformly mixing with the remainder, then this increase in mole fraction would require 165 cc of methane vapour. This is equivalent to 1.3 cubic centimetres of liquid methane; spread across the ground at the opening of the Top Hat this would form a layer of around 0.14 mm thickness.

Fig 5.5 shows the temperature increase required to produce the equivalent change in the speed of sound assuming that the composition remained constant. The total temperature change required would be 2 K. For comparison, all other temperature sensors in the Top Hat showed an increase in temperature of at least 16 K; however, they are all much deeper within the cavity than API-V with the temperature increase shown by these sensors expected to be larger than that experienced by API-V.

**Fig 5.6 The 2.35 m $s^{-1}$ increase in sound speed seen after landing could be caused by any combination of temperature or methane mixing ratio increase shown by the black line below. The saturation levels, assuming a starting methane abundance as determined by either API-V (0.026) or GCMS (0.049), are shown. The methane abundance is unlikely to exceed the saturation level.**

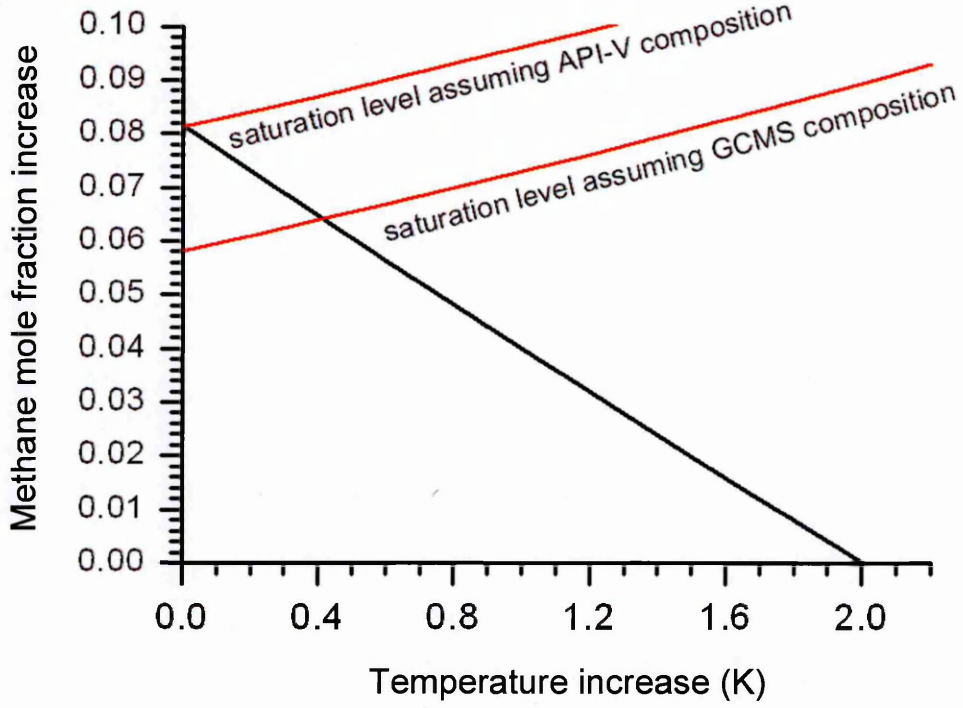


The total change of 2.35 m $s^{-1}$ over the time for which API-V functioned on the surface can be interpreted in the extreme cases as either a 2.0 K increase in temperature or a 0.081 increase in methane mixing ratio. The potential intermediate solutions are shown in Fig 5.6. Interestingly, if the methane mole fraction upon landing is taken from the results of this work, then if no temperature increase occurred the gas sampled by API-V may have just reached saturation point before API-V ceased functioning. Alternatively, if the initial

methane mole fraction is taken from the GCMS results then a temperature increase of at least ~0.4 K must have occurred.

# Chapter 6
# Conclusions

API-V has made measurements during the descent of Huygens through Titan's atmosphere from approximately 11 km altitude to the surface with an average spatial resolution of 6.5 m and after landing for approximately 26 minutes. Each measurement delivered the time of flight of a sound wave between the two sensor heads for the purpose of combining these with the separation distance of the sensors to determine the speed of sound.

Laboratory testing found that the flight spare sensors overestimated the time of flight of the sound wave and hence a calibration technique was devised which measured this offset as 3.71±0.04 μs. Unfortunately, as data was not collected before launch to allow calculation of this offset for the flight model sensors the value from the flight spares has had to be applied to the flight data.

The atmospheric data had a large scatter caused by the clock (which measured the time of flight of the sound wave) being triggered to stop on different peaks in the wave train. The distinctive patterns in the scatter created by missing some peaks allowed two different techniques to be used to extract an estimate of the true speed of sound. The first regarded each data point as an upper limit of time of flight and took a rolling minima of the data to estimate the true times of flight. The second technique estimated the probability that the time of flight was overestimated by specific amounts and used this probability density function to perform a Bayesian analysis of the data. Both methods matched well and showed that the speed of sound generally increased during the descent from 182.6 m $s^{-1}$ at 11 km to 194.0 m $s^{-1}$ at the surface. However, both methods relied on the assumption that the receiving sensor detected the first peak in the wave train at least one time in a hundred; there is no guarantee that the first peak was ever detected.

Three equations of state were considered for use in interpreting the measured speeds of sound in terms of composition. They were provided by Hagermann & Zarnecki (2006),

NIST, and GERG and were based on a Virial equation of state, a modified Benedict-Webb-Rubin equation of state and a Helmholtz free energy equation of state respectively. They each provided significantly different estimates; however, no experimental data for mixtures of methane and nitrogen under Titan-like conditions exist and hence, in order to decide which equation of state best represents such mixtures, higher temperature data by Estela-Uribe (2006) was used. The GERG-2004 equation of state gave the smallest residuals compared to the experimental data and hence was chosen for use in this work. The Huygens GCMS instrument revealed that the only major constituents in Titan's atmosphere are nitrogen and methane; hence, each speed of sound measurement was able to provide a unique solution for the composition in terms of methane mole fraction. The API-V data indicates a methane mole fraction at the Huygens landing site of 0.026±0.018. The mole fraction increases slightly up to 0.029 at ~5 km altitude then decreases to 0.012 at 7.2 km. These values for mole fraction of methane are lower than those seen by GCMS by approximately 0.02. This may have been caused by:

- API-V never detecting the first peaks in the transmitted wave train.
- Differences between the flight model and flight spare sensors used for calibration.
- Inaccuracies in the equation of state chosen for use.
- Unrecognised offsets in the GCMS measurements.

Of the possible systematic uncertainties in the API-V estimates, it seems that the inaccuracies in the equation of state used is the most likely to make a large contribution. Determining the adiabatic lapse rate and methane saturation level using the GERG-2004 equation of state indicates that methane in the atmosphere rising from the surface would begin to condense at 9.2 or 6.9 km for the API-V or GCMS methane abundance estimates respectively. Despite a slight upward air velocity measured by HASI (Teemu, et al. 2006), no clouds were reported in this range. Tokano (2006) predicted that the relative humidity was so high above 8 km that a cloud layer and methane drizzle should exist. Evaporation

of such drizzle, during its fall to the surface, may be the cause of the slight increase in methane mole fraction from the surface to ~5 km.

The surface data provided by API-V show that the speed of sound rose by ~2.35 m $s^{-1}$ over the 26 minutes after impact, at which point API-V ceased working, despite Huygens transmitting from the surface for a further 46 minutes. There was also a discontinuity between the measured speed of sound before and after impact. The cause of the discontinuity is unknown, but could potentially be caused by damage to the instrument; no temperature change was recorded that can explain the discontinuity and the sound speeds measured immediately after impact are not physically possible for mixtures of only nitrogen and methane at the relevant temperature and pressure. It is also difficult to interpret the long term change in terms of composition because, after impact, API-V is in a different thermal environment to the HASI TEM sensor which provided temperature data during descent. There is some evidence that, after landing, heat loss from Huygens caused evaporation of methane from the surface. If the temperature of API-V is assumed constant, then the data could be interpreted as a rise in methane mole fraction in the Top Hat of 0.08, equivalent to the evaporation of 1.3 cubic centimetres of liquid methane. Alternatively, on the assumption that the composition of the gas in the Top Hat remains constant, the change in sound speed can be explained by a rise of 2 K in temperature. The actual situation could, of course, be intermediate between these two extremes.

Interestingly, as time progressed on the surface, the scatter in API-V data changed and eventually the sensor ceased functioning around 26 minutes after impact. As Huygens was not level after impact (Tomasko, et al. 2005), the sensors were tilted relative to the horizontal. Hence, if the hollow produced by Huygens' impact slowly filled with liquid draining from the surrounding soil, one sensor could become submerged before the other causing cessation of function. The hollow filling with liquid could also be consistent with the reduction in ringing seen by the Acoustic Properties Instrument – Sonar after a time of 1270±50 s on the surface. Alternatively, as it has been shown that that the temperature at

API-V could only have risen by a maximum of 2 K, the sensor heads could have become an effective condensation trap if methane abundance rose in other warmer parts of the Top Hat. This condensation could have impeded effective function.

The API-V measurements with the analysis performed on the returned data, have shown that acoustic sensors possess the potential to provide incredibly useful information on planetary atmosphere. Further work, to both refine the technique and overcome some of the obstacles identified here, could allow a version of this sensor to excel in future planetary atmosphere probes.

# Chapter 7
# Future Work

The Huygens API-V instrument was the first instrument to measure the speed of sound in the atmosphere of a non-terrestrial body. As the first instrument of its kind developed for space applications, there have clearly been a number of lessons learnt during its development and in the analysis of the returned data. These will now allow greatly improved versions of the instrument to be constructed for use in the future.

Possibly the most significant problem encountered has been the fact that the clock measuring time of flight stopped on different peaks within the wave train. Part of this problem is that it is not known if the clock ever stopped on the first peak. Lessons can actually be learnt here from the field of seismology. Measuring time differences between similar signals is important in this field, for example when a tremor is received by multiple stations or if a tremor reflects from a boundary and is detected multiple times by the same station. To determine the time difference, a cross correlation, or autocorrelation is performed. The cross correlation of two real signals f(t) and g(t) with no imaginary component, offset by an estimated time $t_{est}$ is

$$f * g = \int_0^\infty f(t)g(t + t_{est})dt, \qquad \textbf{Eq 7.1}$$

Or, in the case of an autocorrelation, the same signal is compared to itself at later times, i.e. as in Eq 7.1 but with g(t)=f(t). It can easily be seen that when $t_{est}$ is the true time difference, the positive and negative parts of f(t) and g(t) are in phase, producing a maximum in the integration. Thus, by calculating the cross correlation over a range of values of $t_{est}$, the true time can easily be determined. In addition, if noise in the data causes a scatter in the measured time due to poor correlation of the signals, then to a zeroth approximation this scatter can be expected to be symmetric about the true value, allowing relatively simple analysis of the returned data.

A similar system can potentially be used for measuring atmospheric sound speed. Although the transmitted API-V signal is too dissimilar to the received signal to allow effective cross correlation, in some particularly favourable measurements in the laboratory, the transmitting sensor was able to detect the reflection of the wave train from the receiving sensor. In these cases, the directly detected and the reflected signal could be cross correlated. This technique has been used to measure times of flight accurately in nitrogen at room temperature – conditions where the equations of state are known to be reliable. Derivations of the speed of sound from these measurements gave agreement between theory and experiment to within 5 cm $s^{-1}$; one sixth the uncertainty attributed to Huygens API-V measurements. An appropriate setup for future instruments could use two reflectors at different distances from a sensor to reflect the sound waves either to a separate receiver, or more probably, back to the transmitter. An autocorrelation could then be performed to determine the time difference. Note that to determine sound speed in this case, only the difference in separation of the two reflectors is required, not the absolute distance between the reflectors and the transmitter. This may make it relatively simple to mount the reflectors in such a way that thermal contraction/expansion can be accurately taken into account.

Laboratory measurements of the speed of sound are generally performed by generating resonance across a cavity of a known size such as described by Trusler & Zarari (1992). It is, however, uncertain how flow through the resonance chamber may effect the measurements, hence, this technique may not be feasible for probes which are continually exposed to the atmosphere. Instead, a discrete atmospheric sample may have to be collected and sealed from the outside, before the speed of sound is measured and the sample released again. Of course discrete sampling would require additional moving parts such as valves which would introduce associated reliability issues as well as reducing temporal resolution.

The second major problem that has been highlighted by the analysis of the data was the lack of temperature data at the sensors' location. The speed of sound is highly dependant upon temperature and hence for conclusions to be made about composition of a gas, temperature should be known to a high accuracy very close to the sensor. Ideally the uncertainty should be ±0.1 K or better; however, this was beyond even the HASI TEM sensor with an accuracy of ±0.25 K. This problem could be overcome by measuring sound speed simultaneously in the atmosphere and also in a sealed chamber of known gas. If the sealed chamber was exposed to the atmosphere, it would approximately follow the same temperature profile, although with a lag due to thermal inertia. Providing that this difference in temperature is small the systematic uncertainties in temperature measurement can be reduced by comparing the two measurements; however, this technique does double the uncertainty in sound speed.

The final large uncertainty, which has affected the accuracy of the composition estimates, was introduced by the equation of state. Equations of state generally use empirical or semi-empirical functions fitted to available datasets. If no data are available for the compositions or conditions of interest, then the equation of state becomes an extrapolation of available data. This has been the case for this work and has meant that different equations of state can provide very different composition estimates based on identical API-V data. Future acoustic investigations should ensure that adequate laboratory simulations of the expected conditions are performed in order to ensure accurate compositions are derived.

The uncertainty in relating the speed of sound to composition is currently the biggest restriction on the use of the speed of sound in investigating planetary atmospheres. The experimental measurements required to overcome this problem can be challenging, but are certainly not impossible to carry out. Despite this problem a speed of sound sensor has a significant time resolution advantage over many other techniques for deriving atmospheric composition. API-V was forced to sacrifice its 1 s time resolution to produce useful accuracy. However a sensor built to an improved design may not have to make this

sacrifice and could also further improve the time resolution. The strength of this technique may in reality be created in combination with other measurement techniques, such as GCMS, where high accuracy low time resolution measurements are combined with the high time resolution speed of sound estimates to provide greatly increased detail in planetary atmosphere research.

The problem of the use of non-ideal equations of state for representing Titan's atmosphere has be investigated in this work, however little discussion has been produced in the scientific literature. Improving the understanding of the thermodynamics of the components of Titan's atmosphere is key to understanding Titan's climate. To this end the author intends to produce a summary and comparison of appropriate equations of state, along with the implications for Titan's atmosphere, for publication.

An acoustic sensor similar to API-V could have uses in a number of fields including space-based and terrestrial applications. On Earth, sound speed sensors can have uses in measuring the quality (i.e. methane content) of natural gas or measuring humidity in weather or industrial applications and patents have been filed for some of these applications (Kelner, et al. 2004). In other planetary environments, an acoustic sensor provides a method to investigate composition with a time resolution far surpassing any other instrument. In addition, improving the sensor further could allow development of a sonic anemometer for use in planetary atmospheres. Terrestrial versions of such instruments already exist which work in a manner very similar to API-V to measure the increase or decrease in time of flight of a sound wave broadcast in an upwind or downwind direction.

One particular application of an acoustic sensor is in the atmospheres of the giant planets. The molecular hydrogen that is contained within the atmospheres of such bodies can be found in two forms. In the ortho form the spins of the two atoms are aligned in the same direction, whereas in the para form they are aligned in the opposite direction. The equilibrium ratio for the two forms is dependant upon temperature and hence, if a pocket of

gas changes its conditions, the ratio of orthohydrogen to parahydrogen will change. The lifetime for the conversion is of the order days (Milenko, et al. 1997). This has two important implications. Because conversion from parahydrogen to orthohydrogen is exothermic, the change has implications for the energy budget and lapse rates of the planetary atmospheres. Also, because the conversion occurs with a large lifetime, if non-equilibrium ratios are found, some details can be determined about the previous state of the gas. Para-hydrogen and orthohydrogen have rather different values for their heat capacity at constant pressure. This then ensures that the ratio of specific heats is also different and hence, measurement of sound speed can be a diagnostic for the ratio of parahydrogen to orthohydrogen. Such an application has been considered by Lorenz (1999).

Acoustic attenuation is another property that may be measured by a sensor similar to that described above. Molecular fluids, and in particular mixtures, have vibrational energy states that can cause significant attenuation of ultrasonic sound waves at particular characteristic frequencies. The strength of the attenuation is related to concentration within a mixture and also to temperature. Hence the development of an 'acoustic spectrometer' may not be impossible.

# Chapter 8 Appendix

As part of this work a number of programs have been written to extract, analyse and log data. The three largest programs were to log calibration data in the lab, perform the optimisation algorithm and perform the Bayesian analysis. The programs were written in C++ and are composed of separate source and header files which have been compiled and linked using Microsoft Visual Studio 6.0. The object oriented nature of C++ and the separation of code into different files often means that the 'main' program is relatively short and simple, with most of the technical work existing in separate files for each object. In this appendix the code for each of the three programs mentioned above is provided. The main program is presented first followed by each header file and its associated source file.

## A.1 Logging Program

This program logged laboratory data during the calibration of API-V. The files presented here are

- the main program
- the scope header and source file which control the oscilloscope
- A date header and source file which format the date and time
- A nagspline header and source file which is a C++ encapsulation of the Numerical Algorithm Group's spline functions

### A.1.1 Main Program

```
//Program that reads temperature from the Lakeshore 331S Temp controller then at specified
// temperature intervals records the trace from a Tektronix TDS3034B Oscilloscope in a file
// with name in the format yyyy_mm_dd_hh_mm_ss__TTT.TT.csv and takes an image with a webcam
// of a pressure meter
//
// Phil Rosenberg,PSSRI, Open University. Jan 2006


// Header file for the Personal488 API Library
#include "iotieee.h"
// Standard I/O Headers
#include <stdio.h>
#include <fstream.h>
#include <time.h>
#include <conio.h>
#include <windows.h>
#include<vfw.h>
//Personally created header files
#include "scope.h" //includes functions to read from oscilloscope using GPIB
#include "date.h" //includes function to get current date and time in a string
#include "nagspline.h"//includes object encapsulation of spline functions
                      // from Numerical Algorithms Group

//define global variables

//array holding resistance callibration points
double rcal[]={6.147,7.09799,8.10613,9.15148,11.85913,14.50718,17.13019,19.70073,22.24518,24.73636,27.00029,27.0469,29.7859
9};
//array holding temperature calibration points after recallibration
double newtcal[]={69.87735227,79.8739406,89.81144424,99.75261771,124.9835943,149.8338987,174.9439718,200.0067744,225.154269
5,249.9850541,272.6419805,273.1109209,300.5508769};
//array holding temperature calibration points programmed into temperature controller
double oldtcal[]={70.115,80.137,90.097,100.058,125.328,150.202,175.322,200.381,225.511,250.311,272.928,273.396,300.772};


const int ncalpoints=13; // number of callibration points
spline calcurve; //a spline object to calculate temperature from resistance
```

```
fstream tout; // a filestream for use in outputting results



// functions
double getR(double T);
int OpenDevice(DevHandleT &dev, char* name);
double getT(DevHandleT dev);
void sample(DevHandleT dev, double T, HWND hWndC);
int saveWebcamImage(HWND hWndC, char*filename);



int main()
{
      //sort callibraton curve. This initialises the spline
      // with an interpolation of the callibration points
      calcurve.interpolate(ncalpoints,rcal,newtcal);


      int period=1000; //period of timeout for communication in ms
      char exit='n'; //exit program variable
      DevHandleT scope; //handle for oscilloscope
      DevHandleT tcon; //handle for temp controller
      int err; //error value

      //open oscilloscope and temp controller output error if connection cannot be made and return -1;
      if((err=OpenDevice(scope,"TDS3034b"))<0)
      {
            cout << "error connecting to TDS3034b" << endl;
            if (scope==-1) cout << "could not open device";
            else if(err==-1) cout << "no query response from device" << endl;
            else if(err==-2) cout << "*TST? query detected error" << endl;
            Close(scope);
            return -1;
      }
      if((err=OpenDevice(tcon,"TC331"))<0)
      {
            cout << "error connecting to TC331" << endl;
```

```
	if (tcon==-1) cout << "could not open device";
	else if(err==-1) cout << "no query response from device" << endl;
	else if(err==-2) cout << "*TST? query detected error" << endl;
	Close(scope);
	Close(tcon);
	return -1;
}

//open webcam capture window for imaging pressure sensor
// This uses build in functions from vfw.h
HWND hWndC = capCreateCaptureWindow ("Capture Window",0 ,0,0,160,120,0,0);
//connect to driver
if(capDriverConnect (hWndC, 0)==false)
{
	cout << "error connecting to webcam" << endl;
	return -1;
}



//request temperatures to sample at
double spacing,min,max;
cout << "Please enter the spacing between samples in K" << endl;
cin >> spacing;

cout << "Please enter the minimum temperature at which you wish to sample" << endl;
cin >> min;

cout << "Please enter the maximum temperature at which you wish to sample" << endl;
cin >> max;

//place all target temperatures in array.
int ntargets=int((max-min)/spacing)+1;
if ((max-min)/spacing-ntargets>0) ntargets+=1;
double *target=new double[ntargets];

cout << "samples will be taken at ";
for(int i=0; i<ntargets; i++)
{
	target[i]=min+double(i)*spacing;
	cout << target[i] << " ";
```

```
}
cout << "Kelvin" << endl;

//wait for user input to start sampling
cout << "press spacebar to start sampling or x to exit" << endl;
while(exit!=' ' && exit!='x')
{
      exit=getch();
}

double T, prevT, prev=-1;
//get one temperature reading before entering loop
T=getT(tcon);

//open file to save temperatures
tout.open("temperaturelog.csv", ios::out);
tout << "date,temperature_(K),scope_filename\n";

//begin sampling
cout << "sampling, press x to stop and exit" << endl;
Output(scope,"acquire:state on"); //ensure scope is sampling
while(exit!='x')
{
      Sleep(100); //wait 0.1s between taking samples
      //get temperature
      prevT=T;
      T=getT(tcon);
      //cout << T <<" K";
      if (T<0)
      {
            cout << "No response from TC331" << endl;
            break;
      }
      //see if we are at one of the requested temperatures
      for(i=0; i<ntargets; i++)
      {
            //enter this section if warming
            if(!(target[i]<prevT || target[i]>T))
            {
                  if(i!=prev)//if this temperature was not the previous one sampled
                  {
```

```
                        sample(scope,T, hWndC);//take a sample from scope
                        cout << T <<" K" << " sampled" << endl;
                        prev=i;//remember this temperature has just been sampled
                        break; //exit for loop
                  }
            }
            //enter this section if cooling
            else if(!(target[i]<T || target[i]>prevT))
            {
                  if(i!=prev)
                  {
                        sample(scope,T, hWndC);
                        cout << T <<" K" << " sampled" << endl;
                        prev=i;
                        break;
                  }
            }
      }
      //cout << endl;
      if(kbhit()) exit=getch();//check to see if user wants to exit
}


tout.close();
delete[] target; //free memory
//close devices
if(Close(scope)<0)
{
      cout <<"Unable to close TDS3034b" << endl;
      return -2;
}
if(Close(tcon)<0)
{
      cout <<"Unable to close TC311" << endl;
      return -2;
}
return 0;
}

//function to get a handle to a device on the GPIB bus
int OpenDevice(DevHandleT &dev, char*  name)
```

```
{
	dev=OpenName(name); //open device
	char szCharBuf[256]; //general use buffer
	Output(dev, "*TST?"); //perform self test
	if(Enter(dev,szCharBuf)<0)return -1; //if response is not received return -1
	if(atoi(szCharBuf)) return -2;//if self test failed (returned anything other than 0) return -2
	else return dev; //else return device handle
}

//function to get temperature from the temperature controller
double getT(DevHandleT dev)
{
	char szCharBuf[256]; //general use string

	//get temperature
	Output(dev, "KRDG?,A");
	if(Enter(dev, szCharBuf)<0) return -1;
	double T=atof(szCharBuf);
	double R=getR(T);

	//return temperature;
	return calcurve.evaluate(R);
}

//function to save data from all sources
void sample(DevHandleT dev, double T, HWND hWndC)
{
	//create filename in format yyyy_mm_dd_hh_mm_ss__TTT.TT.csv
	// y=year, m=month, d=day, h=hour, m=mins, s=secs, T=temperature
	char filename[128];
	char imgfilename[128];
	char szT[20];
	//convert temperature into a string
	gcvt(T,5,szT);
	//get date as a string to use in the filename
	getdate(filename);
	//output temperature and time to temperature log
	tout << filename << "," << T << ",";

	//replace colons with underscores for use in filename
	// and add temperature to end
```

```
	filename[4]='_';
	filename[7]='_';
	filename[10]='_';
	filename[13]='_';
	filename[16]='_';
	strcpy(imgfilename,filename);
	strcat(filename,"__");
	strcat(filename,szT);
	strcat(filename,".csv");
	tout << filename << "\n";

	//open file for storing oscilloscope curves
	fstream fout;
	fout.open(filename, ios::out);

	//store all oscilloscope curves
	storeallcurves(dev,fout);

	//close file
	fout.close();

	//save webcam image
	strcat(imgfilename,".bmp");
	saveWebcamImage(hWndC,imgfilename);
}

//function to convert from T output of temperature controller to
// resistance. This is to convert to different callibration curve
double getR(double T)
{
	if(T<oldtcal[0] || T>oldtcal[ncalpoints-1]) return 0;

	int pointlower=ncalpoints-2;
	while (T<oldtcal[pointlower])
	{
		if(pointlower==0) break;
		else pointlower--;
	}
	int pointhigher=pointlower+1;
	//cout << "ll=" << oldtcal[pointlower] << ", hl=" << oldtcal[pointhigher] << " => ";
```

```
	return (rcal[pointlower]-rcal[pointhigher])/(oldtcal[pointlower]-oldtcal[pointhigher])*(T-
oldtcal[pointlower])+rcal[pointlower];
}

//function to save image from webcam
int saveWebcamImage(HWND hWndC, char*filename)
{
	//grab one frame
	if(capGrabFrame (hWndC)==false) return -1;

	//save frame as bitmap
	if(capFileSaveDIB(hWndC,filename)==false) return -2;

	return 0;
}
```

### A.1.2 Scope

```
//Scope.h Header file for defining Oscilloscope logging functions using a GPIB bus. They are specific to the particular
GPIB logging card used
// Phil Rosenberg,PSSRI, Open University. Jan 2006


// Header file for the Personal488 API Library
#include "iotieee.h"
// Standard I/O Header
#include <stdio.h>
#include <fstream.h>
#include <time.h>
#include <conio.h>
#include <windows.h>

void storeallcurves (const DevHandleT dev, fstream fout);
long getcurve(const DevHandleT dev, const char* const channel, double* const array);



//Scope.cpp source file implementing functions defined in scope.h.

#include "scope.h"
```

```
void storeallcurves (const DevHandleT dev, fstream fout)
{
	//variables:
	// dev: a device handle for the scope
	// fout: a fstream to put the acquired data onto
	//Fstream pauses the acquiring of data by the scope and transfers the data from channels
	// 1, 2, 3 and 4 to the pc, storing them in columns with the time in a csv formatted file.
	// If the scope was acquiring data before the function call this is restarted.
	//
	//Phil Rosenberg Jan 2006



	char szCharBuf[256];//general purpose string

	//see if query return header is on. If so turn it off.
	char header[10];
	Output (dev, "Header?");
	Enter (dev,header);
	if(strchr(header,'1')!=NULL) strcpy(header, "1");
	Output(dev, "Header off");

	//check current acquire state and stop acquiring
	char state[3];
	Output(dev, "acquire:state?");
	Enter(dev,state);
	Output(dev, "acquire:state 0");

	//check current data source and change to source of last trigger
	char source[10];
	Output(dev, "data:source?");
	Enter(dev,source);
	char trigger[10];
	Output(dev,"trigger:a:edge:source?");
	Enter(dev, trigger);
	strcpy(szCharBuf, "data:source ");
	strcat(szCharBuf, trigger);
	Output(dev, szCharBuf);
```

```
//get x axis preamble data
//get x axis zero level
Output(dev, "wfmpre:xzero?");
Enter(dev, szCharBuf);
double xzero=atof(szCharBuf);
//get x axis increment
Output(dev,"wfmpre:xincr?");
Enter(dev, szCharBuf);
double xincr=atof(szCharBuf);

//allocate arrays for each channel
double ch1[10000];
double ch2[10000];
double ch3[10000];
double ch4[10000];

//use getcurve to load each channel
getcurve(dev, "ch1", ch1);
getcurve(dev, "ch2", ch2);
getcurve(dev, "ch3", ch3);
getcurve(dev, "ch4", ch4);

//return to old data source
strcpy(szCharBuf,"data:source ");
strcat(szCharBuf,source);
Output(dev, szCharBuf);

//return to old acquire state
strcpy(szCharBuf,"acquire:state ");
strcat(szCharBuf,state);
Output(dev, szCharBuf);

//return to old query return header state
strcpy(szCharBuf,"header ");
strcat(szCharBuf,header);
Output(dev, szCharBuf);

//output data to file
fout <<  "\"TIME\",\"CH1\",\"CH2\",\"CH3\",\"CH4\"\n";
for(long i=0; i<10000; i++)
{
```

```
            fout << xzero << "," << ch1[i] << "," << ch2[i] << "," << ch3[i] << "," << ch4[i] << "\n";
            xzero+=xincr;
      }


};

long getcurve(const DevHandleT dev, const char* const channel, double* const array)
{
      //variables:
      // dev: device handle to scope.
      // channel: string identifying channel to get data from, this can be "ch1", "ch2", "ch3",
      //    "ch4", "math", "math1" (same as math), "ref1", "ref2", "ref3" and "ref4". The function
      //  checks to ensure the requested channel is selected and returns -2 if not. This could
      //  be due to an invalid value for channel
      // array: an array in which the data is stored. This should have at least 10000 elements.
      //
      //The fuction takes data from one channel of the scope as specified by the device handle
      // dev and the string channel. This is stored in array. No x axis data is stored.
      //
      //Phil Rosenberg Jan 2006

      //see if query return header is on. If so turn it off.
      char header[10];
      Output (dev, "Header?");
      Enter (dev,header);
      if(strchr(header,'1')!=NULL) strcpy(header, "1");
      Output(dev, "Header off");

      //strings to store current settings
      char szCharBuf[256];
      char source[10];
      char encdg[10];
      char width[2];
      char start[6];
      char stop[6];


      //get current settings
      Output(dev, "data:source?");
      Enter(dev,source);
```

```
Output(dev, "data:encdg?");
Enter(dev,encdg);
Output(dev, "data:width?");
Enter(dev,width);
Output(dev, "data:start?");
Enter(dev,start);
Output(dev, "data:stop?");
Enter(dev,stop);

//then change them to required states
Output(dev, "data:encdg ascii");
Output(dev, "data:width 2");
Output(dev, "data:start 1");
Output(dev, "data:stop 10000");
//change to source given by channel string
strcpy(szCharBuf,"data:source ");
strcat(szCharBuf, channel);
Output(dev, szCharBuf);
//check source is correct
Output(dev, "data:source");
Enter(dev, szCharBuf);
if(strstr(szCharBuf,channel)==NULL) return -2; //if strstr() returns null the channel is
                                                // incorrect and has not changed

long retVal; //function return value
char dataBuf[100000]; //string to house the data transferred from scope
char delimiters[2]; //assign delimiters to divide the dataBuf string into each datapoint
delimiters[0]=',';
delimiters[1]='\0';
char* pnext; //pointer that will move along dataBuf to identify each successive datapoint
long i;



Output(dev, "curve?"); //request curve string
if((retVal=Enter(dev,dataBuf))<0) //if Enter() returns -1 curve off so fill array with zeros
{
      for(i=0; i<10000; i++) array[i]=0.0;
}
```

```
else //if Enter() returns >=0 curve is provided and placed in dataBuf
{

	//get preamble data
	//get y axis zero level
	Output(dev,"wfmpre:yzero?");
	Enter(dev, szCharBuf);
	double yzero=atof(szCharBuf);
	//get y axis multiplier
	Output(dev,"wfmpre:ymult?");
	Enter(dev, szCharBuf);
	double ymult=atof(szCharBuf);
	//get y axis offset
	Output(dev,"wfmpre:yoff?");
	Enter(dev, szCharBuf);
	double yoff=atof(szCharBuf);

	//use strtok from string.h to split the string into each datapoint
	pnext=strtok(dataBuf,delimiters);
	array[0]=double(atol(pnext)-yoff)*ymult+yzero;
	i=1;
	while((pnext=strtok(NULL,delimiters))!=NULL)
	{
		array[i]=(double(atol(pnext))-yoff)*ymult+yzero;//use preamble data to convert to voltage
		i++;
	}
}

//reset initial conditions
strcpy(szCharBuf,"data:encdg ");
strcat(szCharBuf,encdg);
Output(dev, szCharBuf);
strcpy(szCharBuf,"data:start ");
strcat(szCharBuf,start);
Output(dev, szCharBuf);
strcpy(szCharBuf,"data:stop ");
strcat(szCharBuf,stop);
Output(dev, szCharBuf);
strcpy(szCharBuf,"data:width ");
strcat(szCharBuf,width);
Output(dev, szCharBuf);
```

```
        strcpy(szCharBuf,"data:source ");
        strcat(szCharBuf,source);
        Output(dev, szCharBuf);
        strcpy(szCharBuf,"header ");
        strcat(szCharBuf,header);
        Output(dev, szCharBuf);


        return retVal;
}
```

### A.1.3 Date

```
//date.h Header file defining function for getting the current date and applying specific formatting

#include <time.h>
#include <string.h>
void getdate(char *szDate, char datesep='/', char timesep=':', char dtsep=' ');


//date.cpp source file for implementing function in date.h
#include"date.h"
void getdate(char *szDate, char datesep, char timesep, char dtsep)
{
        //puts current time and date in string szDate in format yyyy_mm_dd_hh_mm_ss. szDate must
        // be at least 19 characters long;
        char *szNow=new char[50];
        long now;
        long* pnow=&now;
        now=time(0);
        szNow=asctime(localtime(pnow));

        //get year
        for(int i=0; i<4; i++) szDate[i]=szNow[i+20];
        szDate[4]=datesep;

        //get month
        if(strstr(szNow,"Jan"))
        {
```

```
        szDate[5]='0';
        szDate[6]='1';
}
else if(strstr(szNow,"Feb"))
{
        szDate[5]='0';
        szDate[6]='2';
}
else if(strstr(szNow,"Mar"))
{
        szDate[5]='0';
        szDate[6]='3';
}
else if(strstr(szNow,"Apr"))
{
        szDate[5]='0';
        szDate[6]='4';
}
else if(strstr(szNow,"May"))
{
        szDate[5]='0';
        szDate[6]='5';
}
else if(strstr(szNow,"Jun"))
{
        szDate[5]='0';
        szDate[6]='6';
}
else if(strstr(szNow,"Jul"))
{
        szDate[5]='0';
        szDate[6]='7';
}
else if(strstr(szNow,"Aug"))
{
        szDate[5]='0';
        szDate[6]='8';
}
else if(strstr(szNow,"Sep"))
{
        szDate[5]='0';
```

```
            szDate[6]='9';
        }
        else if(strstr(szNow,"Oct"))
        {
            szDate[5]='1';
            szDate[6]='0';
        }
        else if(strstr(szNow,"Nov"))
        {
            szDate[5]='1';
            szDate[6]='1';
        }
        else if(strstr(szNow,"Dec"))
        {
            szDate[5]='1';
            szDate[6]='2';
        }
        szDate[7]=datesep;

        //get day and time
        for (i=8; i<19; i++)
        {
            szDate[i]=szNow[i];
        }
        //replace other dividers with _
        szDate[10]=dtsep;
        szDate[13]=timesep;
        szDate[16]=timesep;

        //put null character at end;
        szDate[19]='\0';
}
```

### A.1.4 Nagspline

```
//nagspline.h a c++ encapsulation of the NAG spline functions

#ifndef NAGSPLINE_H
#define NAGSPLINE_H
```

```
#include<nag.h>
#include<nage01.h>
#include<nage02.h>
#include<nag_stdlib.h>


class spline
{
public:
      spline();
      ~spline();
      int interpolate(long n, double *x,double *y);
      int fitknots(long npoints, double *x, double *y, double *w, int ninteriorknots, double *startingknots=NULL);
      void setprinterror(bool printerror);
      double evaluate(double x, int *errcode=NULL);
      int evaluate(double x, double *y);
      int fit(bool warmstart, long npoints, double *x, double *y, double *w, double S);

private:
      Nag_Spline curve;
      bool lamdaallocated;
      bool callocated;
      void freemem();
      double sse;
      NagError err;
      Nag_Comm warmstartinf;
      bool warmallocated;
      double getSSE() {return sse;};
};

#endif


//nagspline.cpp the source code implementing the functions in nagspline.h

#include"nagspline.h"

//constructor
spline::spline()
{
```

```
        lamdaallocated=false;
        callocated=false;
        sse=0;
        INIT_FAIL(err);
        warmallocated=false;
};

//destructor
spline::~spline()
{
        freemem();
};

//function to free all dynamically allocated memory
void spline::freemem()
{
        if(lamdaallocated)NAG_FREE(curve.lamda);
        if(callocated) NAG_FREE(curve.c);
        lamdaallocated=false;
        callocated=false;
        if(warmallocated)
        {
                NAG_FREE(warmstartinf.nag_w);
                NAG_FREE(warmstartinf.nag_iw);
        }
        warmallocated=false;
};

//sets the spline to interpolate between a number of x,y data points
int spline::interpolate(long npoints, double *x,double *y)
{
        freemem();
        nag_1d_spline_interpolant(npoints,x,y,&curve,&err);
        if(err.code=NE_NOERROR)
        {
                lamdaallocated=true;
                callocated=true;
        }
        sse=0;
        return err.code;
};
```

```
// a function that will give the spline a specified number of knots at specified values of y then
// fit the spline to given x,y data with weights, w, specified for each point
int spline::fitknots(long npoints, double *x, double *y, double *w, int ninteriorknots, double *interiorknots)
{
	freemem();
	curve.n=ninteriorknots+8;
	curve.lamda=NAG_ALLOC (curve.n, double);
	lamdaallocated=true;
	if(interiorknots==NULL)
	{
		double interval=(x[npoints-1]-x[0])/(ninteriorknots+1);
		double nextknot=x[0];
		for(int i=0; i<ninteriorknots; i++)
		{
			nextknot+=interval;
			curve.lamda[i+4]=nextknot;
		}

	}
	else
	{
		for(int i=0; i<ninteriorknots; i++) curve.lamda[i+4]=interiorknots[i];
	}

	e02bac(npoints, x, y, w, &sse, &curve, &err);
	if(err.code=NE_NOERROR)
	{
		callocated=true;
	}
	return err.code;
};

void spline::setprinterror(bool printerror)
{
	if(printerror)err.print=TRUE;
	else err.print=FALSE;
};

//a function to return the y value of the spline at a given value of x
//if an error occurs it is placed in errcode
```

```
double spline::evaluate(double x, int *errcode)
{
      double answer=0;
      nag_1d_spline_evaluate(x,&answer,&curve,&err);
      if(errcode!=NULL) *errcode=err.code;
      return answer;
};

//a function to return the error code of an evaluation. The y value of the spline at the given
//value of x is placed in *y.
int spline::evaluate(double x, double *y)
{
      double answer=0;
      nag_1d_spline_evaluate(x,&answer,&curve,&err);
      *y=answer;
      return err.code;
};

// A function that uses a smoothing factor S to produce a spline that fits to weighted x,y data
int spline::fit(bool warmstart, long npoints, double *x, double *y, double *w, double S)
{
      Nag_Start warmorcold;
      if (warmstart) warmorcold=Nag_Warm;
      else
      {
            warmorcold=Nag_Cold;
            freemem();
      }
      nag_1d_spline_fit(warmorcold,npoints,x,y,w,S,npoints+4,&sse,&warmstartinf,&curve,&err);
      if(err.code==NE_NOERROR)
      {
            lamdaallocated=true;
            callocated=true;
            warmallocated=true;
      }
      return err.code;
};
```

## A.2 Numerical Optimisation Program

This program performed simulated annealing upon the API-V data.

### A.2.1 Main Program

```
//include standard header
#include <fstream.h>
//include numerical algorith group headers for random number generation
#include <nag.h>
#include <nagg05.h>
#include <math.h>
//include specifically defined headers
#include "annealing.h"

int main()
{
      int i;
      float *D;
      int n=608;//1204;
      D= new float[n];
      double alpha=0.999999;
      double start_T=2000;
      int output_every=1000;
      int nearest_neighbours=0;



      fstream fout;
      /*
      fout.open("start.csv", ios::out);
      double width=0.1;
      for(i=0; i<n; i++)
      {
            D[i]=float(floor(g05ddc(0.0,width)*4.0)/4.0)+float(rand()%16);//gaussian spread with fwhm=0.3+random integer
from 0-15
            fout << D[i] << endl;
```

```
	}

	fout.close();
	*/


	fstream fin;
	fin.open("input.tab", ios::in);
	for (i=0; i<n; i++)
	{
		fin >> D[i];
	}
	fin.close();

	cout << "Enter the number of nearest neighbors to take into account" << endl;
	cin >> nearest_neighbours;

	while (nearest_neighbours<1)
	{
		cout<<"The number of nearest neighbours must be at least 1,\n please try again";
		cin >> nearest_neighbours;
	}
	metal sos(n, D, start_T,5);
	sos.warmup(1000);
	cout << "The expected time for completion of the simulation is at least " << sos.expectedtime(alpha) << " seconds" <<
endl;
	fout.open("track.csv",ios::out);


	sos.anneal(alpha,20000000,fout,output_every);
	fout.close();
	cout << "\n\ndone\n\n" << endl;
	//fstream fout;
	fout.open("final.csv", ios::out);
	for (i=0; i<n; i++) fout << D[i] << "," << endl;

	cout << "\ncompleted with " << nearest_neighbours << " nearest neighbours" << endl;

	return 0;
}
```

## A.2.2 Annealing

```
//Annealing.h to define the functions used in the annealing program
#include <stdlib.h>
#include <math.h>
#include <fstream.h>
#include <time.h>
class metal
{
private:
      float *_atom;              //array to hold the initial data
      float *_original;             //copy of original data
      int _n;                    //number of elements in _atom
      float *_best;              //best solution so far
      float _best_energy;           //energy of the best solution so far
      float _energy;             //energy of the current solution
      double _temperature;        //current temperature
      const int _nnc;                  //number of nearest neighbours considered
      double _time_per_iter;        //time in seconds per itteration in warmup

      //function to calculate the energy of two data points
      float energy(float atom1, float atom2);

      //returns a random number in the range 0 to n_ints-1 inclusive
      int randint(int n_ints)
      {
            return rand()%n_ints;
      }

      //function to return a random float in the range 0-1 excluding 0 but
      //including 1.
      double randdouble()
      {
            return double(rand()+1)/double(RAND_MAX+1);
      }
      void acceptChange(float energy_change);
      void makeBest();

      //function to seed the random number generator
      void seedrandomnumbers()
```

```
        {
                //srand ( time(NULL) );
        }

public:
        //constructor
        metal(int n_atoms, float *atom, double start_T, int n_neighbours=1);
        //destructor
        ~metal();
        //function to anneal the data. alpha is the factor by which the
        //temperature descreases each itteration. best is a pointer to an
        //array in which the best solution will be placed. If best is ommitted
        // then the best solution is written over the oriinal data. If best is
        //included then the original data is replaced by the final solution
        //considered. fout is an output stream that should already have been
        //opened before the function is called. output defines the frequency
        //with which data is outputted on fout. ie if output is 100, every 100th
        //itteration will be written to file.
        void anneal(double alpha, long n_itterations, fstream fout, int output, float *best=0);
        double expectedtime(double alpha)
        {
                return _time_per_iter*(-log(float(RAND_MAX)*_temperature)/log(alpha));
        }
        void warmup(int n_iterations);
};

//Annealing.cpp to implement the functions in annealing.h
#include "annealing.h"

//constuctor
metal::metal(int n_atoms, float *atom, double start_T, int n_neighbours)
: _nnc (n_neighbours)
{
        int i,j;
        //set all internal variables
        _n=n_atoms;
        _atom=atom;
        _temperature=start_T;
        _best=new float[_n];
        //_N=new int[_n];
        for (i=0; i<_n; i++)
```

```
        {
                _best[i]=_atom[i];
                //_N[i]=0;
        }
        _original=new float[_n];
        for(i=0; i<_n; i++) _original[i]=_atom[i];


        //seed the random number generator
        seedrandomnumbers();

        //determine starting energy of the system
        _energy=0.0;


        for(i=0; i<_n-_nnc; i++)
        {
                for(j=i+1; j<i+1+_nnc; j++)
                {
                        _energy+=energy(_atom[i],_atom[j]);
                }
        }
        for(i=_n-_nnc; i<_n-1; i++)
        {
                for(j=i+1; j<_n; j++)
                {
                        _energy+=energy(_atom[i],_atom[j]);
                }
        }
        _best_energy=_energy;
        cout <<"starting energy is " <<_energy << endl;;


        _time_per_iter=0.0;
}

metal::~metal()
{
        delete[] _best;
}
```

```
//warms up or'melts' the metal for subsequent annealing
void metal::warmup(int n_iterations)
{
      cout << "warming up" << endl;
      fstream fout;
      fout.open("warmup.csv", ios::out);
      float *best_temp= new float[_n];

      //record time taken for warmup
      time_t start;
      time_t finish;
      start=time(0);
      anneal(1,n_iterations, fout,100, best_temp);
      finish=time(0);
      _time_per_iter=difftime(finish,start)/n_iterations;
      delete[] best_temp;
      fout.close();
      cout << "system warmed up" << endl;
}

//perform annealing
void metal::anneal(double alpha, long n_itterations, fstream fout, int output, float *best)
{
      fout << "iterations,n_changes,energy,temperature,\n";
      int i,j,k;
      //create an array to track which atoms have been selected during
      //each itteration.
      int *unselected=new int[_n];
      for(i=0; i<_n; i++) unselected[i]=i;
      int selected;
      int r;
      int temp;
      float new_local_energy;
      float old_local_energy;
      float delta_energy;
      float direction=1.0;
      int n_alterations;
      int n_no_change=0;
      int n_energy_changes=0;
      int n_energy_changes_all=0;
```

```
for (i=0; i<n_itterations; ++i)
{
      n_alterations=0;
      n_energy_changes=0;

      //alter each atom in a random order
      for (j=0; j<_n; ++j)
      {

            //select an unselected atom. The indeces of the
            //unselected atoms are found in the first (_n-j)
            //elements of unselected[]
            r=randint(_n-j);
            selected=unselected[r];

            //move the selected number out of the range where numbers
            //are selected;
            temp=unselected[r];
            unselected[r]=unselected[_n-j-1];
            unselected[_n-j-1]=temp;

            //determine the direction of the change.
            if(randint(2)) direction=1.0;
            else direction=-1;
            old_local_energy=0;
            new_local_energy=0;

            //determine the energy change
            if(selected<_nnc)
            {
                  for(k=0; k<selected+1+_nnc; ++k)
                  {
                        old_local_energy+=energy(_atom[selected],_atom[k]);
                  }
                  _atom[selected]+=direction;
                  for(k=0; k<selected+1+_nnc; ++k)
                  {
                        new_local_energy+=energy(_atom[selected],_atom[k]);
                  }
```

```
        delta_energy=new_local_energy-old_local_energy;
}

else if (selected>_n-_nnc-1)
{
        for(k=selected-_nnc; k<_n; ++k)
        {
                old_local_energy+=energy(_atom[selected],_atom[k]);
        }
        _atom[selected]+=direction;
        for(k=selected-_nnc; k<_n; ++k)
        {
                new_local_energy+=energy(_atom[selected],_atom[k]);
        }
        delta_energy=new_local_energy-old_local_energy;
}
else
{
        for(k=selected-_nnc; k<selected+1+_nnc; ++k)
        {
                old_local_energy+=energy(_atom[selected],_atom[k]);
        }
        _atom[selected]+=direction;
        for(k=selected-_nnc; k<selected+1+_nnc; ++k)
        {
                new_local_energy+=energy(_atom[selected],_atom[k]);
        }
        delta_energy=new_local_energy-old_local_energy;
}


//determine whether to reject the change
if(_atom[selected]>_original[selected])
{
        //reject the change and return the selected atom to it's previous state
        _atom[selected]-=direction;
}
if (delta_energy>0.0)
{
        if (randdouble()>exp(-delta_energy/_temperature))
```

```
            {
                  //reject the change and return the selected atom to it's previous state
                  _atom[selected]-=direction;
            }
            else
            {
                  //accept the change, calculte the new energy and keep track of n_alterations
                  acceptChange(delta_energy);
                  ++n_alterations;
                  ++n_energy_changes;
            }
      }
      else
      {
            //accept the change, calculte the new energy and keep track of n_alterations
            acceptChange(delta_energy);
            ++n_alterations;
            if(delta_energy<0.0) ++n_energy_changes;
      }


}

//reduce _temperature by a factor alpha
_temperature*=alpha;


//output data for every 100th iteration   to file
if(!(i%output))
{
      fout << i << "," << n_alterations << "," << _energy << "," << _temperature << "\n";

}

//if the energy of the metal has not changed for 1000 iterations then stop
if(n_energy_changes==0) n_no_change+=1;
else n_no_change=0;


if (n_no_change>10000)
```

```
            {
                  fout << i << "," << n_alterations << "," << _energy << "," << _temperature << "\n";
                  cout << "no changes in 1000 iterations" << endl;
                  break;

            }

            if(!(i%output))
            {
                  cout << i << " " << n_alterations <<  endl;
            }
      }

      if (alpha<1.0) cout << "annealing complete" << endl;


      //free memory used
      delete[] unselected;


      //write the best solution to pointer provided or if no pointer is
      //provided overwrite the original data
      if (best!=0)
      {
            for(i=0; i<_n; i++) best[i]=_best[i];
      }
      else for(i=0; i<_n; i++) _atom[i]=_best[i];



}

//determine energy contribution from two atoms
inline float metal::energy(float atom1, float atom2)
{
      return (atom1-atom2)*(atom1-atom2);
}

//decide whether to accept a change
inline void metal::acceptChange(float energy_change)
{
```

```
	_energy+=energy_change;
	if(_energy<_best_energy) makeBest();
	//else if(_energy==_best_energy) cout << "change matched best energy" << endl;
}

//set the current solution to the best so far
void metal::makeBest()
{
	_best_energy=_energy;
	for(int i=0; i<_n; ++i)
	{
		_best[i]=_atom[i];
	}
}
```

## A.3 Bayesian Analysis

This program performs Bayesian analysis on the API-V data. The outputs are a bitmap with pixel coloured to represent the probability of a solution. Black is highest probability, white is zero probability. The bitmap can then be incorporated into a plot. An array is also produced outputting the probability for each pixel, normalised so that the highest probability on a row is equal to unity.

### A.3.1 Main Program

```
//This code uses velocities provided by GERG2004 as a basis for hypotheses for bayesian analysis
// based on deltat=difference between the hypothesised or measured time of flight and that
// predicted by GERG2004 for a reference atmosphere of specified composition.
//
//For the bayesian plot the axes are composition(x) from 0-10% methane and altitude(y) from
// 0-11 km. For each pixel on this plot the altitude is used to determine temperature and pressure
// which is then combined with the hypothesis methane abundance to determine a hypothesis  speed
// of sound. These are stored in tab separated text file "gerg guesses.txt". the temperature is
```

```
// also used to determine the thermal contraction of the Top Hat and the separation of the sensors.
// These values are stored in "separation.txt". The values of time of flight for the reference
// atmosphere are stored in "gerg reference.txt" and the deltat data from huygens is stored in
// "data.txt"
//
//The data from these files is read into the program and the time of flight and deltat hypothesis
// is calculated for each pixel. The Bayesian analysis is then performed for each pixel using the
// apropriate group of 200 huygens data points.
//
//For each row of pixels (ie altitude) the pixels are assigned a greyscale value from 0 to 255 in
// a linear fishion with the highest probability pixel assigned 0 (black) and zero probability
// assigned 255 (white)
//



//headers
#include"bitmap.h"
#include<vector>
#include<iostream>
#include<math.h>

using namespace std;

// function declarations
double countspdf(double x, double given);
double prior (double x);

enum plot_type{methane,speed,tof,deltat};

int main()
{

      int i,j,k;
      plot_type plot=speed;

      const int xpixels=673;//number of pixels in x direction on plots
      const int ypixels=662;//number of pixels in y direction on plots
      const double altrange=11.2;//altitude range on plots in km
      const double altitudeperpixel=altrange/(double)ypixels;
      const int n=1743; //number of huygens data points
```

```
const int groupsize=200; //resolution of bayesian analisis in number of points
const int ngroups=n/groupsize+1;
const int lastgroupsize=n%groupsize;
vector < vector <double > > hypothesis; //2d vector with one element per pixel
vector <double> separation; //vector holding separation for each pixel in y direction
vector <double> gerg_reference; //reference sound speed for each pixel in y direction
vector <double> deltatdata; //API-V deltat data
vector <double> altitude; //Altitude of each API-V measurement
double temp; //a temporary variable for use when reading in data



//read in data from files

cout << "reading data" << endl;

fstream sin;
sin.open("separation.txt", ios::in);
if(!sin.is_open())
{
      cout << "cannot open separation.txt" << endl;
      return 0;
}
for(i=0; i<ypixels; i++)
{
      sin >> temp;
      separation.push_back(temp);
}
sin.close();

fstream rin;
rin.open("gerg reference.txt", ios::in);
if(!rin.is_open())
{
      cout << "cannot open gerg reference.txt" << endl;
      return 0;
}
for(i=0; i<ypixels; i++)
{
      rin >> temp;
```

```
		gerg_reference.push_back(temp);
	}
	rin.close();

	fstream din;
	din.open("data.txt", ios::in);
	if(!din.is_open())
	{
		cout << "cannot open data.txt" << endl;
		return 0;
	}
	for(i=0; i<n; i++)
	{
		din >> temp;
		altitude.push_back(temp);
		din >> temp;
		deltatdata.push_back(temp);
	}
	din.close();


	//depending on the plot being created the hypothesis array must
	//be constructed slightly differently

	if(plot==methane)
	{
		//for the methane plot the speed of sound data from GERG2004 equation of
		// state for each pixel must be read in from a file.
		fstream gin;
		gin.open("gerg guesses.txt", ios::in);
		if(!gin.is_open())
		{
			cout << "cannot open gerg guesses.txt" << endl;
			return 0;
		}
		for(i=0; i<ypixels; i++)
		{
			vector<double> hypothesis_row;
			for(j=0; j<xpixels; j++)
			{
				gin >> temp;
```

```
                        hypothesis_row.push_back(temp);
                }
                hypothesis.push_back(hypothesis_row);
        }
        gin.close();

        //convert hypothesis speed of sound data into deltat hypotheses. Huygens internal units of 1 count
        // equals 0.25 microseconds are used
        for(i=0; i<ypixels; i++)
        {
                for(j=0; j<xpixels; j++)
                {
                        hypothesis[i][j]=separation[i]*4e6/hypothesis[i][j]-gerg_reference[i];
                }
        }
}

else if (plot==speed)
{
        //for the speed of sound plot the value for speed of sound
        // at each pixelel can be determined by the pixel position
        // and the deltat hypothesis calculated from this
        double minspeed=183;
        double maxspeed=195;
        double speedperpixel=(maxspeed-minspeed)/(double)xpixels;
        for(i=0; i<ypixels; i++)
        {
                vector <double> hypothesis_row;
                for(j=0; j<xpixels; j++)hypothesis_row.push_back(separation[i]*4e6/(minspeed+(double)j*speedperpixel)-
gerg_reference[i]);
                hypothesis.push_back(hypothesis_row);
        }
}

else if (plot==tof)
{
        //for the time of flight plot the time of flight for each
        // pixel is determined by its position and the deltat
        // hypothesis is calculated from this
        double mintof=660e-6;
        double maxtof=720e-6;
```

```
	double tofperpixel=(maxtof-mintof)/(double)xpixels;
	for(i=0; i<ypixels; i++)
	{
		vector <double> hypothesis_row;
		for(j=0; j<xpixels; j++)hypothesis_row.push_back(4e6*(mintof+(double)j*tofperpixel)-gerg_reference[i]);
		hypothesis.push_back(hypothesis_row);
	}
}

else if (plot==deltat)
{
	//for a plot of deltat, the value of deltat hypothesis
	// can be determined soley from the pixel position so
	// only conversion to huygens internal units is needed.
	double mindeltat=-20e-6;
	double maxdeltat=100e-6;
	double deltatperpixel=(maxdeltat-mindeltat)/(double)xpixels;

	vector <double> hypothesis_row;
	for(j=0; j<xpixels; j++)hypothesis_row.push_back(4e6*(mindeltat+(double)j*deltatperpixel));

	for(i=0; i<ypixels; i++) hypothesis.push_back(hypothesis_row);
}
else return 0;


//perform the bayesian analysis, placing the results in a 2d vector called prob.
cout << "performing baysian analysis" << endl;
vector < vector<double> > prob;
for(i=0; i<ypixels; i++)
{
	cout << "row " << i << "\b\b\b\b\b\b\b\b";
	cout.flush();
	vector <double> probrow;

	//determine which altitude band the pixels fit into;
	double alt=i*altitudeperpixel;
	int group=0;
	while(alt>altitude[(group+1)*groupsize-1])
	{
		group++;
```

```
            if(group==ngroups-1) break;
        }

        //if the pixels are closer to the top point in the previos band than the bottom point
        // of the band they have been assigned then use the earlier group of points
        if(group>0)
        {
            if(alt<(altitude[group*groupsize]+altitude[group*groupsize-1])/2.0) group--;
        }

        //perform the bayesian analysis
        int npoints=groupsize;
        if(group==ngroups-1) npoints=lastgroupsize;

        for(j=0; j<xpixels; j++)
        {
            temp=prior(hypothesis[i][j]);
            for(k=0; k<npoints; k++)
            {
                temp*=countspdf(deltatdata[group*groupsize+k],hypothesis[i][j]);
            }
            //cout << endl;
            probrow.push_back(temp);
        }
        prob.push_back(probrow);
}



//normalise each row so that the max probability=1.0
cout << "normalising" << endl;
for (i=0; i<ypixels;i++)
{
        double max=0.0;
        for(int j=0; j<xpixels; j++)
        {
            if(prob[i][j]>max) max=prob[i][j];

        }
        for(j=0; j<xpixels; j++)
```

```
		{
			prob[i][j]/=max;
		}
	}


	//create a bitmap representing the probabilities. On each row the most
	// likely delta_t is black and white represents zero probability.
	cout << "generating bitmap" << endl;
	vector< vector <RGBQUAD> > rgb;
	i=0;
	for(i=0; i<ypixels; i++)
	{
		vector< RGBQUAD > rgbrow;
		RGBQUAD rgbpoint;
		//cout << i<< endl;
		//cout << speedprob.at(i).size() << endl;
		for(int j=0; j<xpixels; j++)
		{
			double brightness=255.0-(prob[i][j]*255.0);
			if (brightness <0) brightness=0;
			rgbpoint.rgbBlue=(unsigned char)brightness;
			rgbpoint.rgbRed=(unsigned char)brightness;
			rgbpoint.rgbGreen=(unsigned char)brightness;
			rgbrow.push_back(rgbpoint);
		}
		rgb.push_back(rgbrow);

	}
	bitmap24 hist3d(rgb,1000,1000);
	hist3d.save("hist3d.bmp");

	cout << "completed" << endl;



	return 0;
}
```

```
//prior=1.0, i.e. no prior knowledge
double inline prior (double x)
{
	return 1.0;
}


//The probability density function (pdf) for the measurements. Given is the guess, x
// is the data. The function returns the probability of getting the data given the
// guess is true.
double countspdf(double x, double given)
{
	//The pdf is the sum of npeaks gaussian curves each with a FWHM=2*sqrt(2*ln(2))*width
	//Note the function uses huygens internal units or counts. 1 count = 0.25 microseconds
	int npeaks=13;
	double width=1.5; //FWHM=3.5 counts
	double separation=4.0; //wavelength of sound wave
	double result=0.0;
	for (int i=0; i<npeaks; i++)
	{
		result+=exp((x-given-i*separation)*(x-given-i*separation)/(-2.0*width*width));
	}

	//to accomodate reflections give a finite probability that a signal
	// can occurr after the npeaks
	double level=0.1;
	if(x-given>(npeaks-1)*separation)
	{
		if(result<level) result=level;
	}
	return result;

}
```

### A.3.2 Bitmap

```
//bitmap.h header to define functions to output bitmap file
#include <windows.h>
#include <wingdi.h>
#include<fstream>
#include<vector>
using namespace std;

class bitmap24
{
private:
      BITMAPFILEHEADER bfh;
      BITMAPINFOHEADER bih;
      vector <vector <RGBQUAD> > q;
public:
      bitmap24(const vector <vector <RGBQUAD> > &rgb, LONG xpixelspermetre, LONG ypixelspermetre);
      ~bitmap24(){};
      //setpixel(int x,int y, unsigned short red,unsigned short green,unsigned short blue);
      void save(const char *filename);
};



//bitmap.cpp source file to initialise functions in bitmap.h
#include"bitmap.h"
#include<iostream>
using namespace std;

//requires a 2d vector of rgbquads indexed from bottom left corner of bitmap in form rgb[y][x]
bitmap24::bitmap24(const vector <vector <RGBQUAD> > &rgb, LONG xpixelspermetre, LONG ypixelspermetre)
{
      bih.biSize=sizeof(bih);
      bih.biHeight=rgb.size();
      bih.biWidth=0;
      for(LONG k=0; k<bih.biHeight; k++)
      {
            if(rgb.at(0).size()>bih.biWidth)bih.biWidth=rgb.at(0).size();
      }
      bih.biPlanes=1;
```

```
	bih.biBitCount=24;
	bih.biCompression=BI_RGB;
	bih.biSizeImage=bih.biWidth*bih.biHeight*24;
	bih.biXPelsPerMeter=xpixelspermetre;
	bih.biYPelsPerMeter=ypixelspermetre;
	bih.biClrUsed=0;
	bih.biClrImportant=0;
	bfh.bfType='MB';
	bfh.bfSize=sizeof(bfh)+bih.biSize+bih.biSizeImage;
	bfh.bfReserved1=0;
	bfh.bfReserved2=0;
	bfh.bfOffBits=sizeof(bfh)+bih.biSize;
	vector <RGBQUAD> row;
	for(LONG i=0; i<bih.biHeight; i++)
	{
		for(LONG j=0; j<rgb.at(i).size(); j++)
		{
			row.push_back(rgb.at(i).at(j));
		}
		if (j+1!=bih.biWidth)
		{
			RGBQUAD white;
			white.rgbBlue=255;
			white.rgbGreen=255;
			white.rgbRed=255;
			white.rgbReserved=0;
			for(j; j<bih.biWidth; j++) row.push_back(white);
		}
		q.push_back(row);
	}
}

void bitmap24::save(const char *filename)
{
	fstream fout;
	fout.open(filename,ios::out|ios::binary);
	fout.write((char*)&bfh.bfType,2);
	fout.write((char*)&bfh.bfSize,4);
	fout.write((char*)&bfh.bfReserved1,2);
	fout.write((char*)&bfh.bfReserved2,2);
	fout.write((char*)&bfh.bfOffBits,4);
```

```
        fout.write((char*)&bih.biSize,4);
        fout.write((char*)&bih.biWidth,4);
        fout.write((char*)&bih.biHeight,4);
        fout.write((char*)&bih.biPlanes,2);
        fout.write((char*)&bih.biBitCount,2);
        fout.write((char*)&bih.biCompression,4);
        fout.write((char*)&bih.biSize,4);
        fout.write((char*)&bih.biXPelsPerMeter,4);
        fout.write((char*)&bih.biYPelsPerMeter,4);
        fout.write((char*)&bih.biClrUsed,4);
        fout.write((char*)&bih.biClrImportant,4);
        int bytesperpixel=bih.biBitCount/8;
        for(LONG i=0; i<bih.biHeight; i++)
        {
              for(LONG j=0; j<bih.biWidth; j++)
              {
                    fout.write((char*)&q.at(i).at(j).rgbBlue,1);
                    fout.write((char*)&q.at(i).at(j).rgbGreen,1);
                    fout.write((char*)&q.at(i).at(j).rgbRed,1);
              }
        }

        fout.close();
}
```

# Chapter 9 References

Atreya, S. K., Donahue, T. M., & Kuhn, W. R. 1978, Evolution of a nitrogen atmosphere on Titan. Science, 201, 611.

Barth, E. L., & Rafkin, S. C. R. 2007, TRAMS: A new dynamic cloud model for Titan's methane clouds. Geophysical Research Letters, 34, L03305.

Besley, L. M. 1985, Interpolation procedures for ceramic-encapsulated rhodium iron alloy resistance thermometers in the temperature-range 77 K to 273 K. Journal of Physics E-Scientific Instruments, 18, 201.

Bird, M. K., Allison, M., Asmar, S. W., Atkinson, D. H., Avruch, I. M., Dutta-Roy, R., Dzierma, Y., Edenhofer, P., Folkner, W. M., Gurvits, L. I., Johnston, D. V., Plettemeier, D., Pogrebenko, S. V., Preston, R. A., & Tyler, G. L. 2005, The vertical profile of winds on Titan. Nature, 438, 800.

Bird, M. K., Dutta-Roy, R., Heyl, M., Allison, M., Asmar, S. W., Folkner, W. M., Preston, R. A., Atkinson, D. H., Edenhofer, P., Plettemeier, D., Wohlmuth, R., Iess, L., & Tyler, G. L. 2002, The Huygens Doppler Wind Experiment - Titan winds derived from probe radio frequency measurements. Space Science Reviews, 104, 613.

Broadfoot, A. L., Sandel, B. R., Shemansky, D. E., Holberg, J. B., Smith, G. R., Strobel, D. F., McConnel, J. C., Kumar, S., Hunten, D. M., Atreya, S. K., Donahue, T. M., Moos, H. W., Bertaux, J. L., Blamont, J. E., Pomphrey, R. B., & Linick, S. 1981, Extreme ultraviolet observations from Voyager 1 encounter with Saturn. Science, 212, 206.

Brown, M. E., Bouchez, A. H., & Griffith, C. A. 2002, Direct detection of variable tropospheric clouds near Titan's south pole. 420, 795.

Brown, R. H., Baines, K. H., Bellucci, G., Bibring, J. P., Buratti, B. J., Capaccioni, F., Cerroni, P., Clark, R. N., Coradini, A., Cruikshank, D. P., Drossart, P., Formisano, V., Jaumann, R., Langevin, Y., Matson, D. L., McCord, T. B., Mennella, V., Miller, E., Nelson, R. M., Nicholson, P. D., Sicardy, B., & Sotin, C. 2004, The Cassini Visual and

Infrared Mapping Spectrometer (VIMS) investigation. Space Science Reviews, 115, 111.

Bucker, D., & Wagner, W. 2006a, A reference equation of state for the thermodynamic properties of ethane for temperatures from the melting line to 675 K and pressures up to 900 MPa. Journal of Physical and Chemical Reference Data, 35, 205.

Bucker, D., & Wagner, W. 2006b, Reference equations of state for the thermodynamic properties of fluid phase n-butane and isobutane. Journal of Physical and Chemical Reference Data, 35, 929.

Buser, M., Frommhold, L., Gustafsson, M., Moraldi, M., Champagne, M. H., & Hunt, K. L. C. 2004, Far-infrared absorption by collisionally interacting nitrogen and methane molecules. Journal of Chemical Physics, 121, 2617.

Campbell, D. B., Black, G. J., Carter, L. M., & Ostro, S. J. 2003, Radar evidence for liquid surfaces on Titan. Science, 302, 431.

Courtin, R., Gautier, D., & McKay, C. P. 1995, Titan's thermal emission-spectrum - reanalysis of the voyager infrared measurements. Icarus, 114, 144.

Dain, Y., & Lueptow, R. M. 2001a, Acoustic attenuation in a three-gas mixture: Results. Journal of the Acoustical Society of America, 110, 2974.

Dain, Y., & Lueptow, R. M. 2001b, Acoustic attenuation in three-component gas mixtures - Theory. Journal of the Acoustical Society of America, 109, 1955.

Dymond, J. H., & Smith, E. B. 1969, The virial coefficients of gases (Oxford University Press).

Ejakov, S. G., Phillips, S., Dain, Y., Lueptow, R. M., & Visser, J. H. 2003, Acoustic attenuation in gas mixtures with nitrogen: Experimental data and calculations. Journal of the Acoustical Society of America, 113, 1871.

Elachi, C., Allison, M. D., Borgarelli, L., Encrenaz, P., Im, E., Janssen, M. A., Johnson, W. T. K., Kirk, R. L., Lorenz, R. D., Lunine, J. I., Muhleman, D. O., Ostro, S. J., Picardi, G., Posa, F., Rapley, C. G., Roth, L. E., Seu, R., Soderblom, L. A., Vetrella, S., Wall,

S. D., Wood, C. A., & Zebker, H. A. 2004, Radar: The Cassini Titan RADAR Mapper. Space Science Reviews, 115, 71.

Elachi, C., Wall, S., Allison, M., Anderson, Y., Boehmer, R., Callahan, P., Encrenaz, P., Flamini, E., Franceschetti, G., Gim, Y., Hamilton, G., Hensley, S., Janssen, M., Johnson, W., Kelleher, K., Kirk, R., Lopes, R., Lorenz, R., Lunine, J., Muhleman, D., Ostro, S., Paganelli, F., Picardi, G., Posa, F., Roth, L., Seu, R., Shaffer, S., Soderblom, L., Stiles, B., Stofan, E., Vetrella, S., West, R., Wood, C., Wye, L., & Zebker, H. 2005, Cassini Radar views the surface of Titan. Science, 308, 970.

Elachi, C., Wall, S., Janssen, M., Stofan, E., Lopes, R., Kirk, R., Lorenz, R., Lunine, J., Paganelli, F., Soderblom, L., Wood, C., Wye, L., Zebker, H., Anderson, Y., Ostro, S., Allison, M., Boehmer, R., Callahan, P., Encrenaz, P., Flamini, E., Francescetti, G., Gim, Y., Hamilton, G., Hensley, S., Johnson, W., Kelleher, K., Muhleman, D., Picardi, G., Posa, F., Roth, L., Seu, R., Shaffer, S., Stiles, B., Vetrella, S., & West, R. 2006, Titan Radar Mapper observations from Cassini's T3 fly-by. Nature, 441, 709.

Ely, J. F. 1990, A predictive, exact shape factor extended corresponding states model for mixtures. Advances in Cryogenic Engineering, 35, 1511.

Esposito, L. W., Barth, C. A., Colwell, J. E., Lawrence, G. M., McClintock, W. E., Stewart, A. I. F., Keller, H. U., Korth, A., Lauche, H., Festou, M. C., Lane, A. L., Hansen, C. J., Maki, J. N., West, R. A., Jahn, H., Reulke, R., Warlich, K., Shemansky, D. E., & Yung, Y. L. 2004, The Cassini Ultraviolet Imaging Spectrograph investigation. Space Science Reviews, 115, 299.

Estela-Uribe, J. F., & Trusler, J. P. M. 2000, Acoustic and volumetric virial coefficients of nitrogen. International Journal of Thermophysics, 21, 1033.

Estela-Uribe, J. F., Trusler, J. P. M., Chamorro, C. R., Segovia, J. J., Martin, M. C., & Villamanan, M. A. 2006, Speeds of sound in {(1-x)CH4+ xN2} with x = (0.10001, 0.19999, and 0.5422) at temperatures between 170 K and 400 K and pressures up to 30 MPa. Journal of Chemical Thermodynamics, 38, 929.

Feynman, R. P. 1972, Statistical mechanics, a set of lectures.

Flasar, F. M. 1983, Oceans on Titan. Science, 221, 55.

Flasar, F. M. 1998, The dynamic meteorology of Titan. Planetary and Space Science, 46, 1125.

Flasar, F. M., Kunde, V. G., Abbas, M. M., Achterberg, R. K., Ade, P., Barucci, A., Bezard, B., Bjoraker, G. L., Brasunas, J. C., Calcutt, S., Carlson, R., Esarsky, C. J. C., Conrath, B. J., Coradini, A., Courtin, R., Coustenis, A., Edberg, S., Edgington, S., Ferrari, C., Fouchet, T., Gautier, D., Gierasch, P. J., Grossman, K., Irwin, P., Jennings, D. E., Lellouch, E., Mamoutkine, A. A., Marten, A., Meyer, J. P., Nixon, C. A., Orton, G. S., Owen, T. C., Pearl, J. C., Prange, R., Raulin, F., Read, P. L., Romani, P. N., Samuelson, R. E., Segura, M. E., Showalter, M. R., Simon-Miller, A. A., Smith, M. D., Spencer, J. R., Spilker, L. J., & Taylor, F. W. 2004, Exploring the Saturn system in the thermal infrared: The Composite Infrared Spectrometer. Space Science Reviews, 115, 169.

Fulchignoni, M., Ferri, F., Angrilli, F., Ball, A. J., Bar-Nun, A., Barucci, M. A., Bettanini, C., Bianchini, G., Borucki, W., Colombatti, G., Coradini, M., Coustenis, A., Debei, S., Falkner, P., Fanti, G., Flamini, E., Gaborit, V., Grard, R., Hamelin, M., Harri, A. M., Hathi, B., Jernej, I., Leese, M. R., Lehto, A., Stoppato, P. F. L., Lopez-Moreno, J. J., Makinen, T., McDonnell, J. A. M., McKay, C. P., Molina-Cuberos, G., Neubauer, F. M., Pirronello, V., Rodrigo, R., Saggin, B., Schwingenschuh, K., Seiff, A., Simoes, F., Svedhem, H., Tokano, T., Towner, M. C., Trautner, R., Withers, P., & Zarnecki, J. C. 2005, In situ measurements of the physical characteristics of Titan's environment. Nature, 438, 785.

Fulchignoni, M., Ferri, F., Angrilli, F., Bar-Nun, A., Barucci, M. A., Bianchini, G., Borucki, W., Coradini, M., Coustenis, A., Falkner, P., Flamini, E., Grard, R., Hamelin, M., Harri, A. M., Leppelmeier, G. W., Lopez-Moreno, J. J., McDonnell, J. A. M., McKay, C. P., Neubauer, F. H., Pedersen, A., Picardi, G., Pirronello, V., Rodrigo, R.,

Schwingenschuh, K., Seiff, A., Svedhem, H., Vanzani, V., & Zarnecki, J. 2002, The characterisation of Titan's atmospheric physical properties by the Huygens Atmospheric Structure Instrument (HASI). Space Science Reviews, 104, 395.

Garry, J. C. 1996, Surveying Titan acoustically, (University of Kent at Canterbury).

Gendron, E., Coustenis, A., Drossart, P., Combes, M., Hirtzig, M., Lacombe, F., Rouan, D., Collin, C., Pau, S., & Lagrange, A.-M. 2004, VLT/NACO adaptive optics imaging of Titan. Astronomy and Astrophysics, 00417, L21.

Hagermann, A., Rosenberg, P. D., Towner, M. C., Garry, J. R. C., Svedhem, H., Leese, M. R., Hathi, B., Lorenz, R. D., & Zarnecki, J. C. 2007, Speed of sound measurements and the methane abundance in Titan's atmosphere. Icarus, 189, 538.

Hagermann, A., & Zarnecki, J. C. 2006, Virial treatment of the speed of sound in cold, dense atmospheres and application to Titan. Monthly Notices of the Royal Astronomical Society, 368, 321.

Hagermann, A., Zarnecki, J. C., Towner, M. C., Rosenberg, P. D., Lorenz, R. D., Leese, M. R., Hathi, B., & Ball, A. J. 2005, Physical properties as indicators of liquid compositions: Derivation of the composition for Titan's surface liquids from the Huygens SSP measurements. Monthly Notices of the Royal Astronomical Society, 359, 637.

Han, S. J., Lin, H. M., & Chao, K. C. 1988, Vapour-liquid equilibrium of molecular fluid mixtures by equation of state. Chemical Engineering Science, 43, 2327.

Harland, D. M. 2007, Cassini at Saturn - Huygens results (Springer Praxis).

Harri, A. M., Makinen, T., Lehto, A., Kahanpaa, H., & Siili, T. 2006, Vertical pressure profile of Titan - observations of the PPI/HASI instrument. Planetary and Space Science, 54, 1117.

Herzfeld, K. F., & Litovitz, T. A. 1959, Absorption and dispersion of ultrasonic waves (New York and London: Academic Press).

Hueso, R., & Sanchez-Lavega, A. 2006, Methane storms on Saturn's moon Titan. Nature, 442, 428.

Hunten, D. M. 2006, The sequestration of ethane on Titan in smog particles. 443, 669.

Huygens, C. 1655, De Saturni luna observatio nova.

Israel, G., Cabane, M., Brun, J. F., Niemann, H., Way, S., Riedler, W., Steller, M., Raulin, F., & Coscia, D. 2002, Huygens Probe aerosol collector pyrolyser experiment. Space Science Reviews, 104, 433.

Israel, G., Szopa, C., Raulin, F., Cabane, M., Niemann, H. B., Atreya, S. K., Bauer, S. J., Brun, J. F., Chassefiere, E., Coll, P., Conde, E., Coscia, D., Hauchecorne, A., Millian, P., Nguyen, M. J., Owen, T., Riedler, W., Samuelson, R. E., Siguier, J. M., Steller, M., Sternberg, R., & Vidal-Madjar, C. 2005, Complex organic matter in Titan's atmospheric aerosols from in situ pyrolysis and analysis. Nature, 438, 796.

Jacobsen, R. T., & Stewart, R. B. 1973, Thermodynamic properties of nitrogen Including liquid and vapor phases from 63 K to 2000 K with pressures to 10,000 Bar. Journal of Physical and Chemical Reference Data, 2, 757.

Kelner, E., Minachi, A., Owen, T. E., Burzynski, M. J. R., & Petullo, S. P. 2004, in (Worldwide Patent WO2004046669)

Kliore, A. J., Anderson, J. D., Armstrong, J. W., Asmar, S. W., Hamilton, C. L., Rappaport, N. J., Wahlquist, H. D., Ambrosini, R., Flasar, F. M., French, R. G., Iess, L., Marouf, E. A., & Nagy, A. F. 2004, Cassini radio science. Space Science Reviews, 115, 1.

Kuiper, G. P. 1944, Titan: A satellite with an atmosphere. Astrophysical Journal, 100, 378.

Kunz, O., Klimeck, R., Wagner, W., & Jaeschke, M. in press, The GERG-2004 wide-range reference equation of state for natural gases. GERG Technical Monographs

Lebreton, J. P., Witasse, O., Sollazzo, C., Blancquaert, T., Couzin, P., Schipper, A. M., Jones, J. B., Matson, D. L., Gurvits, L. I., Atkinson, D. H., Kazeminejad, B., & Perez-

Ayucar, M. 2005, An overview of the descent and landing of the Huygens probe on Titan. Nature, 438, 758.

Lellouch, E., Coustenis, A., Gautier, D., Raulin, F., Dubouloz, N., & Frere, C. 1989, Titan's atmosphere and hypothesized ocean: A reanalysis of the Voyager 1 radio-occultation and IRIS 7.7 μm data. Icarus, 79, 328.

Lemmon, E. W., & Ihmels, E. C. 2005, Thermodynamic properties of the butenes Part II. Short fundamental equations of state. Fluid Phase Equilibria, 228, 173.

Lemmon, E. W., & Jacobsen, R. T. 1999, A generalized model for the thermodynamic properties of mixtures. International Journal of Thermophysics, 20, 825.

Lemmon, E. W., & Span, R. 2006, Short fundamental equations of state for 20 industrial fluids. Journal of Chemical and Engineering Data, 51, 785.

Lemmon, E. W., & Tillner-Roth, R. 1999, A Helmholtz energy equation of state for calculating the thermodynamic properties of fluid mixtures. Fluid Phase Equilibria, 165, 1.

Lindal, G. F., Wood, G. E., Hotz, H. B., Sweetnam, D. N., Eshleman, V. R., & Tyler, G. L. 1983, The atmosphere of Titan: An analysis of the Voyager 1 radio occultation measurements. Icarus, 53, 348.

Lorenz, R. D. 1993, The life, death and afterlife of a raindrop on Titan. Planetary and Space Science, 41, 647.

Lorenz, R. D. 1999, Speed of sound in outer planet atmospheres. Planetary and Space Science, 47, 67.

Lorenz, R. D., & Lunine, J. I. 1997, Titan's surface reviewed: the nature of bright and dark terrain. Planetary and Space Science, 45, 981.

Lorenz, R. D., Niemann, H. B., Harpold, D. N., Way, S. H., & Zarnecki, J. C. 2006a, Titan's damp ground: Constraints on Titan surface thermal properties from the temperature evolution of the Huygens GCMS inlet. Meteoritics & Planetary Science, 41, 1705.

Lorenz, R. D., Wall, S., Radebaugh, J., Boubin, G., Reffet, E., Janssen, M., Stofan, E., Lopes, R., Kirk, R., Elachi, C., Lunine, J., Mitchell, K., Paganelli, F., Soderblom, L., Wood, C., Wye, L., Zebker, H., Anderson, Y., Ostro, S., Allison, M., Boehmer, R., Callahan, P., Encrenaz, P., Ori, G. G., Francescetti, G., Gim, Y., Hamilton, G., Hensley, S., Johnson, W., Kelleher, K., Muhleman, D., Picardi, G., Posa, F., Roth, L., Seu, R., Shaffer, S., Stiles, B., Vetrella, S., Flamini, E., & West, R. 2006b, The sand seas of Titan: Cassini RADAR observations of longitudinal dunes. Science, 312, 724.

Lunine, J. I., Lorenz, R. D., & Hartmann, W. K. 1998, Some speculations on Titan's past, present and future. Planetary and Space Science, 46, 1099.

Lunine, J. I., & Stevenson, D. J. 1987, Clathrate and ammonia hydrates at high pressure: Application to the origin of methane on Titan. Icarus, 70, 61.

Lunine, J. I., Stevenson, D. J., & Yung, Y. L. 1983, Ethane ocean on Titan. Science, 222, 1229.

McCord, T. B., Hansen, G. B., Buratti, B. J., Clark, R. N., Cruikshank, D. P., D'Aversa, E., Griffith, C. A., Baines, E. K. H., Brown, R. H., Dalle Ore, C. M., Filacchione, G., Formisano, V., Hibbitts, C. A., Jaumann, R., Lunine, J. I., Nelson, R. M., & Sotin, C. 2006, Composition of Titan's surface from Cassini VIMS. Planetary and Space Science, 54, 1524.

Merryweather-Clarke, N. 1995, Huygens/SSP thermal interface mathematical model. Internal Document

Milenko, Y. Y., Sibileva, R. M., & Strzhemechny, M. A. 1997, Natural ortho-para conversion rate in liquid and gaseous hydrogen. Journal of Low Temperature Physics, 107, 77.

Niemann, H. B., Atreya, S. K., Bauer, S. J., Biemann, K., Block, B., Carignan, G. R., Donahue, T. M., Frost, R. L., Gautier, D., Haberman, J. A., Harpold, D., Hunten, D. M., Israel, G., Lunine, J. I., Mauersberger, K., Owen, T. C., Raulin, F., Richards, J. E.,

& Way, S. H. 2002, The Gas Chromatograph Mass Spectrometer for the Huygens Probe. Space Science Reviews, 104, 553.

Niemann, H. B., Atreya, S. K., Bauer, S. J., Carignan, G. R., Demick, J. E., Frost, R. L., Gautier, D., Haberman, J. A., Harpold, D. N., Hunten, D. M., Israel, G., Lunine, J. I., Kasprzak, W. T., Owen, T. C., Paulkovich, M., Raulin, F., Raaen, E., & Way, S. H. 2005, The abundances of constituents of Titan's atmosphere from the GCMS instrument on the Huygens probe. Nature, 438, 779.

Ori, G. G., Marinangeli, L., Baliva, A., Bressan, M., & Strom, R. G. 1998, Fluid dynamics of liquids on Titan's surface. Planetary and Space Science, 46, 1417.

Owen, T. 1982, The composition and origin of Titan's atmosphere. Planetary and Space Science, 30, 833.

Peng, D.-Y., & Robinson, D. B. 1976, A new two-constant equation of state. Industrial & Engineering Chemistry Fundamentals, 15, 59.

Porco, C. C., Baker, E., Barbara, J., Beurle, K., Brahic, A., Burns, J. A., Charnoz, S., Cooper, N., Dawson, D. D., Del Genio, A. D., Denk, T., Dones, L., Dyudina, U., Evans, M. W., Fussner, S., Giese, B., Grazier, K., Helfenstein, P., Ingersoll, A. P., Jacobson, R. A., Johnson, T. V., McEwen, A., Murray, C. D., Neukum, G., Owen, W. M., Perry, J., Roatsch, T., Spitale, J., Squyres, S., Thomas, P., Tiscareno, M., Turtle, E. P., Vasavada, A. R., Veverka, J., Wagner, R., & West, R. 2005, Imaging of Titan from the Cassini spacecraft. Nature, 434, 159.

Porco, C. C., West, R. A., Squyres, S., McEwen, A., Thomas, P., Murray, C. D., Delgenio, A., Ingersoll, A. P., Johnson, T. V., Neukum, G., Veverka, J., Dones, L., Brahic, A., Burns, J. A., Haemmerle, V., Knowles, B., Dawson, D., Roatsch, T., Beurle, K., & Owen, W. 2004, Cassini imaging science: Instrument characteristics and anticipated scientific investigations at Saturn. Space Science Reviews, 115, 363.

Redlich, O., & Kwong, J. N. S. 1949, On the thermodynamics of solutions V: An equation of state. Fugacities of gaseous solutions. Chemical Reviews, 44, 233.

Reichl, L. E. 1980, A modern course in statistical physics (Edward Arnold (Publishers) Ltd).

Ruffino, G., Castelli, A., Coppa, P., Cornaro, C., Foglietta, S., Fulchignoni, M., Gori, F., & Salvini, P. 1996, The temperature sensor on the Huygens probe for the Cassini mission: Design, manufacture, calibration and tests of the laboratory prototype. Planetary and Space Science, 44, 1149.

Sagan, C., & Dermott, S. F. 1982, The tides in the seas of Titan. Nature, 300, 731.

Samuelson, R. E., Hanel, R. A., Kunde, V. G., & Maguire, W. C. 1981, Mean molecular weight and hydrogen abundance of Titan's atmosphere. Nature, 292, 688.

Samuelson, R. E., Nath, N. R., & Borysow, A. 1997, Gaseous abundances and methane supersaturation in Titan's troposphere. Planetary and Space Science, 45, 959.

Setzmann, U., & Wagner, W. 1991, A new equation of state and tables of thermodynamic properties for methane covering the range from the melting line to 625 K at pressures up to 1000-Mpa. Journal of Physical and Chemical Reference Data, 20, 1061.

Sivia, D. S. 1996, Data analysis: A Bayesian tutorial (Clarendon Press).

Smith, P. H., Lemmon, M. T., Lorenz, R. D., Sromovsky, L. A., Caldwell, J. J., & Allison, M. D. 1996, Titan's surface, revealed by HST imaging. Icarus, 119, 336.

Smukala, J., Span, R., & Wagner, W. 2000, New equation of state for ethylene covering the fluid region for temperatures from the melting line to 450 K at pressures up to 300 MPa. Journal of Physical and Chemical Reference Data, 29, 1053.

Smythe, W. D. 1975, Spectra of hydrate frosts: Their application to the outer Solar System. Icarus, 24, 421.

Soave, G. 1972, Equilibrium constants from a Modified Redlich-Kwong equation of state. Chemical Engineering Science, 27, 1197.

Sohl, F., Sears, W. D., & Lorenz, R. D. 1995, Tidal dissipation on Titan. Icarus, 115, 278.

Sotin, C., Jaumann, R., Buratti, B. J., Brown, R. H., Clark, R. N., Soderblom, L. A., Baines, K. H., Bellucci, G., Bibring, J.-P., Capaccioni, F., Cerroni, P., Combes, M.,

Coradini, A., Cruikshank, D. P., Drossart, P., Formisano, V., Langevin, Y., Matson, D. L., McCord, T. B., Nelson, R. M., Nicholson, P. D., Sicardy, B., LeMouelic, S., Rodriguez, S., Stephan, K., & Scholz, C. K. 2005, Release of volatiles from a possible cryovolcano from near-infrared imaging of Titan. Nature, 435, 786.

Span, R., Lemmon, E. W., Jacobsen, R. T., Wagner, W., & Yokozeki, A. 2000, A reference equation of state for the thermodynamic properties of nitrogen for temperatures from 63.151 to 1000 K and pressures to 2200 MPa. Journal of Physical and Chemical Reference Data, 29, 1361.

Span, R., & Wagner, W. 1996, A new equation of state for carbon dioxide covering the fluid region from the triple-point temperature to 1100 K at pressures up to 800 MPa. Journal of Physical and Chemical Reference Data, 25, 1509.

Span, R., & Wagner, W. 2003a, Equations of state for technical applications. I. Simultaneously optimized functional forms for nonpolar and polar fluids. International Journal of Thermophysics, 24, 1.

Span, R., & Wagner, W. 2003b, Equations of state for technical applications. II. Results for nonpolar fluids. International Journal of Thermophysics, 24, 41.

Span, R., & Wagner, W. 2003c, Equations of state for technical applications. III. Results for polar fluids. International Journal of Thermophysics, 24, 111.

Stofan, E. R., Elachi, C., Lunine, J. I., Lorenz, R. D., Stiles, B., Mitchell, K. L., Ostro, S., Soderblom, L., Wood, C., Zebker, H., Wall, S., Janssen, M., Kirk, R., Lopes, R., Paganelli, F., Radebaugh, J., Wye, L., Anderson, Y., Allison, M., Boehmer, R., Callahan, P., Encrenaz, P., Flamini, E., Francescetti, G., Gim, Y., Hamilton, G., Hensley, S., Johnson, W. T. K., Kelleher, K., Muhleman, D., Paillou, P., Picardi, G., Posa, F., Roth, L., Seu, R., Shaffer, S., Vetrella, S., & West, R. 2007, The lakes of Titan. Nature, 445, 61.

Stofan, E. R., Lunine, J. I., Lopes, R., Paganelli, F., Lorenz, R. D., Wood, C. A., Kirk, R., Wall, S., Elachi, C., Soderblom, L. A., Ostro, S., Janssen, M., Radebaugh, J., Wye, L.,

Zebker, H., Anderson, Y., Allison, M., Boehmer, R., Callahan, P., Encrenaz, P., Flamini, E., Francescetti, G., Gim, Y., Hamilton, G., Hensley, S., Johnson, W. T. K., Kelleher, K., Muhleman, D., Picardi, G., Posa, F., Roth, L., Seu, R., Shaffer, S., Stiles, B., Vetrella, S., & West, R. 2006, Mapping of Titan: Results from the first Titan radar passes. Icarus, 185, 443.

Stretton, J. L. 1965, Calculation of vibrational relaxation times in polyatomic gases. Transactions of the Faraday Society, 61, 1053.

Stryjek, R., Chappelear, P. S., & Kobayashi, R. 1974, Low-temperature vapor-liquid equilibriums of nitrogen-methane system. J. Chem. Eng. Data, 19, 334.

Taylor, F. W., & Coustenis, A. 1998, Titan in the Solar System. Planetary and Space Science, 46, 1085.

Teemu, J., Makinen, J. T. T., Harri, A. M., Tokano, T., Savijarvi, H., Siili, T., & Ferri, F. 2006, Vertical atmospheric flow on Titan as measured by the HASI instrument on board the Huygens probe. Geophysical Research Letters, 33, L21803.

Timoshenko, S., & Woinowsky-Krieger, S. 1959, Theory of plates and shells (2nd ed.: McGraw-Hill Book Co.).

Tobie, G., Lunine, J. I., & Sotin, C. 2006, Episodic outgassing as the origin of atmospheric methane on Titan. Nature, 440, 61.

Tokano, T., McKay, C. P., Neubauer, F. M., Atreya, S. K., Ferri, F., Fulchignoni, M., & Niemann, H. B. 2006, Methane drizzle on Titan. Nature, 442, 432.

Tomasko, M. G., Archinal, B., Becker, T., Bezard, B., Bushroe, M., Combes, M., Cook, D., Coustenis, A., de Bergh, C., Dafoe, L. E., Doose, L., Doute, S., Eibl, A., Engel, S., Gliem, F., Grieger, B., Holso, K., Howington-Kraus, E., Karkoschka, E., Keller, H. U., Kirk, R., Kramm, R., Kuppers, M., Lanagan, P., Lellouch, E., Lemmon, M., Lunine, J., McFarlane, E., Moores, J., Prout, G. M., Rizk, B., Rosiek, M., Rueffer, P., Schroder, S. E., Schmitt, B., See, C., Smith, P., Soderblom, L., Thomas, N., & West,

R. 2005, Rain, winds and haze during the Huygens probe's descent to Titan's surface. Nature, 438, 765.

Tomasko, M. G., Buchhauser, D., Bushroe, M., Dafoe, L. E., Doose, L. R., Eibl, A., Fellows, C., McFarlane, E., Prout, G. M., Pringle, M. J., Rizk, B., See, C., Smith, P. H., & Tsetsenekos, K. 2002, The Descent Imager/Spectral Radiometer (DISR) experiment on the Huygens entry probe of Titan. Space Science Reviews, 104, 469.

Toublanc, D., Parisot, J. P., Brillet, J., Gautier, D., Raulin, F., & McKay, C. P. 1995, Photochemical modeling of Titan's atmosphere. Icarus, 113, 2.

Towner, M. C., Garry, J. R. C., Lorenz, R. D., Hagermann, A., Hathi, B., Svedhem, H., Clark, B. C., Leese, M. R., & Zarnecki, J. C. 2006, Physical properties of Titan's surface at the Huygens landing site from the Surface Science Package Acoustic Properties sensor (API-S). Icarus, 185, 457.

Trusler, J. P. M., & Zarari, M. 1992, The speed of sound and derived thermodynamic properties of methane at temperatures between 275 K and 375 K and pressures up to 10 MPa. Journal of Chemical Thermodynamics, 24, 973.

Tyler, G. L., Eshleman, V. R., Anderson, J. D., Levy, G. S., Lindal, G. F., Wood, G. E., & Croft, T. A. 1981, Radio science investigations of the Saturn system with Voyager 1 - Preliminary results. Science, 212, 201.

Younglove, B. A. 1982, Thermo-physical properties of fluids 1. Argon, ethylene, para-hydrogen, nitrogen, nitrogen trifluoride, and oxygen. Journal of Physical and Chemical Reference Data, 11, 1.

Younglove, B. A., & Ely, J. F. 1987, Thermo-physical properties of fluids 2. Methane, ethane, propane, isobutane, and normal butane. Journal of Physical and Chemical Reference Data, 16, 577.

Yung, Y. L., Allen, M., & Pinto, J. P. 1984, Photochemistry of the atmosphere of Titan: Comparison between model and observations. The Astrophysical Journal Supplement Series, 55, 465.

Zarnecki, J. C., Leese, M. R., Garry, J. R. C., Ghafoor, N., & Hathi, B. 2002, Huygens' Surface Science Package. Space Science Reviews, 104, 593.

Zarnecki, J. C., Leese, M. R., Hathi, B., Ball, A. J., Hagermann, A., Towner, M. C., Lorenz, R. D., McDonnell, J. A. M., Green, S. F., Patel, M. R., Ringrose, T. J., Rosenberg, P. D., Atkinson, K. R., Paton, M. D., Banaszkiewicz, M., Clark, B. C., Ferri, F., Fulchignoni, M., Ghafoor, N. A. L., Kargl, G., Svedhem, H., Delderfield, J., Grande, M., Parker, D. J., Challenor, P. G., & Geake, J. E. 2005, A soft solid surface on Titan as revealed by the Huygens Surface Science Package. Nature, 438, 792.